Supersymmetry Searches in the Single Lepton Final State with the ATLAS Detector

by

Keith Morgan Edmonds

A Thesis Submitted in Partial Fullfillment of the
Requirements for the Degree of

DOCTOR RERUM NATURALIUM

in the Department of Physics

Keith Morgan Edmonds, 2011
Johannes Gutenberg - Universität Mainz

Abstract

This thesis presents an analysis for the search of Supersymmetry with the ATLAS detector at the LHC. The final state with one lepton, several coloured particles and large missing transverse energy was chosen. Particular emphasis was placed on the optimization of the requirements for lepton identification. This optimization showed to be particularly useful when combining with multi-lepton selections. The systematic error associated with the higher order QCD diagrams in Monte Carlo production is given particular focus. Methods to verify and correct the energy measurement of hadronic showers are developed. Methods for the identification and removal of mismeasurements caused by the detector environment are applied. A new detector simulation system is shown to provide good prospects for future fast Monte Carlo production. The analysis was performed for $\approx$ 35 pb^{-1} and no significant deviation from the Standard Model is seen. Exclusion limits are found in the single muon and four jets subchannel for minimal Supergravity. Previous limits set by Tevatron and LEP are extended.

Table of Contents

Chapter 1

Introduction

The Standard Model of elementary particle physics is very successful in describing the fundamental constituents of matter and their interactions. The vast majority of experimental measurements are consistent with the Standard Model. It represents the current best representation of the building blocks of reality. Nevertheless, there are theoretical as well as experimental difficulties that motivate an extension of the Standard Model to a more general theory. Supersymmetry is an interesting possibility for naturally extending the Standard Model.

Searches for Supersymmetry are among the main physics goals of the ATLAS experiment at the CERN Large Hadron Collider (LHC). If they exist, the LHC will be able to copiously produce Supersymmetric particles with masses up to several TeV so there are very strong possibilities for discovery. If new particles are found, it is important to investigate the properties of these particles, such as masses, couplings and lifetimes, to determine what possible models are consistent with those measurements. Many models of Supersymmetry are being explored and they span a large phenomenological space. To reduce the number of parameters and therefore facilitate the study of the phenomenology at colliders, some simplified models are defined. These are defined by imposing conditions on the breaking of Supersymmetry. Among the most appealing for study is minimal

Supergravity (mSUGRA), with the additional requirement that the lightest particle is stable and only weakly interacting. This leads to final states characterized by multiple high energy jets and large missing transverse energy.

This thesis pertains to searches for Supersymmetry using leptonic final states. Several studies necessary for such searches are presented. The following chapter will give an overview of the theory for both the Standard Model and Supersymmetry. In the third chapter the LHC and the ATLAS detector will be discussed with explanations of the various subsystems. Chapter 4 will begin with a discussion of the pertinent Supersymmetry phenomenology and the important backgrounds for this topology. Current experimental constraints and limit setting is then briefly discussed. In chapter 5 the Monte Carlo event generation and detector simulation techniques are discussed. This leads to a presentation of object reconstruction and identification methods. Methods for event cleaning and the removal of Cosmic backgrounds are discussed in Chapter 6. Chapter 7 will involve discussions of various preliminary analyses. These include validation of the ATLAS fast simulation system and lepton definition optimization. Chapter 8 contains a discussion of a method to obtain the jet energy scale from $t\bar{t}$ background events. Chapter 9 is a discussion of the various theoretical uncertainties that arise in the production of the W Boson with associated jets. In chapter 10 a data analysis is presented for $\approx 35\ pb^{-1}$. In chapter 11 a conclusion is given and future possibilities are briefly discussed.

Chapter 2

Particle Physics

The purpose of physics has always been to explain the world around us. The branch of physics aimed at describing the microscopic world is called particle physics. The current mathematical model of particle physics is simply called the Standard Model of Particle Physics [1]. This Standard Model (SM) has held up to dozens of tests over the last few decades [2]. No clear discrepancies between theory and experiment have been found up to the current energy scale of a few hundred GeV. There are several theoretical and some experimental reasons why one would think that the Standard Model is not a fundamental theory but instead an effective theory for the scales already probed. There are many possibilities for the extension of the Standard Model above the TeV scale. One of the most natural models is called Supersymmetry (SUSY), which postulates a new symmetry between Fermions and Bosons. Supersymmetry provides solutions to many of the open questions in the Standard Model and this makes it a very good candidate for new physics.

2.1 The Standard Model

In particle physics the fundamental laws that control the make-up of matter and the physical universe are expressed by excitations of quantized fields obeying symmetries.

Each type of excitation in each field can be associated with a classical particle. Particles are generally distinguished by mass eigenstates and quantum numbers. Particle physics studies the basic elements of matter and the forces acting between them. The SM is a theory which describes how three of the four known fundamental forces interact to make up all known matter. The Standard Model is based on two relativistic quantum field theories: Quantum Chromodynamics (QCD) and Quantum Flavour Dynamics (QFD). QCD describes the interactions of the colour charged particles through the strong force. QFD describes the theory of electroweak interactions. One of the symmetries of QFD is broken below TeV scales and the remaining symmetry forms Quantum Electrodynamics (QED) which describes the electromagnetic interaction of electrically charged particles. The Standard Model falls short of being a complete theory of fundamental interactions, primarily because it does not include the force gravity.

The fields are represented classically by point particles with certain properties called quantum numbers. Quantum numbers are quantized properties which can be used to classify particles. One important quantum number is "spin" which is often described as the internal angular momentum of a particle. Particles represent positive fluctuations of the field. Negative fluctuations are represented by anti-particles which have all the same quantum numbers but with opposite sign. The mass for particles and antiparticles must be the same because they correspond to symmetrically opposing fluctuations in the field.

Within the Standard Model two classes of particles can be distinguished by spin, Fermions and Bosons. Fermions are particles of half odd integer spin obeying Fermi-Dirac statistics and form ordinary matter. A system of identical particles obeying Fermi-Dirac statistics is totally anti-symmetric under the interchange of any pair of particles. The Fermions can be split into two groups based on their colour charge quantum number, the quarks and the leptons. QCD governs the strong interaction between the coloured quarks which acts to bind them into colour singlet hadrons such as protons and neutrons. Leptons are colour singlets and therefore do not interact with the strong force.

Bosons have integer spin and are often dubbed the force carriers of the Standard Model because they mediate the different interactions associated with force. Bosons obey Bose-Einstein statistics in that a system of identical Bosons is totally symmetric under the interchange of any pair. The photon is the mediator for electromagnetism, the Z and the W Bosons are related to the weak force, while the gluons are responsible for the strong force. The only undiscovered particle of the Standard Model is the Higgs Boson which is a by-product of the mechanism responsible for how particles acquire mass.

As can be seen in figure 2.1 the Fermions are broken up into 3 generations (I, II and III) while the Bosons are each arranged into groups by their force. The Higgs mechanism and its effect on the electroweak sector is represented by the dashed lines. This makes for 37 distinct particles in the Standard Model, although, one rarely distinguishes between particles by colour. Furthermore, each Fermion has an associated anti-particle which brings the total to 61 particles with differing quantum numbers. Most particles decay quite quickly to ordinary matter.

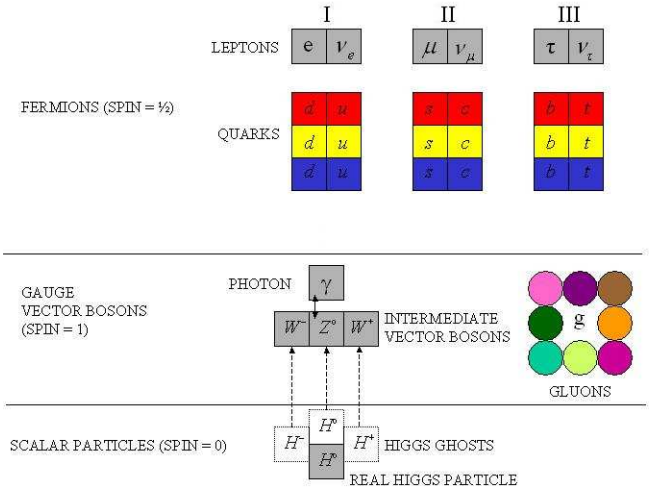

Figure 2.1: 37 Standard Model particles are shown grouped by some of their interactions and symmetries. There are an additional 24 anti-particles from the Fermions.

In the Standard Model it is assumed that neutrinos are massless. Although, this has been experimentally proven to be wrong it is a convenient assumption since the masses are practically zero and their exact nature is unknown [3]. The knowledge that neutrinos have mass is not nearly enough information to know the details of their nature. It is

assumed that the true theory of neutrinos can be added to the SM with little change to experimental predictions at colliders.

The SM particles are summarized in table 2.1.

Table 2.1: The particle content of the SM. [4]

Name	Symbol	Spin	Charge	Coloured	Mass (MeV)
Fermions (× 2 for anti-particles)					
Leptons					
Electron	e	$1/2$	-1	No	0.51
Electron Neutrino	ν_e	$1/2$	0	No	≈ 0
Muon	μ	$1/2$	-1	No	105.66
Muon Neutrino	ν_μ	$1/2$	0	No	≈ 0
Tau	τ	$1/2$	-1	No	1,777
Tau Neutrino	ν_τ	$1/2$	0	No	≈ 0
Quarks (× 3 for colour)					
Up	u	$1/2$	$2/3$	yes	1.9
Down	d	$1/2$	$-1/3$	yes	4.4
Charm	c	$1/2$	$2/3$	yes	1320
Strange	s	$1/2$	$-1/3$	yes	87
Top	t	$1/2$	$2/3$	yes	172,700
Bottom	b	$1/2$	$-1/3$	yes	4,240
Bosons					
Photon	γ	1	0	no	0
W (+ & -)	$W^\pm$	1	± 1	no	80,398
Z	Z	1	0	no	91.188
gluons	g	1	0	yes	0
Higgs	H	0	0	no	>114,400

2.1.1 Symmetries and Interactions

The interactions of the SM can be derived mathematically from the principle of local gauge invariance. This is a symmetry requirement placed upon the SM. Local symmetries are those which are dependent on position whereas global symmetries are not. Many theoretical advances have been made by requiring known global symmetries to be local.

Symmetries are directly connected to the existence of conserved quantities through Noether's theorem. For example, the conservation of 4-momentum and of angular momentum follows from the invariance of the systems Lagrangian, $\mathcal{L}$, under the operations

of translation and rotation, respectively. The equations of motion are derived from Lagrangian densities using the Euler-Lagrange equation [5]. For example, the equation of motion describing the time evolution of a free massless charged lepton, ℓ, and its associated neutrino, ν, are derived from the free lepton Lagrangian density*

$$\mathcal{L}^0_\ell = i\left(\bar{\Psi}^\ell \not{\partial} \Psi^\ell + \bar{\Psi}^\nu \not{\partial} \Psi^\nu\right) \tag{2.1}$$

where $\Psi^\ell(x)$ and $\Psi^\nu(x)$ are the complex spinors describing the state of the particles. Also, $\bar{\Psi} \equiv \Psi^\dagger \gamma^0$ where γ^μ are the Dirac matrices. Since observables only depend on $|\Psi|^2$, one can demand that the theory be invariant under local gauge transformations,

$$\Psi(x) \rightarrow \Psi'(x) = e^{i\phi(x)}\Psi(x). \tag{2.2}$$

This invariance implies that the equations of motion as well as $\mathcal{L}$ remain unchanged. There is one such local gauge transformation associated with each type of symmetry. The so-called internal symmetries give rise to important conserved quantities. The gauge principle makes the theory invariant under these transformations by adding terms to the Lagrangian. These terms include spin 1 fields (i.e. gauge Bosons) with transformation properties defined to make $\mathcal{L}$ invariant under the corresponding transformation.

The underlying symmetry group of the SM is,

$$SU(3)_C \otimes SU(2)_L \otimes U(1)_Y. \tag{2.3}$$

where C, L and Y represent colour charge, weak isospin and weak hypercharge, respectively. Equation 2.3 can be broken into two Yang-Mills theories. The first is $SU(3)$, which represents the QCD coupling of coloured particles to the $SU(3)_C$-octet gluons that arise after localizing the gauge group. These 8 Bosons, G^μ_a, are associated to 8 generators represented by Gell-Mann matrices, λ_a ($a \in [1, 8]$). The coupling strength for the strong

*$\not{\partial} \equiv \gamma^\mu \partial_\mu$.

interaction is denoted by g''.

The Lagrangian of an $SU(3)_C$ gauge theory with quark fields, q, in the fundamental triplet representation is:

$$\mathcal{L}_{QCD} = -\frac{1}{4g''^2} G^a_{\mu\nu} G^{\mu\nu}_a + \sum_{j=1}^{f} \bar{q}_j (i\gamma^\mu D_\mu - m_j) q_j \tag{2.4}$$

with the covariant derivative $D_\mu = \partial_\mu - ig'' \frac{\lambda_a}{2} G_{\mu a}$. The masses of the quarks in the sum over flavours, j, are added by hand. The QCD colour charge index has been suppressed. The symbol $G^a_{\mu\nu}$ represents the gauge invariant gluonic field strength tensor given by,

$$G^a_{\mu\nu} = \partial_\mu G^a_\nu - \partial_\nu G^a_\mu - g f_{abc} G^b_\mu G^c_\nu \tag{2.5}$$

where f_{abc} are the structure constants of $SU(3)_C$.

Due to the non-abelian nature of $SU(3)_C$ gluons are also coloured and therefore have self interaction. The interaction strength is dependent on the energy scale of the momentum transfer in the interaction probing the force. The coupling g'' is typically recast as,

$$\alpha_s(\mu) \equiv \frac{g''^2(\mu)}{4\pi}. \tag{2.6}$$

where μ represents the scale of momentum transfer. The coupling constant, $\alpha_s(\mu)$, is large for low values of momentum transfer which leads to the phenomenon of asymptotic freedom [6] and the fact that coloured particles quickly hadronize into colour singlet states.

The $SU(2)_L \otimes U(1)_Y$ in equation 2.3 represents the non-abelian gauge theory of electroweak interactions. The gauge Bosons corresponding to this group mix to form the γ, the Z and the $W^\pm$ Bosons through a process called electroweak symmetry breaking. They couple to all Fermions through weak isospin, T_3, and weak hypercharge, Y. The hypercharge is the generator of $U(1)_Y$, for which the gauge Boson is called B^μ and the

coupling strength is denoted by g. The generators of the $SU(2)_L$ group, $\vec{T} \equiv (T_1, T_2, T_3)$, are related to the Pauli spin matrices,

$$\vec{T} \equiv \frac{\vec{\sigma}}{2} = (\sigma_1, \sigma_2, \sigma_3). \tag{2.7}$$

The associated gauge Bosons are $\vec{A}^\mu$ and the coupling strength is denoted by g'. The algebra of the $SU(2)_L \otimes U(1)_Y$ group then follows $[T^i, T^j] = i\epsilon T^k$ and $[T^i, Y] = 0$.

The Fermions that couple to the gauge Bosons are grouped into multiplets of the SM gauge group. The left handed Fermions of each family are weak-isospin doublets, while the right handed ones are singlets and therefore do not couple to the $W^\pm$ Bosons. One can define chirality projectors for left handed, $\mathbf{L}$, and right handed, $\mathbf{R}$, Fermions such that,

$$\mathbf{L} \equiv \frac{1}{2}(1 - \gamma^5), \qquad \mathbf{R} \equiv \frac{1}{2}(1 + \gamma^5) \tag{2.8}$$

where $\gamma^5 \equiv i\gamma^0\gamma^1\gamma^2\gamma^3$. One can then recast the weak current [7] for a lepton, ℓ, and neutrino, ν, in the form,

$$J^+_\mu = \bar{\ell}\gamma_\mu(1 - \gamma_5)\nu = 2\bar{\ell}\gamma_\mu \mathbf{L}\nu \equiv 2\bar{\ell}_L\gamma_\mu\nu_L \ . \tag{2.9}$$

The weak currents can also be written in terms of leptonic isospin currents,

$$J^i_\mu = \frac{1}{2}\begin{pmatrix}\bar{\nu}_L & \bar{\ell}_L\end{pmatrix}\gamma_\mu\sigma^i\begin{pmatrix}\nu_L \\ \ell_L\end{pmatrix} \ . \tag{2.10}$$

A comparison will show that the weak charged current, which couples with the W Boson, can be written in terms of J^1 and J^2 as

$$J^+_\mu = 2(J^1_\mu - iJ^2_\mu). \tag{2.11}$$

The hypercharge current is given as,

$$J_\mu^Y \equiv -(\bar{\nu}_L \gamma_\mu \nu_L + \bar{\ell}_L \gamma_\mu \ell_L + 2\bar{\ell}_R \gamma_\mu \ell_R), \tag{2.12}$$

which then gives the electromagnetic current as,

$$J_\mu^{em} = -\bar{\ell}\gamma_\mu \ell = J_\mu^3 + \frac{1}{2} J_\mu^Y. \tag{2.13}$$

The group commutators then imply the Gell-Mann-Nishijima relation,

$$Q = T_3 + \frac{1}{2} Y. \tag{2.14}$$

The gauge fields B^μ and $A^{3\mu}$ combine into the photon, γ, and the Z Boson:

$$\begin{aligned} A_\mu &= cos\theta_W B^\mu + sin\theta_W A_\mu^3, \\ Z_\mu &= -sin\theta_W B^\mu + cos\theta_W A_\mu^3 \end{aligned} \tag{2.15}$$

where the angle $\theta_W \approx 0.231$ [4] is known as the Weinberg mixing angle. The A_1^μ and A_2^μ combine into the charged weak Boson fields:

$$\begin{aligned} W^{+\mu} &= \frac{1}{\sqrt{2}}(A_1^\mu - iA_2^\mu), \\ W^{-\mu} &= \frac{1}{\sqrt{2}}(A_1^\mu + iA_2^\mu). \end{aligned} \tag{2.16}$$

It can be shown using 2.14 that the coupling strengths of the electroweak interaction, g and g', are related to the coupling strength of the EM interaction, e, as

$$-e = gcos\theta_W = g' sin\theta_W \ . \tag{2.17}$$

2.1.2 The Higgs Mechanism

The SM introduces masses to the $W^{\pm}$ and Z Bosons by a mechanism which is used to break $SU(2)_L \otimes U(1)_Y$. This method also gives masses to the charged Fermions by the addition of a Yukawa coupling. The only way this is possible in a weakly coupled theory is to have a scalar field coupled without derivatives to the Fermions [5]. It is done through spontaneous symmetry breaking which means that the ground state of the system is not the ground state of the symmetry. To break this symmetry a weak isospin doublet with components of scalar Higgs fields having non-vanishing and invariant vacuum expectation values are introduced:

$$\phi = \begin{pmatrix} \phi_a \\ \phi_b \end{pmatrix} = \frac{1}{\sqrt{2}} \begin{pmatrix} \phi_1 + i\phi_2 \\ \phi_3 + i\phi_4 \end{pmatrix}. \tag{2.18}$$

The $SU(2)_L \otimes U(1)_Y$ generators are then,

$$\left(y^{(\phi)}, t_1^{(\phi)}, t_2^{(\phi)}, t_3^{(\phi)}\right) = \left(y^{(\phi)}, \vec{t}^{(\phi)}\right) = \left(\frac{g}{2}\mathbf{I}, \frac{g'}{2}\vec{\sigma}\right). \tag{2.19}$$

The kinetic energy terms break the $SU(2)_L \otimes U(1)_Y$ symmetry so the partial derivative needs to be replaced with the usual covariant derivative,

$$\partial_\mu \rightarrow D_\mu = \partial_\mu + iB_\mu y^{(\phi)} + i\vec{A}_\mu \cdot \vec{t}^{(\phi)}. \tag{2.20}$$

The Higgs Lagrangian is,

$$\mathcal{L}_\phi = \frac{1}{2}\left|D_\mu \phi\right|^2 - \frac{\mu^2}{2}\phi^\dagger\phi - \frac{\lambda}{2}(\phi^\dagger\phi)^2, \tag{2.21}$$

where λ must be positive to keep the potential from becoming negative for large ϕ which would cause instability. To tree level approximations this gives a vacuum expectation value of,

$$\langle\phi\rangle^\dagger \langle\phi\rangle \equiv v^2 = \frac{|\mu^2|}{\lambda}. \tag{2.22}$$

It is possible to make a $SU(2) \otimes U(1)$ gauge transformation to a unitary gauge where ϕ^a=0 and ϕ^b is Hermitian. In the unitary gauge the vacuum expectation values of the components are,

$$\langle\phi\rangle = \begin{pmatrix} 0 \\ v \end{pmatrix}. \tag{2.23}$$

Making the expansion of the Higgs field, h, around the vacuum,

$$\phi_0^{exp} = \frac{1}{\sqrt{2}} \begin{pmatrix} 0 \\ v + h(x) \end{pmatrix}, \tag{2.24}$$

one can then derive the explicit version of the Higgs Lagrangian density:

$$\begin{aligned} \mathcal{L}_{Higgs} &= \left| \left(\partial_\mu + iB_\mu y^{(\phi)} + i\vec{A}_\mu \cdot \vec{t}^{(\phi)} \right) \frac{v+h}{\sqrt{2}} \begin{pmatrix} 0 \\ 1 \end{pmatrix} \right|^2 \\ &- \frac{\mu^2}{2}(v+h)^2 - \frac{\lambda}{4}(v+h)^4. \end{aligned} \tag{2.25}$$

It can be seen from equations 2.16 that this includes a mass term for the weak charged Bosons, $(\frac{1}{4}vg')^2 W_\mu^+ W^{-\mu}$, that gives $m_{W^\pm} = \frac{1}{2}vg'$. The B_μ and A_μ^3 terms can be extracted from 2.25 to yield,

$$\mathcal{L}_{Higgs}^{A^3-B} = \frac{v^2}{8} \left[(B_\mu \; A_\mu^3) \begin{pmatrix} g^2 & -gg' \\ -gg' & g'^2 \end{pmatrix} \begin{pmatrix} B^\mu \\ A^{3\mu} \end{pmatrix} \right]. \tag{2.26}$$

This matrix can then be diagonalized to give a rotation corresponding to the same one as in 2.15. The resulting eigen values represent the mass terms for the fields Z_μ ($\frac{1}{2}m_Z^2 Z_\mu Z^\mu$) and A_μ ($\frac{1}{2}m_A^2 A_\mu A^\mu$) with $m_A = 0$ and $m_Z = \frac{1}{2}v\sqrt{g^2 + g'^2}$. This is equivalent to equations 2.15 so that a relation can be derived between m_W and m_Z,

$$\rho \equiv \frac{m_W^2}{m_Z^2 cos^2\theta_W} = 1. \tag{2.27}$$

The fact that $\rho = 1$ is consistent with experimental data [4] is a great achievement of the SM.

The 2^{nd} line of equation 2.25 contains a second order mass term for the Higgs field which implies that there exists a physical Higgs particle. The mass of the neutral Higgs Boson can be derived to depend on the vacuum expectation value, v, and on the coupling strength [5], λ,

$$m_h = \sqrt{2v\lambda}. \tag{2.28}$$

By introducing a so called Yukawa coupling between the Higgs field and Fermions, one can also include mass terms for the Fermions. After electroweak symmetry breaking, the fermions acquire a mass proportional to the vacuum expectation value of the Higgs field.

The bare Higgs Boson mass, m_h, receives quantum corrections from loop effects of every particle coupling directly or indirectly to the Higgs field. For Yukawa coupling particles, heavier particles give larger corrections because the Yukawa strength is related to mass. Indirectly coupling particles can also give corrections which are proportional to their mass. If undiscovered particles exist then they will have large mass and therefore induce large corrections. Other high scale phenomena such as condensates and compactified dimensions will have similar effects on the renormalized Higgs Boson mass. The theory is renormalizable through dimensional regularization so this does not destroy consistency of the model [8]. A theoretical problem arises from the question of why the sum of all these corrections appears to be small relative to the bare Higgs mass. A systematic cancellation of many large terms would be considered unnatural unless it was to originate from a symmetry. Supersymmetry is a symmetry with this property.

2.2 Supersymmetry

Supersymmetry is one possible extension to the Standard Model achieved by the addition of a symmetry between Fermions and Bosons [9]. It is a favoured Beyond the Standard Model (BSM) theory because it is a next logical symmetry extension to the Standard Model. SUSY is not an exclusively independent theory so it can be incorporated into many other theories. Several BSM scenarios require or imply Supersymmetry in order to become naturally consistent theories. The spin degree of freedom is space-time symmetry which is not integrated into the gauge theory structure at present. SUSY would do this in a natural gauge theoretic way and put spin on par with the other quantum numbers.

There are only very few possible symmetries which can exist in a theory of point particle interactions which obey Lorentz transformations. The Coleman-Mandula "no-go" theorem [10] states that the only possible S-matrix symmetries are internal symmetries or those belonging to the Poincaré group. A possible way out is a symmetry with spinorial charges rather than tensorial charges. The corresponding algebra is called a Lie-superalgebra and the corresponding theorem for supersymmetric theories is the Haag-Lopuszanski-Sohnius theorem [11]. The assumptions of this extension are consistent with that of Supersymmetry.

The generators of the Supersymmetry group change the spin of a particle by $\frac{1}{2}$. This represents a symmetry between Fermions and Bosons via a spin current. For conservation of spin, the symmetry under these operations means that for every bosonic degree of freedom there must be a corresponding fermionic degree of freedom. This implies that all particles can be associated to one or more partners through the Supersymmetric transform. The generators of Supersymmetry commute with the gauge operators so the transformation respects the gauge quantum numbers. From this, it is clear that no two particles in the Standard Model are supersymmetric partners of one another. The supersymmetric partner(s) of the Standard Model particles are called sparticles. The names of the SM Fermions are constructed with the prefix "s" as in selectron or sneutrino.

Those of the SM Bosons are constructed with the suffix "ino" as in photino or higgsino.

If one takes the operator that generates Supersymmetry to be Q, then

$$Q\,|Boson\rangle \;=\; |Fermion\rangle\,, \quad \text{and} \quad Q\,|Fermion\rangle \;=\; |Boson\rangle\,. \tag{2.29}$$

In a supersymmetric extension of the Standard Model, each of the known fundamental particles must be in either a chiral or gauge supermultiplet. It is important to note that only chiral supermultiplets can contain Fermions whose left handed parts do not transform in the same way as their right handed parts under the gauge group. The left handed and right handed parts of Standard Model Fermions are two component Weyl Fermions which have differing gauge transformations. This implies that the left handed and right handed parts have distinct sparticles. There are many dual representations of Supersymmetry but the two component Weyl spinor notation is the most natural in this sense.

Due to the Spin Statistic Theorem [12] the proposed set of spinorial charges Q_α with $a \in [1,4]$ is closed through anti-commutators, meaning Q must be a fermionic operator. Q_α can be expressed in terms of a Weyl spinor, Q_A, with $A \in [1,2]$ and $Q_\alpha = (Q_A, \bar{Q}^{\dot{A}})$ where $\bar{Q}^{\dot{A}} = (Q_A)^*$. Together with the generators of the Poincaré group they form the Super-Poincaré algebra [13]:

$$\begin{aligned} [M^{\mu\nu}, Q_\alpha] &= \frac{1}{2}(S^{\mu\nu})^\beta_\alpha Q_\beta \\ [Q_\alpha, P^\mu] &= 0 \\ \{Q_\alpha, \bar{Q}_\beta\} &= 2(\Gamma^\mu)_{\alpha\beta} P_\mu \end{aligned} \tag{2.30}$$

where P is the generator of translations, M is the generator of Lorentz transformations, Γ^μ is given by $\{\Gamma^\mu, \Gamma^\nu\} = -2g^{\mu\nu}$ and $S^{\mu\nu} = \frac{i}{2}[\Gamma^\mu, \Gamma^\nu]$. If the metric, $g^{\mu\nu}$ is Minkowski, $\eta^{\mu\nu}$, then Γ^μ reduces to the well known Dirac, γ^μ, matrices. From this it is clear that Supersymmetry includes space-time transformations. If Supersymmetry is taken as a local symmetry then it naturally becomes a theory of gravity, Supergravity.

2.2.1 The MSSM

In a renormalizable supersymmetric field theory, the interactions and masses of all particles are determined by their gauge transformation properties and the superpotential, W. If SUSY were an exact symmetry the Supersymmetric partners of each particle would have the same mass. It is known from experiment that this is not the case, so SUSY must be broken.

All of the particles that have been found would necessarily be massless in the absence of electroweak symmetry breaking. All the SM fermions obtain their masses through a Yukawa coupling to the Higgs Vacuum Expectation Value (VEV) which is 0 without electroweak symmetry breaking. The photon and gluon are required to be massless by electromagnetic and QCD gauge invariance while the $W^{\pm}$ and Z bosons acquire mass through the Higgs mechanism. Conversely, all of the undiscovered particles have exactly the opposite property; each of them can have a Lagrangian mass term in the absence of electroweak symmetry breaking. For squarks, sleptons and Higgs scalars this follows from a general property of complex scalar fields that a mass term $m^2|\phi|^2$ is always allowed by all gauge symmetries. For the higgsinos and gauginos, it follows from the fact that they are fermions in a real representation of the gauge group. For obvious technological reasons experimental particle physics probes smaller scales first. This means that one would expect particles with lower masses to be found first. Therefore, if SUSY is a symmetry of nature it is not surprising that the sparticles will be found after the particles of the Standard Model.

If one considers the most simplistic version of SUSY, the Minimal Supersymmetric Standard Model (MSSM), the potential is of the form:

$$W_{MSSM} = \bar{u} y_u Q H_u - \bar{d} y_d Q H_d - \bar{e} y_e L H_d + \mu H_u H_d \tag{2.31}$$

where the family and colour indexes have been suppressed for clarity. The quantities H_u,

H_d, Q, L, $\bar{u}$, $\bar{d}$ and $\bar{e}$ are the chiral superfields corresponding to the chiral supermultiplets in table 2.2. The y_u, y_d, y_e terms are the dimensionless Yukawa coupling parameters and μ is the constant in the supersymetric version of the SM Higgs Boson mass term. In the MSSM two Higgs Bosons are needed to give mass to the up-type and down-type quarks.

Table 2.2: The particle content of the MSSM represented as chiral supermultiplets. The spin-1/2 fields are left handed two component Weyl Fermions and the spin-0 fields are complex scalars.

Names	Symbol	Spin 0/1	Spin $\frac{1}{2}$	$SU(3)$	$SU(2)$	$U(1)$
(s)quarks	Q	$(\widetilde{u}_L\ \widetilde{d}_L)$	$(u_L\ d_L)$	3	2	$\frac{1}{6}$
(×3 Families)	$\bar{u}$	$\widetilde{u}_R^*$	$u_R^\dagger$	$\bar{3}$	1	$-\frac{2}{3}$
	$\bar{d}$	$\widetilde{d}_R^*$	$d_R^\dagger$	$\bar{3}$	1	$\frac{1}{3}$
(s)leptons	L	$(\widetilde{\nu}\ \widetilde{e}_L)$	$(\nu\ e_L)$	1	2	$-\frac{1}{2}$
(×3 Families)	$\bar{e}$	$\widetilde{e}_R^*$	$e_R^\dagger$	1	1	1
Higgs(inos)	H_u	$(H_u^+\ H_u^0)$	$(\widetilde{H}_u^+\ \widetilde{H}_u^0)$	1	2	$+\frac{1}{2}$
	H_d	$(H_d^0\ H_d^-)$	$(\widetilde{H}_d^0\ \widetilde{H}_d^-)$	1	2	$-\frac{1}{2}$
bino, B Boson		B^0	$\widetilde{B}^0$	1	1	0
wino, W Bosons		$W^\pm, W^0$	$\widetilde{W}^\pm, \widetilde{W}^0$	1	3	0
gluino, gluon		g	$\widetilde{g}$	8	1	0

Since SUSY is not a true symmetry at TeV scales the underlying model should have a Lagrangian density that is invariant under Supersymmetry but a vacuum state that is not. This means that the effective Lagrangian, $\mathcal{L}$, should be broken into two parts,

$$\mathcal{L} = \mathcal{L}_{SUSY} + \mathcal{L}_{soft}, \tag{2.32}$$

where $\mathcal{L}_{SUSY}$ contains all the gauge and Yukawa interactions and obeys exact SUSY while $\mathcal{L}_{soft}$ violates SUSY but only contains mass terms and coupling parameters with positive mass dimension. The terminology "soft" comes from the requirement that terms can be added to a supersymmetric Lagrangian that do not respect supersymmetry but still keep the soft ultraviolet behaviour of the theory. These soft-breaking terms in $\mathcal{L}_{soft}$ introduce many new parameters into the theory.

SUSY Higgs Sector

As in the Standard Model the gauge symmetry of the MSSM is broken spontaneously by a Higgs mechanism. In the Standard Model a single Higgs doublet is used in order to give mass to all Fermions. In the MSSM this imposes a problem, since either only left handed or right handed superfields can be used in the construction of the Lagrangian. Additionally, the Hermitian conjugate of a left handed superfield is right handed and vice versa. The coupling to a Hermitian conjugated Higgs superfield is forbidden. This leads to the usage of two Higgs superfields, one for the u, c and t quarks and one for the d, s and b quarks. A quadratic term using the Higgs fields can be formed and added to the potential as in the SM. From this term the additional Higgs Boson mass parameter μ is introduced. The corresponding vacuum expectation values of the Higgs fields need not be the same and are denoted v_1 and v_2.

After breaking and mixing there are 5 physical Higgs Bosons. As in the Standard Model the radiative corrections to the Higgs Boson mass are derived from the heaviest particles. The one loop correction to the lightest MSSM Higgs Boson mass, m_h, is proportional to [14]:

$$\Delta m_h^2 \approx G_F m_t^4 \log\left(\frac{m_{\tilde{t_1}} m_{\tilde{t_2}}}{m_t^2}\right), \tag{2.33}$$

where $m_{\tilde{t_1}}$ and $m_{\tilde{t_2}}$ are the masses of the lightest and heaviest stop squarks respectively. Masses equal to the top quark, as in exact SUSY, would imply an exact cancellation. The two equal and opposite loop corrections from the top quark and stop squark are shown in figure 2.2.

If SUSY is expected to provide a mechanism for the radiative corrections to the Higgs mass to be small, then the relationship between dimensionless couplings must be maintained. This requirement is equivalent to requiring the SUSY breaking to be soft.

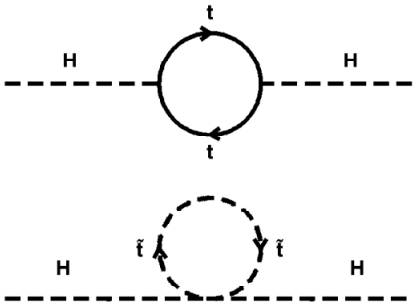

Figure 2.2: The Feynman diagrams for the cancellation of the Higgs Boson mass renormalization between fermionic top quark loop and scalar stop squark loops in SUSY [15].

R-Parity

The potential in equation 2.31 is minimal in the sense that it is able to produce a consistent supersymmetric extension to the SM. There are several ways that this can be expanded, such as adding SUSY generators in addition to Q. Many of these are clearly unneeded over-complications for a minimal model and therefore will not be discussed here. There are, however, two terms that could be added to equation 2.31 which deserve special attention. The first violates Lepton Number, L,

$$W_{\Delta L=1} = \frac{1}{2}\lambda^{ijk} L_i L_j \bar{e}_k + \lambda'^{ijk} L_i Q_j \bar{d}_k + \mu'^i L_i H_u, \tag{2.34}$$

which is defined as the number of leptons where anti-particles are counted as negative. The second violates baryon number, B,

$$W_{\Delta B=1} = \frac{1}{2}\lambda''^{ijk} \bar{u}_i \bar{d}_j \bar{d}_k, \tag{2.35}$$

which is defined as the number of quarks divided by 3 and again counting anti-particles as negative. In the Standard Model there are no such terms since there are no possible renormalizable Lagrangians with terms that violate L or B. There is, of course, the possibility of non-renormalizable terms that violate L or B but the contributions would be small. The conservation of B and L in the Standard Model is a nice feature since their violation is very well bounded experimentally [16].

One could eliminate the terms of equations 2.34 and 2.35 by simply requiring that B and L are exact symmetries. This is theoretically an issue for two reasons. One is that this constraint would be arbitrarily imposed on the model with no natural explanation. The other is that this would forbid the possible unification of the Fermions in further extensions to the Standard Model.

A very attractive way to solve all of these issues is with a B-L continuous gauge symmetry which is spontaneously broken at a scale inaccessible to current experiments. A continuous $U(1)_{B-L}$ forbids renormalizable terms which violate B and L [17]. If $U(1)_{B-L}$ is only broken by scalar vacuum expectation values (or other order parameters) that carry even integer values of 3(B-L), then there exists an exactly conserved discrete remnant subgroup at our scale which has the desired properties [18]. This conserved quantity is termed R-Parity and can be expressed as a discrete multiplicative Z_2 symmetry:

$$P_R = (-1)^{3(B-L)+2s} \tag{2.36}$$

where s is the spin of the particle. This symmetry assigns all particles a value of 1 and all sparticles a value of -1. This has a few phenomenologically interesting consequences at scales where P_R is discrete. Firstly, the Lightest Supersymmetric Particle (LSP) is stable. If it is uncoloured and electrically neutral it can be a candidate for the much sought after non-baryonic dark matter. Secondly, all sparticles must decay to an odd number of sparticles. These result in chains ending with a single sparticle, the LSP. And finally, in collider experiments, such as the LHC, sparticles must be produced in pairs.

The B-L continuous gauge symmetry method for deriving P_R is rarely used in model building. Instead it is often taken as a well motivated axiom for constraining the MSSM. Of course one does not have to make this assumption at all and there are many searches at ATLAS being done for models with R-parity violation. Within this thesis P_R is always assumed to be conserved.

mSUGRA

An elegant mechanism for spontaneous soft Supersymmetry breaking is proposed by Supergravity (SUGRA) [19]. It postulates SUSY breaking in a hidden sector at a scale of around 1 TeV, which is mediated to the MSSM sector by flavour-blind gravitational interactions. The Supergravity parameter space is far too large to be experimentally investigated in its entirety. Therefore, a phenomenologically simplified model has been introduced, the minimal version of Supergravity (mSUGRA). It is characterized by mass unification at the so-called GUT Scale, m_{GUT}, defined as the common crossing point of the running coupling constants. These constraints lead to soft supersymmetry breaking universality, which is the hypothesis that all mass matrices are proportional to the unit matrix, that the triple scalar couplings are proportional to the Yukawa matrices and that breaking parameters introduce no complex phases. This reduces the number of free parameters governing mSUGRA to five values:

m_0 : The universal scalar soft mass term

$m_{\frac{1}{2}}$: The uniform Fermion soft mass term

A_0 : The uniform tri-linear coupling

$tan(\beta)$: The ratio of vacuum expectation values of the two Higgs Boson doublets

$sign(\mu)$: The sign of the Higgs Boson mixing parameter

Even in the Standard Model there are small nonzero parameters, such as the off-diagonal components and the CP-violating phase in the quark mixing matrix. This implies the case for strict soft supersymmetry breaking universality is not very strong. Yet even though it might not be exact, soft supersymmetry breaking universality is likely a good approximation.

The assumption of mass unification is in general only theoretically motivated and based mainly on aesthetics. In fact, the most important reason for assuming unification is a practical one. As long as no signs of supersymmetry have been found, the main purpose of models is to reveal general phenomenological implications. Assuming unification

reduces the complexity of the problem, but still allows a broad range of phenomenological scenarios.

The mixing of the sparticles and their masses is very important for their phenomenology in colliders. In the most common scenario, the neutralino $\widetilde{\chi}_1^0$ is Bino-like and is the LSP. The states $\widetilde{\chi}_2^0$ and $\widetilde{\chi}_1^\pm$ are SU(2) gaugino-like and nearly degenerate. $\widetilde{\chi}_3^0$, $\widetilde{\chi}_4^0$ and $\widetilde{\chi}_2^\pm$ are Higgsino-like and because of their μ dependence share some of the characteristics of the Higgs Boson mass spectra. For sfermions the mixing between flavours can be ignored in most cases.

2.3 Conclusions

In the MSSM there are 33 distinct masses corresponding to undiscovered particles. The masses and mixing angles for these particles can be computed given an underlying model for the soft terms at some input scale. A complete set of Feynman rules for the interactions of these particles with each other and with the Standard Model particles can then be derived. Assuming that the mixing of squarks and sleptons in the I and II family is negligible, the mass eigenstates of the MSSM are listed in Table 2.3.

Supersymmetry is more than a theoretically motivated exercise since there are several ways it helps to answer questions the SM does not. Although the SM describes the discovered fundamental particles and their interactions with great success, there are some open questions that point towards an extension of the model. Some of them are intrinsic problems, some arise from cosmological measurements and some have a pure theoretical nature.

There is no explanation for the observed multiplet structure and mass hierarchy in the SM. This leads to the hope that there is a more fundamental underlying theory that overcomes this problem. Attempts have been made by defining Grand Unified Theories (GUTs) [20], which have a simpler gauge group (such as SU(5) or SO(10)) and thus

Table 2.3: The sparticles in the MSSM with sfermion mixing for the first two families assumed to be negligible.

Names	Spin 0	P_R	Gauge Eigenstates	Mass Eigenstates
Higgs Particles	Q	+1	$H_u^0\ H_d^0\ H_u^+\ H_d^-$	$h^0\ H^0\ A^0\ H_d^\pm$
squarks	0	-1	$\widetilde{u}_L\ \widetilde{u}_R\ \widetilde{d}_L\ \widetilde{d}_R$ $\widetilde{s}_L\ \widetilde{s}_R\ \widetilde{c}_L\ \widetilde{c}_R$ $\widetilde{t}_L\ \widetilde{t}_R\ \widetilde{b}_L\ \widetilde{b}_R$	(same) (same) $\widetilde{t}_1\ \widetilde{t}_2\ \widetilde{b}_1\ \widetilde{b}_2$
sleptons	0	-1	$\widetilde{e}_L\ \widetilde{e}_R\ \widetilde{\nu}_e$ $\widetilde{\mu}_L\ \widetilde{\mu}_R\ \widetilde{\nu}_\mu$ $\widetilde{\tau}_L\ \widetilde{\tau}_R\ \widetilde{\nu}_\tau$	(same) (same) $\widetilde{\tau}_1\ \widetilde{\tau}_2\ \widetilde{\nu}_\tau$
neutralinos	$\frac{1}{2}$	-1	$\widetilde{B}^0\ \widetilde{W}^0\ \widetilde{H}_u^0\ \widetilde{H}_d^0$	$\widetilde{\chi}_1^0\ \widetilde{\chi}_2^0\ \widetilde{\chi}_3^0\ \widetilde{\chi}_4^0$
charginos	$\frac{1}{2}$	-1	$\widetilde{W}^\pm\ \widetilde{H}_u^+\ \widetilde{H}_d^-$	$\widetilde{\chi}_1^\pm\ \widetilde{\chi}_2^\pm$
gluino	$\frac{1}{2}$	-1	$\widetilde{g}$	(same)
gravitino	$\frac{3}{2}$	-1	$\widetilde{G}$	(same)

have fewer coupling constants and a simpler multiplet structure. Many of these models exploit SUSY to achieve their aims. Such models are quite constraining and this leads to interesting predictions, for example the quark-to-lepton charge relations. Although theoretically appealing, such constraints often lead to clearly wrong predictions, such as overly unstable protons. Another reason why GUTs infer SUSY is the unification of the coupling constants. If there is a fundamental theory where all the forces at TeV scales are the remnants of single broken force, then there should be a scale above which this force is unified and has one coupling. Above this scale there will be one unified field and below this scale it will break into the SM structure. It is easy to imagine there being a scale for which Fermion generation is irrelevant but for a complete unified field theory all quantum numbers must be unified. In a SUSY model at a scale where SUSY is an exact symmetry, Fermions and Bosons are unified by construction so SUSY is a natural symmetry of such models.

Gravity is not included in the Standard Model and if a final theory exists it is expected that it would include Gravity. Supergravity has strong possibilities to be a basis for this unification. In fact a version of 11-dimensional Supergravity is predicted as a low energy

effective theory of the only consistent theory of quantum gravity to date, M-theory [21].

There are further reasons to believe that Supersymmetry is a symmetry of nature which are not theoretically motivated. There is an unexplained asymmetry between matter and anti-matter in the universe. This is generally associated with CP violation and current measurements of CP violation coming from the weak interaction are not large enough to account for the measured matter asymmetry. In experiments, first evidence of CP violation in the mixing of neutral B mesons has been observed [22]. This measurement differs by 3.2 standard deviations from the standard model prediction. Both common solutions to this require additions to the SM. The first is that neutrinos account for it by some additional phases but most such models are finely tuned [23]. The other solution is that this violation comes from the many phases possible in SUSY [24].

From cosmological measurements it is known that matter is mainly made of dark matter and no Standard Model particle can fulfill the experimental requirements needed for such a particle. R-parity conserving models of SUSY provide a dark matter candidate of the LSP. SUSY is not the only extension to predict a dark matter candidate but the existence of such a particle in the theory is reassuring.

If the Higgs Boson is found it could add an additional question. The stability of the Higgs Boson mass cannot be understood in a natural way. With appropriate couplings the Supersymmetric loops in the mass correction term will cancel the SM correction terms at high scales where Supersymmetry is exact.

Chapter 3

The LHC and ATLAS

Particle accelerators and colliders are the basic tools of particle physics. They allow for the creation of particles so that one can study their interactions. Detectors at colliders are used to study particle collisions through the effects the created particles have on the surrounding environment. Most collisions produce particles which quickly decay to form ordinary matter.

Since SUSY particles have not already been observed it is clear that SUSY is broken and the sparticles have higher mass than their SM counterparts. If SUSY particles do not exist at our average scale then higher scales must be artificially produced. Particle colliders cause interactions at a high center of mass energy in order to produce these higher scales where the heavy particles exist.

3.1 LHC at CERN

As of the 30^{th} of March 2010, the European Organization for Nuclear Research (CERN) is in the first running phase for the world's highest energy particle collider, the Large Hadron Collider (LHC) [25]. It is a circular accelerator with a circumference of 27 km, built approximately 100 m underground straddling the Switzerland-France border. The LHC produces proton-proton collisions at a centre of mass energy of 7 TeV by crossing

two 3.5 TeV beams. This energy is expected be enough to test the Standard Model with searches for the Higgs Boson. In later running periods, the LHC is expected to achieve a centre of mass energy of 14 TeV.

The LHC was built in the tunnel that formerly held the Large Electron-Positron collider (LEP). The LHC has two main advantages over LEP, higher energy and instantaneous luminosity. This is mainly the result of the fact that there will be less loss of energy due to synchrotron radiation than LEP because of the larger mass of the proton [26]. Although the higher energy of the LHC will allow for the ability to probe up to a higher energy, it has some disadvantages to LEP. According to the Standard Model electrons are elementary whereas protons are made of partons such as quarks and gluons. Because of this, the electron-positron interaction is much cleaner than the proton-proton interaction.

A possibly more comparable collider is the Tevatron at the Fermi National Accelerator Laboratory near Chicago. It is a proton anti-proton collider with a center of mass of 1.96 GeV. The Tevatron has two multipurpose detectors at collision points, D0 and CDF.

Two beams of protons at 450 GeV will be injected into the LHC beam pipes from the Super Proton Synchrotron and accelerated to higher energy within the LHC. Superconducting magnets with a magnetic field of 8.5 Tesla keep the protons inside the beam pipes. The schematic layout of the LHC complex with its various systems are shown in figure 3.1.

The LHC beam is not intended to be continuous but broken into bunches. For the data periods discussed in this thesis there were $0.9 - 1.2 \times 10^{11}$ protons per bunch. The bunch harmonic number is the time taken to encircle the ring divided by the bunch spacing, in other words it is the maximum number of bunches that could possibly be in the ring. The maximal bunch harmonic number is 3564 but this is not intended to be achieved since there are intentionally empty bunches. For the early running periods there were 200 - 300 bunches in the ring, which is only about 10% of the nominal for a 25 ns spacing. Nominal

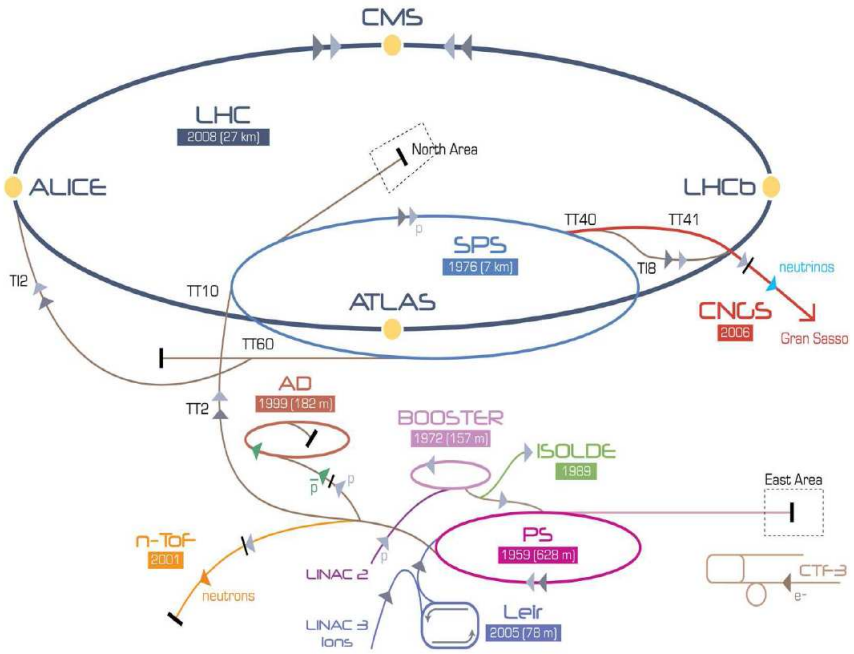

Figure 3.1: Schematic layout of the LHC complex. [27]

high luminosity of 10^{34} cm^{-2} s^{-1} has not yet been achieved but several different stable configurations have been used for early running with continually increasing luminosity. The event rate by which a given interaction will occur is $R = L\sigma$, where σ is the cross section for the process and L is the instantaneous Luminosity of the interaction. Running ended for the winter shutdown with a supplied integrated luminosity of nearly 45 pb^{-1}.

3.2 ATLAS

The LHC beams are collided at four locations where detectors have been installed. The detectors at these points are named ATLAS, CMS, LHCb and ALICE. The detector this thesis is based upon is A Toroidal LHC ApparatuS (ATLAS) [28]. The ATLAS collaboration was formed in 1992 and the ATLAS detector began taking 7 TeV collision data in 2010.

ATLAS is a multi-purpose detector that is capable of accurately measuring all known particles, except purely weakly interacting particles such as neutrinos. The ATLAS de-

tector is hermetic* to the level of the individual object resolution, identification efficiency and range. This ability implies it can indirectly measure the weakly interacting particles of each event by conservation of momentum. This is only possible in the transverse (radial) direction because the $\hat{z}$ components of the initial particles is unknown.

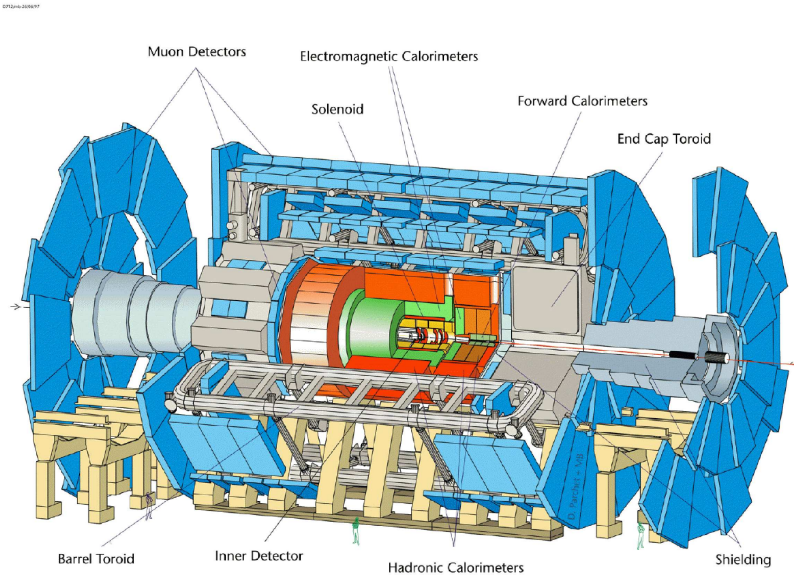

Figure 3.2: The different sections of the ATLAS detector. The detector is about 44 m in length, 22 m in height and weighs 7000 tons [29].

In order to detect such a variety of particles the ATLAS detector has several different types of subsystems, as illustrated in figure 3.2. The inner detector measures several interaction positions of charged particles to reconstruct tracks. These points or any detector component which measures an interaction position is referred to as a "hit". The momentum is measured via the radius of curvature of the path taken by the particle in the magnetic field created by the central solenoid. Similarly the Muon system measures the hit position of muons to reconstruct their path. The electromagnetic calorimetry systems measure the energy and incoming direction of electrons and photons. The hadronic calorimeters measure the energy and position of hadronic particles. The differing amounts of energy deposited in each calorimeter help greatly in particle identification, as displayed

*Hermetic is defined as the ability to detect particles in all directions from interaction point.

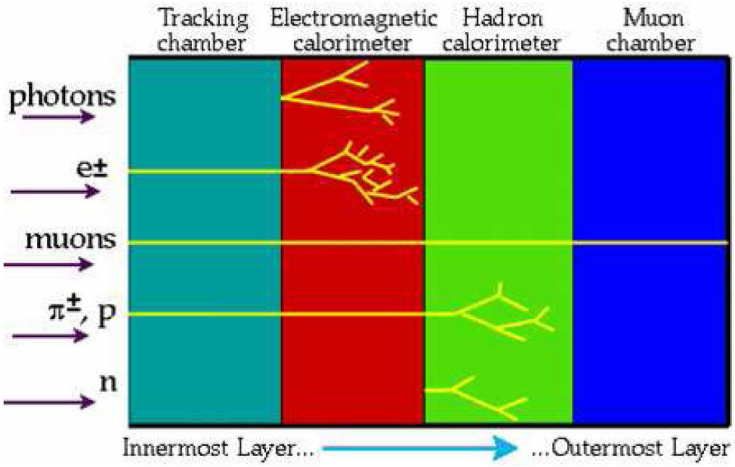

Figure 3.3: A schematic diagram which represents the various detector layers and how they can be used for particle identification. [30]

in figure 3.3.

The coordinate system of the ATLAS detector is set with a right handed Cartesian coordinate system, with the y-axis up, the x-axis toward the center of the LHC ring and the z axis along the beam. The origin of the azimuthal angle, $\phi = 0$, corresponds to the positive x-axis and increases clock-wise looking into the positive z direction. Transverse momentum, p_T, is defined as the momentum perpendicular to the LHC beam axis. The polar, θ, angle is measured from the positive z-axis. Pseudorapidity, η, is defined by

$$\eta = -\ln\left(\tan\frac{\theta}{2}\right). \tag{3.1}$$

With up to 0.7×10^9 interactions per second there is far too much data to record every event. A complicated trigger system is set up to trigger on events which are of interest. The trigger will have to reject nearly all events in order to reduce the rate of 40 MHz (25 ns bunch spacing) down to a manageable 100 Hz. The overall data taking efficiency for the ATLAS detector is approximately 94%.

3.2.1 The ATLAS Calorimeters

It is expected that quarks and gluons will readily be produced with high energy at the LHC. Quarks and gluons cannot propagate freely because they are not colour singlets.

In most cases they quickly hadronize into many colour singlet hadrons, such as pions. When a quark or gluon is produced with high energy, these hadrons are boosted into a collimated spray. This collimated spray is known as a jet. It is by detecting this jet that the 4-momentum of the original quark or gluon can be inferred.

High energy hadrons initiate particle showers when they come into contact with matter such as the ATLAS calorimeter. Because of the complexity of hadronic showers, there are several models. One of these is the spallation model, where hadronic showers are seen as the strong interactions between high momentum hadrons and a nucleon within the nuclei of the calorimeter material. These interactions can cause the nucleon to be ejected from the nucleus which can then travel and interact with other nuclei. Since the ejected particle will in general carry less momentum than the particle causing their ejection, the shower will broaden and die out.

The hadronic showering process is dominated by a succession of inelastic hadronic interactions. At high energy, these are characterized by multiparticle production and particle emission originating from nuclear decay of excited nuclei. Due to the relatively frequent generation of π^0's, there is also an electromagnetic component present in hadronic showers. The complexity of this process means that two hadronic showers originating from the same type of particle in the same calorimeter can be quite different.

Electrons interact with the material through the EM force instead the strong force as with hadrons. These interactions cause Bremsstrahlung and subsequent pair production from the emitted photon. As with hadronic showers the electromagnetic showers will broaden and die out.

To measure the energy deposited by these jets a series of electromagnetic and hadronic calorimeters are used [31]. These measure the energy the showers deposited in calorimetric regions by sampling the shower in the active regions. The calorimeters are segmented in η and ϕ, as well as in depth. There are four depth samplings in the EM calorimeter and three or four depth samplings in the hadronic calorimeter. The layout of the ATLAS

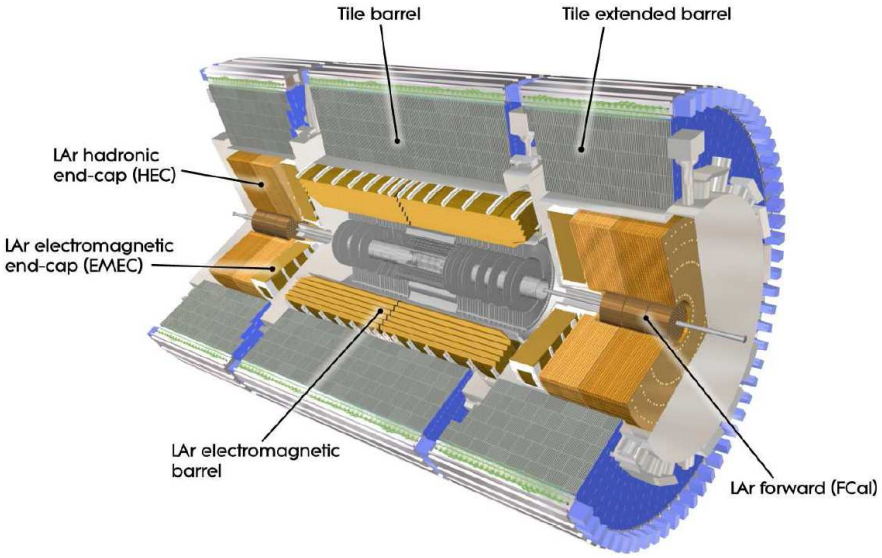

Figure 3.4: The different sections of the ATLAS calorimeter system. [32]

calorimeter system is shown in figure 3.4.

The electromagnetic calorimeter is a lead / liquid argon (LAr) sampling calorimeter. The lead layers serve as absorbers and the liquid argon is the active material for detection. It has a zig-zag accordion design to allow continuous azimuthal coverage with minimal density variation. The LAr electromagnetic barrel consists of two identical half-barrels of 3.2 m length which are joined at z = 0 to a precision of 4 mm. The EM barrel calorimeters are more than 22 radiation lengths thick for electrons. The endcaps are divided into two parts: an outer wheel covering the region $1.375 < |\eta| < 2.5$ and an inner wheel covering the region $2.5 < |\eta| < 3.2$. The performance of the electromagnetic calorimeter with data has been superb except for one issue. The vertical-cavity surface-emitting laser in the optical transmitter data links for the ATLAS liquid argon calorimeter have been suffering failures [33].

The Hadronic Barrel calorimeters have iron plate absorbers and plastic scintillator tiles for energy sampling. Scintillators work by the capture of the light radiated by the de-excitation of molecules in the material. The tile barrel is placed directly outside the LAr electromagnetic barrel and covers the region $|\eta| < 1.7$. The barrel part covers $|\eta| <$

1.0, while the extended barrel cover $0.8 < |\eta| < 1.7$. The Tile calorimeter has 99.1% [34] of its scintillator cells operational.

In the region $1.5 < |\eta| < 3.2$ two hadronic endcap calorimeters (HEC) have been built. Due to the higher radiation exposure which would burn out scintillators, the intrinsically radiation hard LAr technology has been chosen. Parallel Copper plates are used as absorber material with LAr in between.

The ATLAS EM calorimeters are expected to have an energy resolution† of [28],

$$\frac{\sigma_E}{E} = \frac{10\%}{\sqrt{E/GeV}} \oplus 70\% \ , \tag{3.2}$$

while the Hadronic calorimeters were designed for

$$\frac{\sigma_E}{E} = \frac{50\%}{\sqrt{E/GeV}} \oplus 3\% \ . \tag{3.3}$$

3.2.2 The ATLAS Inner Detector

The purpose of the inner detector (ID) is to measure the momentum and direction of charged particles as precisely as possible. If measurements are precise, secondary vertexes can be reconstructed and distinguished from the primary vertex. Secondary vertexes can result from the decay of long lived particles or from other beam interactions. A charged particle passing through a detecting component will be measured and recorded as a hit. A series of such hits can be reconstructed into a track. The momentum and the sign of the charge are determined by measuring the bending of the track in the r$\times\phi$ plane by the Lorentz force in the two Tesla magnetic field created by the inner solenoid. Due to the magnetic field, the track of a charged particle is described by a helix with 5 parameters. Three of these describe the velocity vector at the point of closest approach of the helix to the primary vertex. The remaining two are the impact parameters, d_0 and z_0, which

†$\sigma_X \equiv RMS(X^{reco} - X^{Truth})$

are the transverse and longitudinal coordinates of that point, respectively.

The hits are determined from interactions within the subsystems of the various detectors which cover up to $|\eta| = 2.5$. The subsystems of the ATLAS inner detector are depicted in figure 3.5.

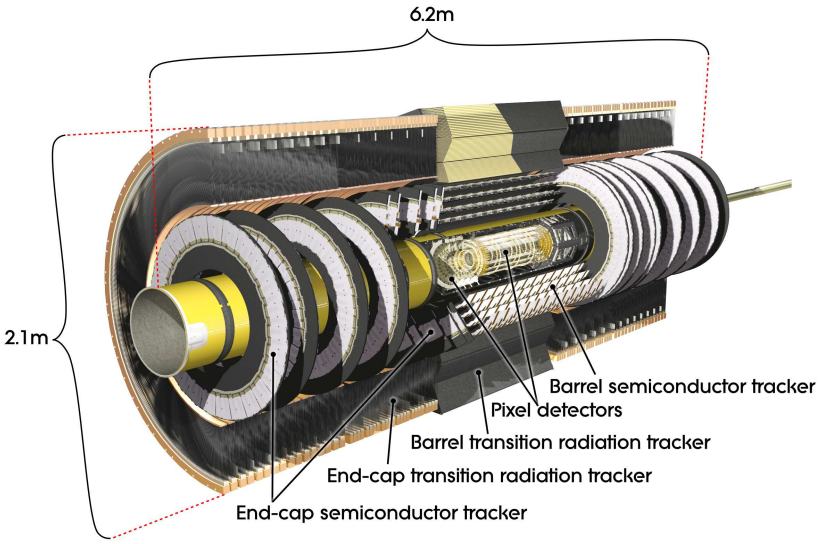

Figure 3.5: The different sections of the ATLAS inner detector. [32]

The pixel detector is the innermost part of the inner detector. It is designed to measure the position of the primary vertex, as well as the starting point of any charged track. It is a reverse-biased silicon wafer which is segmented into 50×400 μm pixels. The two dimensional array of the diodes is bump-bounded to sixteen flipped front-end readout chips, where the electric signal is amplified and compared to a threshold. The barrel part consists of three cylindrical layers, while three discs on each side are used for the endcaps.

Outside the pixel detector is the semiconductor tracker (SCT). The SCT extends the inner detector system by adding one barrel and two endcap silicon microstrip detectors. The silicon microstrips of the SCT detector are similar in technology to the pixel. The SCT measures particle position by detecting the electric charge liberated by a charged particle passing through a reverse-biased silicon diode. There are 4 barrel layers in the

central region and ringed endcaps to increase coverage.

Outside the SCT is the transition radiation tracker (TRT). The TRT is a compilation of about 370,000 drift chamber tubes containing 70% Xenon, 27% CO_2 and 3% Oxygen. Each 6 mm tube has the inside covered with aluminum to act as the cathode. There is a gold-plated tungsten wire down the middle to act as the readout anode. When a charged particle passes through the tube it ionizes the noble gas in the gas mixture inside. Most hits from a high momentum electron track are produced by the absorption of transition radiation photons in the gas mixture. Transition radiation is produced by relativistic charged particles when they cross the interface of two media of different dielectric constants. The emitted photons come from the homogeneous difference between the two inhomogeneous solutions of Maxwell's equations for the moving particle in each medium. The wire is charged so that the ions drift towards it and the point where the charged particle passes through the tube can thus be measured. Transition radiation photons generally lead to electronic pulses crossing a high threshold whereas pulses from particles which do not produce transition radiation usually only cross a low threshold. This fact can be used to distinguish electrons from other particles, most importantly charged pions. The TRT only covers the pseudorapidity region $|\eta| < 2$.

One of the first inner detector issues to address with data is the alignment [35]. Alignment is essentially the knowledge of where the detector components are. The results with 7 TeV data collected during 2010 show that the current alignment precision is about 17 μm for the Pixel barrel sensors. The estimation of the tracking systematics associated with the alignment from data is currently in progress. As the 7 TeV data accumulates progressively better alignments will be obtained.

The components of each sub-detector have been timed with a precision of 1-2 ns. The average noise occupancy has been measured to be $\approx 10^{-10}$ hits per channel per BC for the Pixel Detector and $\approx 10^{-5}$ hits per channel per BC for the SCT. The intrinsic hit efficiency has been measured to be close to 100% for the silicon detectors and 97.2 $\pm$

0.5% for the TRT.

3.2.3 The ATLAS Muon System

For particles with no strong interactions and large mass there is a range of energy in which they are minimally ionizing. This means that the mean rate of energy loss from ionization is low. Since muons are minimal ionizing particles, they traverse the inner detector and the calorimeters relatively undisturbed. This implies an additional system for muon detection. The muon system is the outermost part of ATLAS and is similar to the inner detector in that it uses several differing subdetectors to reconstruct tracks bent by a magnetic field. There is a large variety of the muon subsystems which form a relatively complex and inhomogeneous layout. Because of this layout, there are cases with large distances between measuring stations and these induce significant extrapolation uncertainties. The subsystems of the muon detector are illustrated in figure 3.6.

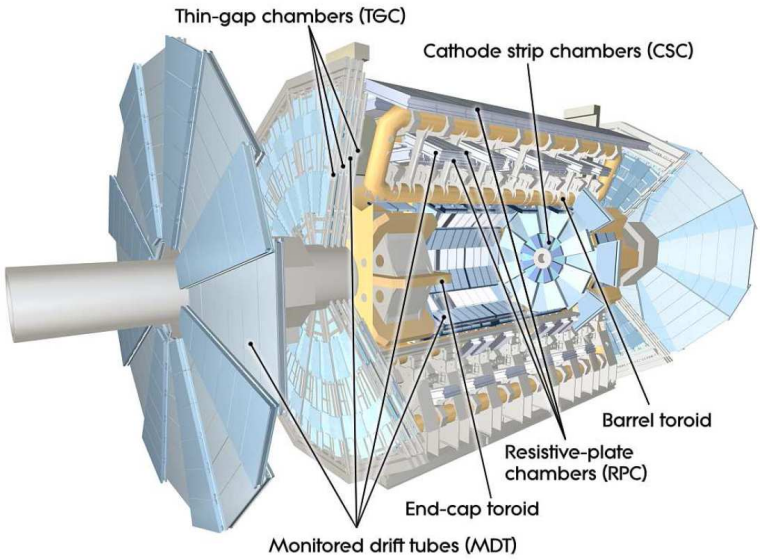

Figure 3.6: The different sections of the ATLAS muon system. [32]

The magnetic field for the bending of the tracks is generated by the toroid magnet system. There is high inhomogeneity in the magnetic field as depicted in figure 3.7. This forbids simple analytical shapes for the muon tracks as with the inner detector.

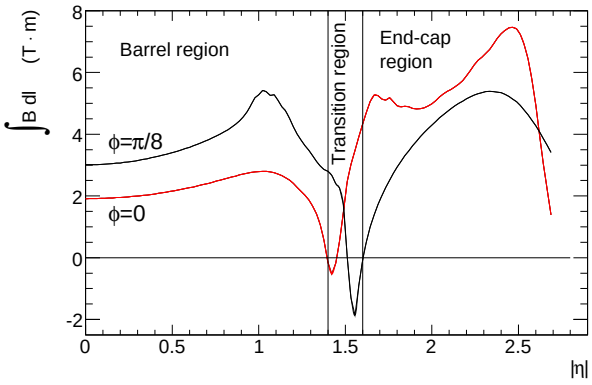

Figure 3.7: The magnetic field of the ATLAS muon system. [36]

Four different gaseous detector technologies are used in the Muon System. These are the monitored drift tubes (MDT), the cathode strip chambers (CSC), the thin-gap chambers (TGC) and the resistive plate chambers (RPC).

The MDTs are used to provide precision measurements of the track coordinates. These chambers consist of several layers of drift tubes that measure the drift time of an electron produced by the ionizing muon. Like the TRT the tubes are made of aluminium but they are much larger (30 mm) and the gas in the tubes consists of 93% Ar and 7% CO_2.

In the forward region ($2.0 < |\eta| < 2.7$), the CSCs are used in the innermost muon tracking layer. They are multiwire proportional chambers with cathode planes segmented into strips in orthogonal directions. The induced-charge distributions on the strips are used to determined the track coordinates.

The RPCs are gaseous detectors which do not use a wire but two resistive plates with a distance of 2 mm as parallel electrodes. Electron avalanches are produced along the ionizing track towards the anode due to the electric field produced.

The TGCs are multiwire proportional chambers, which function similar to the CSCs. To achieve a better time resolution, they have a smaller anode to cathode distance and a different gas mixture. In addition to the time measurement, the TGCs also determine the azimuthal coordinate of a muon track to complement the measurement of the MDTs. The inner layer of the MDTs is complemented by two layers of TGCs, while the middle

layer is complemented by seven TGC layers. The muon subsystems work complementary to cover the $|\eta| < 2.7$ range. There are however some gaps in this coverage such as at $\eta \approx 0$ where there are no muon detectors due to cabling. Another large region is the $1 < |\eta| < 1.3$ region where there are a limited number of chambers in the transition region between horizontally laid and vertically laid chambers. This region can be seen in figure 3.8.

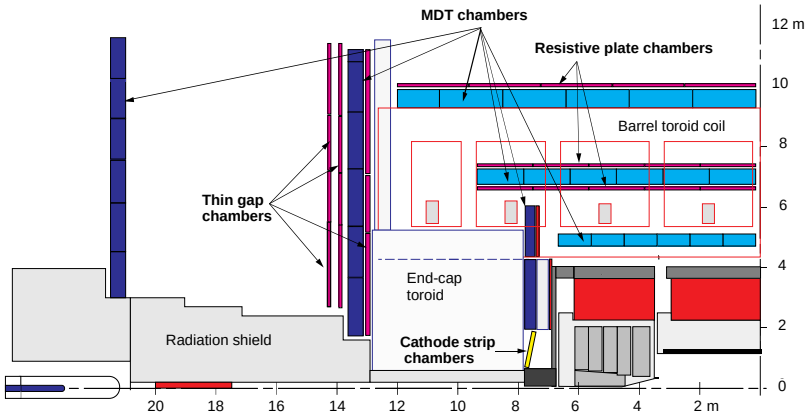

Figure 3.8: The different sections of the ATLAS muon system. [36]

3.2.4 The Trigger System

The collisions at the LHC provide an event rate of approximately 1 GHz at the design luminosity. For each event ATLAS can record about 1.5 megabytes of data. In order to store data from every collision, this would mean 1.5 petabytes of data would have to be recorded every second in ATLAS. This is impossible with the current technology in electronics systems and storage elements. Most events created in ATLAS are of low momentum transfer and are therefore not interesting.

To select events that are interesting, a three level trigger system is designed for ATLAS. This determines whether an event shall be recorded while reducing the event rate several orders of magnitude in order to match the capacity of the data acquisition (DAQ) system. The first triggering level (LVL1) is composed of hardware based selection com-

ponents. Software based selections for the second level (LVL2) and third level (Event Filter) triggers allow for more complicated algorithmic selections. Each successive level of trigger has a progressively more complex selection to determine physics signatures of interest and therefore requires more time to reach a decision. A schematic diagram of the ATLAS trigger system is presented in figure 3.9.

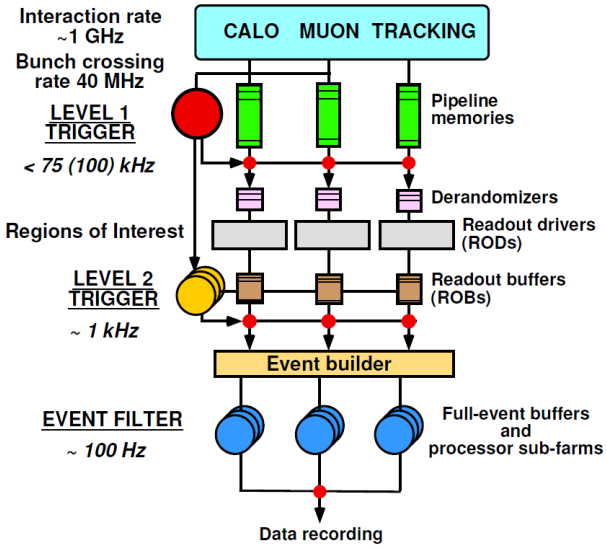

Figure 3.9: Schematic diagram of the ATLAS trigger system. [28]

The LVL1 trigger only uses information from the calorimeters and muon spectrometer and reduces the data rate from ≈1 GHz to ≈75 kHz. The time required to make a decision is known as latency and is ≈2 μs for the LVL1 trigger. Once an event is selected, the LVL1 trigger sends information regarding where in the ATLAS detector the interesting physics object may be to the Region of Interest Builder (RoIB). The LVL2 trigger uses these RoIs to determine which regions of the detector to examine and therefore minimize the time needed to make a trigger decision. The RoI correspond to 2-4% of the full event data so the processing time saved by this simplification is significant. The LVL2 trigger can make use of the other subdetectors if the RoI signature indicates that they may be useful. The LVL2 trigger reduces the data rate from ≈75 kHz to about ≈3 kHz with an average latency of ≈ 40 ms [37].

The final selection of an interesting physics event which is to be recorded and used

for subsequent detailed offline analyses is made by the event filter. The latency is ≈1 s, so several processors are used in parallel in order to produce a data rate of ≈ 100 Hz. The trigger selection is configured via a trigger menu which defines trigger chains. A trigger chain specifies a sequence of reconstruction and selection algorithms which start from a L1 trigger and lead to a specific trigger signature. If the requirements for one or more trigger signatures are satisfied, event recording is triggered. Prescale factors can be applied to each L1 trigger and each HLT chain. A series of L1 and HLT prescale sets are defined to accompany each menu. There are between 200 and 500 chains defined in the current trigger menus. In the final analysis for this thesis specific single muon triggers are used. These triggers consume $< 1\%$ of the available bandwidth.

Chapter 4

Searches for SUSY

As motivated previously SUSY searches in this thesis will focus on the R-Parity conserving mSUGRA models. Other specific models can be motivated as well and are being pursued by the ATLAS collaboration. mSUGRA is expected to phenomenologically represent a variety of R-Parity conserving MSSM scenarios. In general the MSSM can have many signatures which differ from mSUGRA [38] and it is unwise to expect such a simplified model to represent reality. This is the motivation for SUSY searches to be aimed at generic signatures which are not tuned to any model.

mSUGRA searches in ATLAS all assume the presence of missing transverse energy, $\not{E}_T$, from the purely weakly interacting LSPs. Several hard jets and leptons from the cascade decays to the LSPs are also typical of such events. This prompts the studies to be divided phenomenologically into the # Jets $\times$ # Leptons plane [36]. The expected discovery reach for the ATLAS benchmark searches of this can be seen in figure 4.1. As can be seen, differing topologies have differing reaches for differing points. This is due to the relative advantages and disadvantages that arise in different searches.

One of the most obvious differences is the dominant source of background. This thesis deals mainly with the 4 jets, 1 lepton selection. The requirement of a lepton eliminates the difficult to model QCD multijet background leaving $t\bar{t}$ as the dominate background.

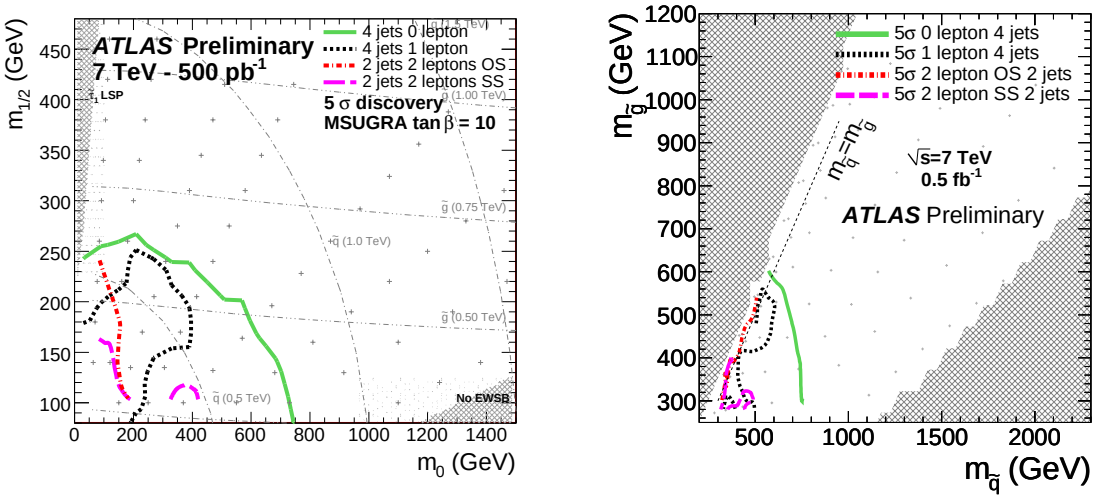

Figure 4.1: The 5 σ discovery reach for various ATLAS mSUGRA searches with an integrated luminosity of 500 pb^{-1}. The $m_0 \times m_{1/2}$ plane (left) and the $m_{\tilde{q}} \times m_{\tilde{g}}$ plane (right) are shown for $tan(\beta) = 10$, A_0 = -400 GeV and positive μ. [39]

The secondary background for this model is W+Jets production which has similar issues to the QCD multijet. Events with τ leptons are taken as a special case because of the difficulty in reconstruction. This prompts the assignment of the symbol ℓ to represent either an electron or muon.

4.1 SUSY Phenomenology

The assumption of R-Parity conservation implies that sparticles will be produced in pairs. Again because of R-Parity conservation, all sparticles must decay into an odd number (usually 1) of sparticles with some additional particles. Since the LSP is stable and all sparticles can follow a decay chain to it, all SUSY final states end in at least two LSPs. Since these are undetectable they lead to $\not{E}_T$.

The masses of the left handed states are different from the masses of the right handed states because the renormalization group equations of the left handed doublets have an additional SU(2) gaugino mass contribution compared to the right handed singlets. In general the squarks are heavier than the sleptons.

The masses of the sparticles depend on the mSUGRA parameters in a way which can be roughly understood [40]. If m_0 increases, all masses rise considerably except the lightest Higgs Boson and the gauginos, which are nearly constant. All masses increase with increasing $m_{\frac{1}{2}}$. The masses of the gauginos and the first two generations of sfermions hardly depend on $tan(\beta)$. The mass of the lightest Higgs Boson is constant for large $tan(\beta)$, but drops considerably if $tan(\beta)$ becomes small. Sfermions masses of the third generation have an approximate $-A_0^2$ dependence with a maximum that is shifted to positive values of A_0. The mass of the lightest Higgs Boson is higher for lower A_0. The sign of μ has little effect compared to the other parameters.

The proton parton distribution function for high energy proton-proton collisions is biased toward gluon interactions. This means that the production of gluinos and squarks by gluon-gluon and quark-gluon fusions will dominate SUSY production at the LHC. The dominant production diagrams are shown in figure 4.2. There are specific models where this is not the case; for example, models with all squark and gluino masses above a few TeV will have such production kinematically suppressed. This thesis focuses on mSUGRA for low m_0 and $m_{\frac{1}{2}}$ values and therefore relatively low squark and gluino masses. The choice of low mass is to allow for early limits to be set or early discoveries to be made. Low mass points typically have higher cross sections and therefore one would expect a possible observation even with limited integrated luminosity.

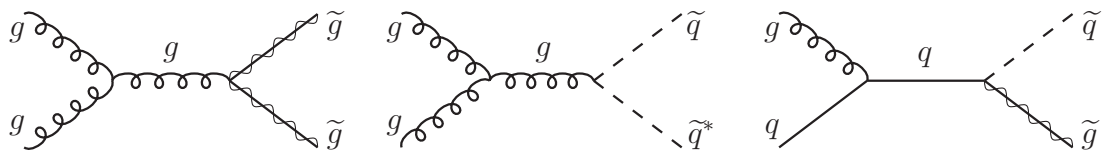

Figure 4.2: Feynman diagrams for gluino and squark production at the LHC from gluon-gluon and gluon-quark fusion.

An example of such low mass point just above current limits is the ATLAS SUSY benchmark point named SU4. SU4 is an mSUGRA point defined by the following parameters: m_0 = 200 GeV, $m_{\frac{1}{2}}$ = 160 GeV, A_0 = -400 GeV, $tan(\beta)$ = 10, and $sign(\mu) >$

0. For this model point, the masses of the strongly interacting particles are in the range of 410 to 420 GeV.

For cases like SU4 the gluino is the heaviest gaugino and does not mix. Gluino decays must proceed through a squark. If the on-shell $\widetilde{g} \to q\widetilde{q}$ is kinematically allowed it will dominate. Otherwise the so called three body decay will proceed through a virtual quark. Since the stop and sbottom squarks are likely the lightest due to large Yukawa couplings of their supersymmetric partners, they will dominate the decays and subsequently produce tops and bottoms in abundance. This is the motivation for SUSY searches which focus on identifying bottom quarks.

If the decay $\widetilde{q} \to q\widetilde{g}$ is kinematically allowed it will dominate the squark decays similarly to above. If not, the squarks will decay into a quark and a chargino or neutralino: $\widetilde{q} \to q'\widetilde{\chi}_i^{\pm}$ or $\widetilde{q} \to q\widetilde{\chi}_i^0$. Each chargino and neutralino contains some content from each of the electroweak gauginos ($\widetilde{B}, \widetilde{W}^0, \widetilde{W}^{\pm}$) after their mixing. The mixing content determines their weak interaction strength to (s)fermion partners. The decay to the LSP is favoured for right handed squarks since the $\widetilde{\chi}_1^0$ LSP is mostly bino, $\widetilde{B}$. Alternatively, left handed squarks often prefer decays to the heavier charginos or neutralinos because the wino, $\widetilde{W}$, coupling is stronger. This coupling is dependent on the chirality mixing of the squarks.

To the level that sleptons are lighter than squarks the $\widetilde{\chi}_i^0 \to \ell\widetilde{\ell}(\nu\widetilde{\nu})$ and the $\widetilde{\chi}_i^{\pm} \to \nu\widetilde{\ell}(\ell\widetilde{\nu})$ decays will dominate neutralino and chargino decay. They can also decay into their lower mass counterparts through Z or h, or into one another through the W Boson.

For a particular chargino or neutralino it may be that all of these two body decays are kinematically forbidden. This is more likely the case for $\widetilde{\chi}_2^0$ and $\widetilde{\chi}_1^{\pm}$. In this case the decays occur through three body decays:

$$\widetilde{\chi}_i^0 \to ff\widetilde{\chi}_j^0,\ \widetilde{\chi}_i^0 \to ff'\widetilde{\chi}_j^{\pm},\ \widetilde{\chi}_i^{\pm} \to ff'\widetilde{\chi}_j^0,\ \widetilde{\chi}_2^{\pm} \to ff\widetilde{\chi}_1^{\pm}, \tag{4.1}$$

where f represents a SM Fermion with f and f' distinct members of the same SU(2) multiplet.

Sleptons typically decay via two-body decays of weak interaction strength:

$$\widetilde{\ell} \to \ell\widetilde{\chi}_i^0,\ \widetilde{\ell} \to \nu\widetilde{\chi}_i^{\pm},\ \widetilde{\nu} \to \nu\widetilde{\chi}_i^0,\ \widetilde{\nu} \to \ell\widetilde{\chi}_i^{\pm}\ . \tag{4.2}$$

In most cases decays to the $\widetilde{\chi}_1^0$ are kinematically allowed and therefore dominate. Because the stau, $\widetilde{\tau}$, is expected to be the lightest slepton, its production can be favoured. Its subsequent decays therefore produces signatures with taus.

Depending on the particular model and the chosen parameters, the decay chains from squarks and gluinos to the LSP can significantly differ. In addition to the LSP the decay chains must end in SM fermions. This implies that decay chains produce multiple jets and leptons. For this reason the studies are divided phenomenologically into the # Jets $\times$ # Leptons plane.

Channels which include taus may have slightly larger production cross sections but electrons and muons are preferred for experimental reason. Taus are much more difficult to reconstruct than electrons and muons, which implies that they will not be well understood in early data taking times. For this reason only channels selecting electrons and muons will be explored in this thesis. A typical production and decay chain for the types of processes focused on in this thesis is shown in figure 4.3.

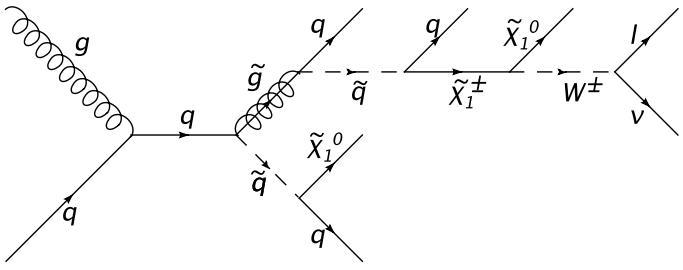

Figure 4.3: Example Feynman diagram for the production and decay of a typical mSUGRA event discussed in this thesis.

4.2 SUSY Backgrounds

In all searches there are events which are misidentified as signal because they pass the selection cuts. These are typically events with a large cross section or similar topology to that of the signal. This thesis focuses on selections which require a single lepton so one would expect backgrounds with one lepton from the hard process to dominate. A corresponding SUSY signal is typically a pair of squarks which decay through chains producing a ℓ, several jets and two LSPs. High $\not{E}_T$ is a typical topological cut to select events where there were weakly interacting particles. For SUSY one expects the two LSPs to be a large source of $\not{E}_T$. The neutrinos are the only purely weakly interacting particle of the SM but they can be produced with high energy from the decay of a W or Z Boson. A W Boson decay of this sort will also produce an energetic lepton. In this way W Boson events are a background to SUSY searches. Due to the cascade decays in SUSY one would also like to select events with high jet multiplicity.

$t\bar{t}$ production is by far the dominant background for tight selections of one lepton SUSY. For looser selections W production with additional QCD jets can dominate. Smaller contributions come from Z+Jets, Di-boson, single top and QCD processes.

4.2.1 $t\bar{t}$

At hadron colliders, such as the LHC, top quarks are produced mainly in $t\bar{t}$ pairs. At the LHC, the hard process $gg \rightarrow t\bar{t}$ comprises the majority of the production. The top quark decay is mediated by the electroweak interaction. Since flavour changing neutral currents are forbidden in the Standard Model due to the GIM mechanism [41], the decays of the top quark involving the Z or γ Bosons are highly suppressed and can only occur in higher order diagrams. Therefore, the top quark decay vertex must involve a W Boson. The three final states are therefore: $t \rightarrow Wb$, $t \rightarrow Ws$ and $t \rightarrow Wd$.

The full width, $\Gamma(t \rightarrow X)$, can be approximated by the partial width of $\Gamma(t \rightarrow Wb)$.

This is because the Cabibbo-Kobayashi-Maskawa (CKM) matrix element linking top and bottom quarks, V_{tb}, is nearly one. Therefore, the $t \to Wb$ decay completely dominates with a predicted branching ratio, $BR(t \to Wb)$, greater than 99.8%.

From a $t\bar{t}$ pair the decays almost always result with two bottom quarks and two W Bosons. Because of this the $t\bar{t}$ decay chains can be classified according to how the W Boson decays. A W can decay leptonically to a lepton and its associated neutrino or hadronically to a pair of quark weak isospin partners. The commonly named decay channels of a $t\bar{t}$ pair are the Semileptonic, Fully Hadronic and Di-leptonic channels. In the Semileptonic channel, one of the W Bosons decays leptonically (W$\to \ell\nu$) and the other one hadronically (W$\to jj$) giving a final state topology of $t\bar{t} \to (jjb)(\ell\nu b)$. Defining ℓ to be only electrons and muons, the branching ratio is BR $\approx$ 2 x 0.2132 x 0.676 $\approx$ 28.8%*. In the Di-leptonic channel, both W Bosons decay leptonically giving a branching ratio of BR $\approx$ 0.2132 x 0.2132 $\approx$ 4.5%. In the Fully Hadronic channel, both W Bosons decay hadronically leaving a final state topology of $t\bar{t} \to (jjb)(jjb)$. The branching ratio for the Fully Hadronic channel is the largest of the three being BR $\approx$ 0.676 x 0.676 $\approx$ 45.7%. These do not add up to 100% because τ leptons are excluded and only electrons and muons were considered. The various τ decay chains are illustrated along with the others in figure 4.4. The term Leptonic $t\bar{t}$ is used to refer to all non-Fully Hadronic decays.

The Semileptonic channel is the dominant background for the single ℓ SUSY searches discussed in this thesis. This is because it has a high p_T lepton, many jets and a neutrino to give high $\not{E}_T$. As will be discussed later, cuts designed to eliminate events where the ℓ comes from a W Boson will change the background composition such that the Di-leptonic $t\bar{t}$ background is more important.

*Values taken from [4].

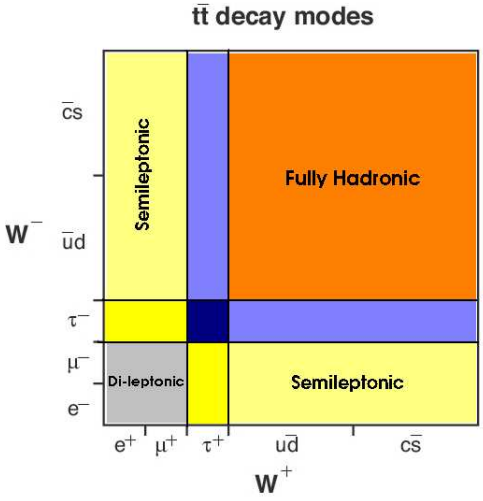

Figure 4.4: The various branching ratios of the $t\bar{t}$ decay chain. The area represents the ratio of the cross section taken by each chain.

4.2.2 W+Jets

The mass of the W Boson is currently measured to be $m_W = 80.399 \pm 0.025$ GeV [4]. The W can decay to any weak isospin pair, but the most interesting for single ℓ SUSY searches are the W$\rightarrow e\nu_e$ and the W$\rightarrow \mu\nu_\mu$ decays. The hadronic decays are of little importance because they do not have a ℓ in the hard process. There is some contamination to these channels from the W$\rightarrow \tau\nu_\tau \rightarrow \ell\nu_\ell\nu_\tau$ decay.

The W$\rightarrow \ell\nu$ decays are important backgrounds for SUSY searches with one ℓ because they have a similar topology. The ℓ is often high in p_T since it comes from the decay of the heavy W particle. The ν is energetic for the same reason and is undetectable so will provide a significant source of $\not{E}_T$.

The measurement of the W Boson production inclusive cross section was one of the first measurements at the LHC so the cross section is known [42]. Additionally, the cross sections can be evaluated by means of Monte Carlo methods such as the program FEWZ [43]. FEWZ is designed to calculate the inclusive cross section at next-to-next-to-leading order (NNLO) for the W and Z Bosons.

The production cross section for W Bosons with additional jets decreases as the number of jets increases. This implies that the background can be significantly reduced by a

high jet multiplicity requirement.

The major issue with this background is that it is difficult to accurately generate MC which one would expect to represent reality. Until very recently multijet MC samples were only available at leading order (LO) in α_s for a limited number of outgoing particles.

As can be seen from figure 4.5 the cross sections are quite different between LO and NLO calculations. This implies that there is a significant portion of the sample which is not output from a LO generator. To compensate for this, analyses often assume that Standard Model backgrounds can be measured in SUSY-free regions to fix normalizations and then employ LO MC to extrapolate to kinematic regions where SUSY signal is expected. Hence, an implicit assumption in those analyses is that LO distributions have correct shapes and that higher-order QCD effects provide kinematics independent renormalization. This assumption is valid to some extent but not true in general [44].

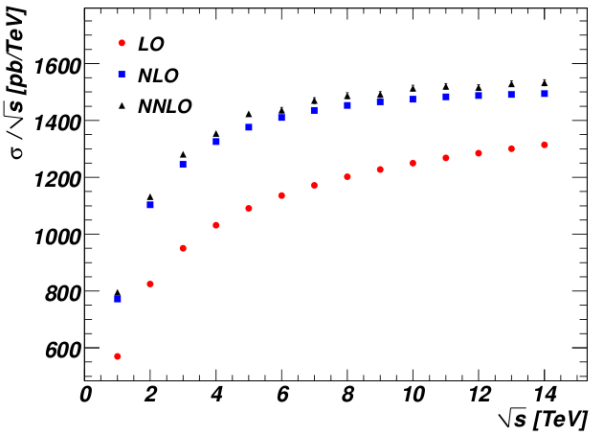

Figure 4.5: W Boson production inclusive cross section divided by center-of-mass energy ($\sqrt{s}$) as a function of $\sqrt{s}$. [45]

This extrapolation is done by multiplying the LO sample by a normalization factor called a k-factor. These k-factors are simply the NNLO cross section divided by the LO cross section. These k-factors are dependent on the particular final topology because it selects particular phase space regions.

4.2.3 Minor Backgrounds

As mentioned before, the choice of final state selects the dominant backgrounds. For a search without leptons the dominant background is the QCD multijet production. This background is difficult to model for essentially the same reasons as the W+Jets. Applying the requirement of one lepton will significantly reduce this background because the reconstructed lepton must be faked by a jet. Fake leptons are an expected phenomena so there are minor contributions from QCD multijet production to the single lepton background. Another background caused by fake leptons is the Z+Jets background where Z$\rightarrow \nu\nu$. This can supply significant missing energy but the requirement for a fake lepton significantly reduces its prevalence. The QCD background is much more dominant because of its large cross section.

Other minor backgrounds come from the opposite effect, where a lepton is missed. For example Z+Jets where Z$\rightarrow \ell\ell$ has a similar topology to W+Jets when one of the ℓ is not reconstructed. For LHC energies the Z+Jets cross section is about an order of magnitude less than that for W+Jets. This is the major reason why W+Jets is the more dominant background. The Drell-Yan production of leptons through virtual Z/γ will contribute with a similar topology to Z+Jets.

Single top production where the top decays leptonically also contributes for essentially the same reasons as $t\bar{t}$. This is a relatively minor background mainly due to the low cross section. The dominant production chain is t-channel followed closely by W-gluon fusion. The s-channel production is very small

Electroweak Di-boson production can have high p_T leptons as well as $\not{E}_T$. Again this is only a minor background due to the relatively low cross section. WW production is the dominant background coming from Di-boson production.

4.3 Current Limits

There have already been several SUSY searches but no evidence has yet been found. The sources of limits on the parameters in SUSY can be divided into direct and indirect measurements. There are virtual sparticle effects on several Standard Model observables [46].

A typical example of a measurement which restricts the parameter space of SUSY is the limit on $BR(b \rightarrow s\gamma)$. As with many indirect limits theoretical motivations existed before the experimental confirmation of the values [47]. In the limit of exact supersymmetry, any magnetic moment-transition operator vanishes [48] and therefore $BR(b \rightarrow s\gamma) = 0$. As SUSY breaking terms are turned on, the rate for the decay $b \rightarrow s\gamma$ no longer vanishes, but it can still be considerably suppressed by the approximate cancellation.

Restrictions can be made if one assumes that the LSP is the dark matter particle indicated by Cosmology and Astrophysics [49]. The cold dark matter density of the universe is,

$$\rho_{DM} \approx 1.2 \times 10^{-6} \frac{GeV}{cm^3}. \tag{4.3}$$

This measurement is of limited use when building models or trying to predict the mass of the LSP. This is because of the freedom to tune to that particular density by changing the interaction strengths or the scale for R-Parity breaking.

The first mass limits for squarks and gluinos were made at CERN by the UA1 and UA2 experiments at the SPS. LEP later set very strong limits on sleptons and charginos which are still relevant today [50]. Recently the D0 and CDF experiment extended the limits for $\widetilde{\chi}_2^0$ and $\widetilde{\chi}_1^{\pm}$ as well as quark-gluon production. Figure 4.6 shows the current exclusion limits from these experiments for a mSUGRA point with A_0=0, $tan(\beta)$=3 and $sign(\mu)$ positive for the left plot and negative for the right. The left plot shows the $m_0 \times m_{\frac{1}{2}}$ plane excluded by the combination of the D0 (green) and LEP (grey) searches.

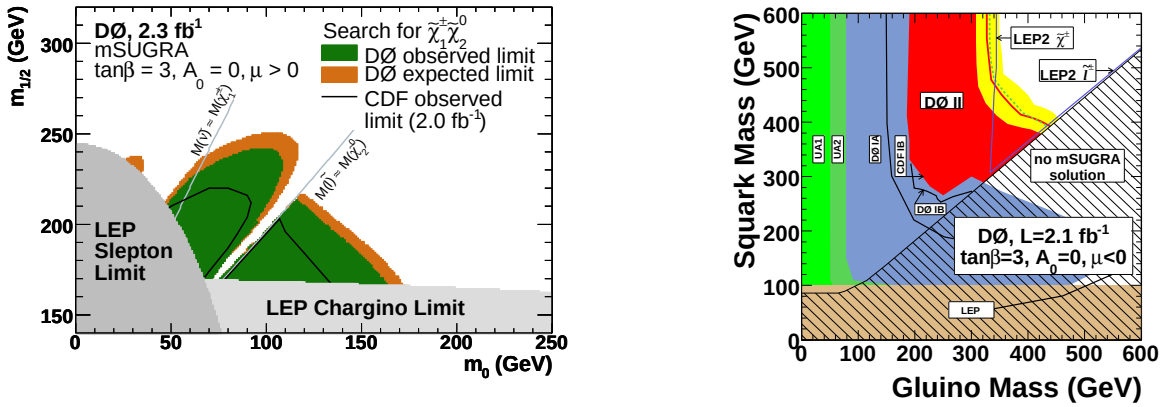

Figure 4.6: Current limits on mSUGRA for direct observation in collider experiments. The left plot [51] shows the limits in the $m_0 \times m_{\frac{1}{2}}$ plane while the right plot [52] shows the $m_{gluino} \times m_{squark}$ plane.

A previous CDF measurement is represented by the black line.

The right plot in figure 4.6 shows excluded regions at the 95% C.L. in the gluino and squark mass plane. The results for several experiments are shown. The red (dotted green) line is the limit of the observed (expected) excluded region by D0, which is currently the best exclusion. The band specified by yellow shows the effect of the parton distribution function choice and of the variation of renormalization and factorization scale by a factor of two. The dark red region therefore represents the most conservative limiting scenario. The two blue lines indicate the indirect limits inferred from the LEP2 chargino and slepton searches [53]. The region where no mSUGRA solution can be found is shown hatched.

This 95% C.L. exclusion gives lower limits of 379 GeV and 308 GeV on the squark and gluino masses, respectively. It should be kept in mind that these limits depend on the model and the parameter choice.

4.4 Signal Significance and Limit Calculation

Uncertainties on the background are incorporated in the significance by convoluting the Poisson probability that the background fluctuates to the observed signal with a Gaussian background probability density function $G(b; N_b, \delta N_b)$ with mean N_b and standard deviation δN_b [54]. Given these assumptions, the probability, P, that the background fluctuates by chance to the measured value N_{data} or above is given by:

$$P = \frac{\int_0^\infty G(b; N_b, \delta N_b) \sum_{i=N_{data}}^\infty \frac{e^{-b} b^i}{i!}}{\int_0^\infty G(b; N_b, \delta N_b) \sum_{i=0}^\infty \frac{e^{-b} b^i}{i!}}. \tag{4.4}$$

If this Gaussian probability density function G is replaced by a Dirac delta function $\delta(bNb)$, the estimator P results in a usual Poisson probability. This can be cast as a standard deviation, σ, through the transform,

$$\sigma = \sqrt{2} erf^{-1}(1 - 2P). \tag{4.5}$$

The raw numbers of signal, S, and background, B, are often used as crude estimates on the significance. Maximizing $\frac{S}{B}$ in tandem with $\frac{S}{\sqrt{B}}$ will often result in the maximum of σ within errors. This method is useful for optimizations but not acceptable for limit setting.

Limits will be calculated with a negative Poisson log-likelihood ratio test statistic [55]. If the estimated amount of signal is s, the estimated background is b and the number of observed candidates is d the likelihood ratio can be written as

$$X = \frac{e^{-(s+b)}(s+b)^d}{d!} \Big/ \frac{e^{-b} b^d}{d!} \quad . \tag{4.6}$$

To compute the probability density function of X one convolutes it with a Gaussian as in equation 4.4 to accommodate for systematic error. This results in a semi-frequentist approach where points are drawn at random from a Poisson parent distribution but

nuisance parameters are handled in a Bayesian model by the assumption of a Gaussian distribution.

The exclusion limit is calculated as the % of the resulting probability density function past a given value. For expected limits this value is taken as the mean of the background only probability density function. For the observed limit, this value is taken from measurements.

Chapter 5

Monte Carlo Production and Reconstruction

Monte Carlo (MC) production is a very important and sophisticated method for predicting what one expects to see in the ATLAS detector. Monte Carlo algorithms are a commonly used class of computational algorithms for simulating the behaviour of various nondeterministic physical and mathematical systems. Several different types of Monte Carlo algorithms are used to perform Monte Carlo Production.

For proton-proton collisions at the LHC, precise theory is only known for the parton interactions with specified external lines. Additionally the theory of parton interactions is only calculable to a few coupling orders at most. Each MC event takes a pseudo-random point in the parameter space for the external lines. The ensemble of such points will represent a collection of data. MC algorithms are also used to sample the space in parameterized particle interaction and detector response functions.

In order to produce the best possible Monte Carlo events on which to perform analyses, a full chain of steps needs to be taken. The steps for this production are shown in figure 5.1. The generation stage is where the particle four vectors are created. The simulation and digitization stages serve to add a model of the detector in order to reproduce

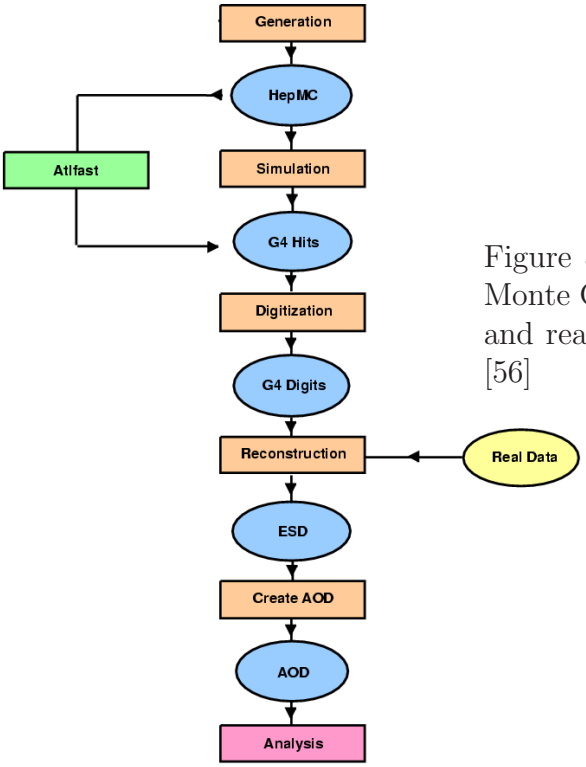

Figure 5.1: Schematic representation of the ATLAS Monte Carlo production chain. Both GEANT4 digits and real data are reconstructed as the same output. [56]

detector conditions. The reconstruction stage is where the detector measurements are interpreted as objects like jets and leptons. The reconstruction is the same for data and MC. Because of the complexity and time MC production requires, especially the detector simulation stage, centrally produced official samples from the ATLAS Monte Carlo Group will be used for most studies. However, some samples used in this thesis were produced privately and these samples will be clearly identified.

The simulation stage can be hastened by using ATLFAST-II which provides a faster simulation of the calorimeter. Since the simulation of the calorimeter in the full chain takes the most time, using a parameterized version can decrease the average simulation time per event. This loss of sophistication and therefore accuracy, is often well worth the amount of time it saves.

The general software framework for all ATLAS analyses is Athena. All steps in the production chain are done within this framework except for a few generators. Athena is a control framework and is a concrete implementation of an underlying architecture called

Gaudi [57].

5.1 Monte Carlo Generation

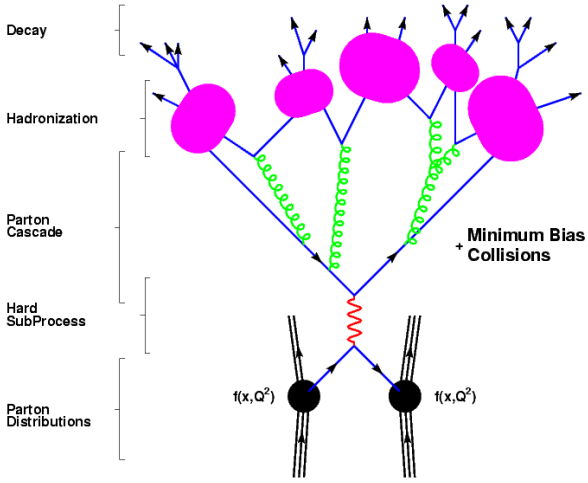

Figure 5.2: Schematic diagram of the generation for a Monte Carlo event [58].

Generation refers to the production of particle 4-vectors for specified physics processes. Generation of an event in a Monte Carlo p-p collision is done in several steps. A simplistic tree level version of generation is summarized in figure 5.2 to illustrate the steps of generation. First, two partons (one from each proton) collide to produce the hard subprocess which then forms two final state particles. The energy and type of each parton is determined by the Parton Distribution Function of the proton at the so called Factorization Scale. A simple Feynman diagram such as this is referred to as a 2 to 2 process because the 2 initial state particles collide to form 2 final state particles. The initial sate particles can radiate gluons and photons before the interaction; this is called Initial State Radiation (ISR). Similarly the final state particles can produce Final State Radiation (FSR) in the parton cascade.

The parton cascade is the process where quickly decaying particles such as the top decay. Radiation can also occur in the parton cascade which is why it is equivalently called the parton shower. The parton shower represents an approximate perturbative

treatment of QCD dynamics at scales of momentum transfer greater than a cut off which is typically of order 1 GeV^2. Below this scale particles undergo hadronization to form jets of hadrons. These hadrons are mostly unstable and therefore undergo further decays.

Any two of the proton's partons can have the hard interaction while the remaining partons are still involved in the process due to colour connection. The remaining partons from the proton no longer form a colour singlet and must therefore hadronize to form the underlying event (UE). Other proton-proton collisions that are in the same or previous bunch crossings but detected at the same time are referred to as pile-up. Along with the underlying event, pile-up is a major experimental difficulty because it is difficult to separate this from the interesting "hard" process which is to be measured. In addition there is another similar phenomena called Multiple Parton interactions (MPI). This is when two partons from each of the same two protons have a hard scatter. UE and MPI are modelled by the generator while pile-up must be added by overlaying minimum bias events. Pile-up which comes from protons in the same bunch is referred to as "in time pile-up" and pile-up from other bunch crossings is referred to as "out of time pile-up".

There are many event generators available. The most common in ATLAS are PYTHIA [59] and HERWIG [60] which have only leading order matrix elements. PYTHIA and HERWIG are multi-purpose event generators designed to simulate all stages of a p-p collision and output the 4-vectors of all the particles at each stage of their evolution. HERWIG needs the addition of JIMMY [61] to model underlying event. Matrix Element generators such as ALPGEN [62] and MC@NLO [63] are run to generate the LO or NLO Matrix Elements of the hard process. These can then be interfaced with either PYTHIA or HERWIG and JIMMY for the shower and hadronization. MC@NLO with HERWIG will be used for all $t\bar{t}$ production discussed in this thesis.

5.1.1 Monte Carlo Truth

Most Monte Carlo generation samples include a truth particle container*. The truth particles are the particles as they are created in the generation stage. Although there will be truth information in the Monte Carlo events stating how each event was generated, a realistic analysis will not use truth information in the measurement because it will not be available with real data.

A truth container has all the particles that exist in each event in all their states of generation. Often one wants to know if the reconstructed object they are using originated from the generated particle implied by the reconstruction. In other words, if a reconstructed electron is found, it would be valuable to know if there was an electron that produced the detector activity which was reconstructed the electron.

For single particles the matching of the truth particle to that resulting from reconstruction is straightforward. One can then match this to the reconstructed object. For jets the situation is more complicated since there are many outgoing particles originating from a single quark or gluon. It is commonly resolved by choosing them in the form in which they are first produced. This means the truth quarks are defined to be the quarks which are initially produced, not any of the following states it forms before or during hadronization. These should have similar 4-vectors to the jet they create. It should be noted, however, that a photon or gluon can be produced at the same time if it is a three body decay.

The Truth Matched Jets are defined as the jets which are matched one to one with these truth particles. Since a jet's 4-vector is not, in general, the same as the truth particle which it came from, the word "matched" needs to be defined rigorously. A jet is matched to a particle if it is the closest jet within $\Delta R = 0.4$†. If two particles are matched to the same jet then the event is considered merged and not matched. This is

*In this case a TruthParticleContainer named SpclMC.

†$\Delta R \equiv \sqrt{\Delta\phi + \Delta\eta}$.

quite commonly the case for boosted W Bosons decaying hadronically. Truth matching efficiencies are generally above 90% for SUSY-like events.

In addition to these now defined Truth Matched Jets there are Truth Jets. These are jets formed from jet algorithms being run on the truth particles. They will have all the same variables as a reconstructed jet since the truth particle is used in the place of a calorimeter cluster. These can be built either before or after detector simulation. The difference is minimal for high energy jets but the simulation creates many particles which can be reconstructed as additional low energy jets.

5.2 Detector Simulation

Detector simulation is the process whereby the final particles of generated events are passed through a GEANT4 [64] simulation of the ATLAS detector to produce GEANT4 Hits. GEANT4 hits are a record of where each particle traversed the detector and how much energy was deposited. The path of the decay chain is followed through the simulated ATLAS detector. This must be done in discrete step sizes but these are chosen small enough so that only one material is contained within each step. This means that the particle will only interact at discrete points but enough so that a continuous approximation is achieved. The understanding of how each particle interacts with each type of material is calculated from empirically parameterized models and validated by precision beam tests. A hit is recorded for each step that occurred in a material that could detect and record the information related to this particle. For example, a neutrino will not be recorded in a calorimeter. Also, no particle will record a hit if the step is done in dead material such as the detector's supporting structure. However, the particle's path is still affected by the dead material.

5.2.1 Fast Simulation

The ATLFAST-II package was developed to improve the speed of the detector simulation with mandates to provide simulated information in such a way that the standard ATLAS reconstruction program can be run and the same output format as for fully simulated GEANT events can be provided. The gain in CPU time is accomplished by using parameterizations of the electromagnetic and hadronic calorimeter showers. Instead of a step by step calculation of the physics processes in particle showers, the energies are deposited into the ATLAS calorimeter structure based on these parameterizations [65].

Parameterizations for FastCaloSim are based on fully simulated single particle events. Only photons and pions from full simulation are used in the derivation of the parameters. Parameterizations are first made for how much energy is deposited in the calorimeter layers. After this an object dependent parameterizations is derived.

The speed gain has recently been accessed for $t\bar{t}$ events in Athena version 15. Eight identical jobs were sent to identical machines with no other jobs running on them. Five events per full simulation job were run while a hundred events for ATLFAST-II were run. The results are summarized in table 5.1 and show an overall gain factor of 15.8. Although the same reconstruction and AOD building is done the values differ due to initialization time.

Table 5.1: Comparison of the Full Chain production to that using ATLFAST-II for CPU time. An overall gain factor of 15.8 is achieved.

$t\bar{t}$ Sample	Sim. s/event	Digi. s/event	Reco. s/event	AOD Build s/event	Total (KSi2K) s/event
Full Sim	1023.6±25.1	19.5±0.2	74.7±0.9	12.9±0.1	3756.0±79.1
AF-II	34.6±0.2	8.8±0.0	26.7±0.2	1.4±0.0	238.0±1.0

It is important to assess to what extent the ATLFAST-II simulation can be used for physics analyses. In particular it is important to identify weaknesses in the detailed object description of ATLFAST-II and how they propagate to final analyses results. Differences between ATLFAST-II and full GEANT are expected because detector details and shower

fluctuations difficult to model accurately in a parameterization.

5.3 Digitization

Digitization is the process whereby the GEANT4 hits from the simulation are subjected to the response of the detector to produce digits, such as times and voltages. The hits produced from the simulation step are digitized in 25 ns bins and the effects from the detector and its electronics such as light attenuation and electronic noise are applied to resemble actual detector response. These are stored in the Raw Data Object (RDO) and sent as prepared raw data to the reconstruction. As can be seen in figure 5.1, RDOs contain the same information as the byte stream which comes from the detector, but they are not in the same format.

5.4 Reconstruction

The reconstruction stage combines the output of all the detectors to determine the important quantities and stores them as Event Summary Data (ESD). The ESD consists of sufficient information to re-run parts of the reconstruction, such as track refitting and jet calibration. For most analyses the information available in an ESD is excessive. The Analysis Object Data (AOD) is a summary of the reconstructed ESD. An AOD consists of a reduced size output of physics quantities from the reconstruction that should suffice for most kinds of analysis work. Separate tailor-made streams of AODs are foreseen for different needs of the physics community. These are called Derived Physics Data, DPDs. Both AODs and SUSY DPDs were used for the analyses in this thesis.

An important issue that must be dealt with in all analyses is overlap removal. The overlap refers to two objects being reconstructed from a single detector signature. The overlap for this analysis is with electrons, muons and jets. The objects will never be reconstructed at exactly the same position and there are also events were one would

expect these objects to be close to each other for topological reasons. A typical jet radius is $\Delta R = 0.4$ so overlap removal is only done on objects which are within this distance. Because of their individual structure, within $\Delta R = 0.2$ electrons are preferred before muons and jets. In the region $0.4 > \Delta R > 0.2$, jets are taken before electrons and muons because they are likely just part of the EM shower. This will be the only definition of overlap removal discussed in this thesis.

5.4.1 Jet Reconstruction

There are several ways to define and build jets so it is important to specify exactly which method was used. Clustering of calorimeter cells is the first step in defining a jet. The cell is the smallest calorimeter reconstruction object. All ATLAS calorimeters together provide 187652 cells; each of which provides the raw reconstructed energy in MeV. Clusters of calorimeter cells in the jet context are called particles and are the building blocks of jets. There are two types of particles commonly used in ATLAS reconstruction; towers and topological clusters. Particles have a massless four-vector built from the sum of cell energies and the geometrical center of the clusters. A tower is a group of cells in a fixed $\Delta\eta \times \Delta\phi$ grid over some or all samplings. A cluster is a group of cells formed around a seed cell. Clusters are the main reconstruction object for calorimetry and are used for all the jet reconstruction in this thesis. Topological clusters have variable borders based on the significance of the adjacent cells.

Jets built from towers are not used in this thesis because they have been shown to be problematic in early data. Towers have a fixed size of 0.1×0.1 in $\Delta\eta \times \Delta\phi$[‡], and all cells are used in towers. All the energy is in some particle and because of this they do not provide noise or pile-up suppression. The largest of these effects comes from cells which are well below threshold giving negative energies. Some methods have been attempted to suppress this noise [66] but were ultimately unsuccessful. Additionally, a small particle

[‡]0.1 for the $\Delta\phi$ is defined as $2\ \pi/64$.

shower on the edge of a tower will not be contained in one tower. Topological clusters on the other hand provide efficient noise and pile-up suppression on average. Topological clusters are more likely to not split energy deposits from a hadron, which gives validity to calling these objects "particles". The drawback of topological clusters is that they typically have detector region dependent size.

Jet finding algorithms are run on massless particles to build the jets. There are several methods for defining rigorously what a jet is. This ambiguity has caused the development of several different jet finding algorithms. As a standard, ATLAS uses a seeded Anti-k_T algorithm [67]. The Anti-k_T algorithm is of a type where for each particle above threshold, the quantities d_{ij} and d_{iB} are evaluated as follows:

$$d_{ij} = min(p_{Ti}^{-2}, p_{Tj}^{-2}) \frac{(\Delta R)_{ij}^2}{R^2} \ , \tag{5.1}$$

$$d_{iB} = p_{Ti}^{-2} \ . \tag{5.2}$$

To build Anti-k_T jets a list of d values is first compiled. If the smallest entry is d_{ij} the particles i and j are added and the list is remade. If the smallest entry is d_{iB}, this object is considered a complete jet and is removed from the list. Standard ATLAS Anti-k_T jets built from topological clusters are available with two size parameters, R, 0.4 and 0.6.

Energy Scale Calibration is important so that the energy of the jet accurately represents the energy of the coloured particle which initiated the jet. All cells are initially calibrated to EM scale. EM scale is a calibration such that the energy readout of the detector will give the energy of the EM particle which interacts with it. In other words, if a 100 GeV electron entered the calorimeter it would record 100 GeV. The detectors are calibrated with electron and pion particle beams. As discussed in the detector section, hadronic showers are different from EM showers so the calorimeter would not in general record the correct energy of the hadronic particle. If a shower is known to be hadronic a calibration must be applied in order to adjust the scale appropriately.

There are two hadronic scale calibration approaches in jet reconstruction. The Global Cell Weighting (GCW)[§] jet calibration uses topological clusters on EM scale as input to jet algorithms. A calibration function is then derived from Monte Carlo production. If it is possible to match a Truth Particle Jet with each reconstructed jet, then a fit to a cluster level calibration function based on energy density to all matched jet pairs can be derived.

The other method, Local Hadron Calibration, attempts to calibrate topological clusters to hadronic scale by discriminating EM and hadronic clusters. Although preferred, Local Hadronic Calibrated topological clusters are complicated to derive so this calibration scheme will likely not be used for early data.

5.4.2 Inner Detector Track Reconstruction

The helical trajectories of tracks are parameterized in the ATLAS software by the following five parameters: $\tau = (d_0, z_0, \phi_0, \theta, q/p)$, where d_0 is the transverse impact parameter, z_0 is the longitudinal impact parameter, ϕ_0 is the azimuthal angle of the track, θ is the polar angle and q/p relates to the curvature, λ, via $\lambda = q/psin\theta$. The track momentum resolution of is expected to be [32].

$$\sigma_{1/p_T} = 410/TeV(1 \oplus 80GeV/p_T) \ . \tag{5.3}$$

For this to be possible all subdetectors need to be functioning near their intended design capacity. A track from a particle traversing the barrel would typically have 3 pixel clusters, 8 SCT clusters and more than 30 TRT straw hits. Tracks in the inner detector can be seen in figure 5.3, which is a plot of the hit positions made with an early data run. The hits in the Pixel Detector are the innermost three layers, surrounded by the four layers of the SCT and finally the straws of the TRT.

Tracks are reconstructed in Athena using a number of individual algorithms which

[§]This method was formerly called H1 calibration.

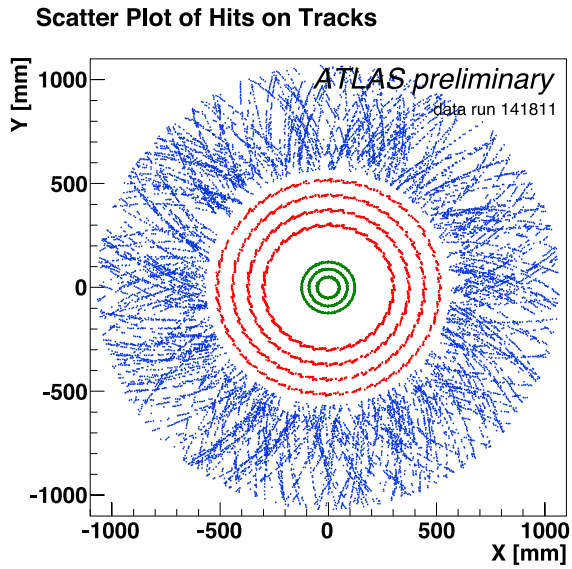

Figure 5.3: Scatter plot of hits on track in the Inner Detector barrel from an early set of collision events. [68]

are run sequentially on the inner detector hits [69]. The final track collection is the combination of the tracks reconstructed by each algorithm. Successive algorithms only run on the remaining hit collection to avoid duplicate tracks. The two basic types of algorithms are called inside-out and back-tracking. The inside-out algorithm reconstructs primary particles most efficiently, while the back-tracking algorithm is used to recover secondaries. Each algorithm can be run multiple times with different cut requirements to ensure that particles with different properties are reconstructed as efficiently at possible.

The inside-out algorithm reconstructs tracks starting from the pixel detector and adds hits while moving radially outwards. The clustered hits in the individual sub-detectors are grouped into space points. Space points are constructed from a single pixel cluster or two SCT clusters to provide a three dimensional information using the two dimensional position on a surface. Seeds are then built from groups of three space points in the silicon layers. Track candidates are built using a combinatorial Kalman filter technique where an ambiguity solver rejects poor track candidates until the hits are only attached to the most promising track candidates. The silicon track candidate is fit and an extension to the TRT is probed. Finally, a track fit is performed to provide the final estimate of the

track parameters.

Some tracks may not have seeds in the silicon detectors found by the inside-out algorithm. For example tracks originating from secondary decay vertexes inside the ID volume or from photon conversions may have insufficient silicon hits. Such tracks are reconstructed using the complementary back-tracking algorithms, which reconstructs tracks beginning from track segments reconstructed in the TRT. The track candidates are then extrapolated into the silicon and compatible ID clusters that have not been used in the inside-out algorithm are attached. The pixel and SCT clusters allow the polar track direction to be constrained.

5.4.3 Electron Reconstruction

A standard algorithm called "eGamma" [36] is used for the electron identification and reconstruction. An eGamma candidate electron is defined by a track matching to a selected cluster. The default clustering algorithm for ATLAS uses the sliding window technique. In this technique, first a fixed size window is chosen to take all cells within it. The window size is 3×7 second layer cells in the $\eta \times \phi$ plane for the barrel region of the EM calorimeter and 5×5 second layer cells in the endcap region. This window is then moved in each η and ϕ direction summing the energies of cells from all EM calorimeter layers and the presampler inside the window until a local maximum is found. If the cluster's E_T is greater than 3 GeV, the cluster is kept and the algorithm moves on to find other EM clusters.

If a track matches to a cluster it is then an electron candidate. The quality of Loose, Medium or Tight can then be assigned to it using the "isEM" bit quality cuts. These are Booleans which are defined in table 5.2. They are set to true or false dependent on p_T and η dependent parameterizations in their cut variables. These variables are based on the shower shape properties in different compartments of the calorimeter as well as variables combining ID and Calo information. The bits are grouped into three quality

classes; Loose, Medium and Tight. Loose is the combination of basic cluster quality variables (0, 2, 3, 4, 6). Medium is Loose with the addition of the cluster strip variables (8, 9, 10, 11, 12, 13, 15) and basic tracking parameters (17, 18, 19). Tight is Medium with the addition of some high quality tracking variables (16, 22, 24, 25).

Table 5.2: The isEM bits and their corresponding variables. Bits only available after relevant work in this thesis have been omitted.

bit	Name	Cut Variable Description
0	ClusterEtaRange	Cluster η range of the second EM layer
2	ClusterHadronicLeakage	Cluster leakage into the hadronic calorimeter
3	ClusterMiddleEnergy	Energy in 2^{nd} sampling of 7×7 cells
4	ClusterMiddleEratio37	Energy ratio in 2^{nd} sampling of 3×7 to 7×7
5	ClusterMiddleEratio33	Energy ratio in 2^{nd} sampling of 3×3 to 3×7
6	ClusterMiddleWidth	Energy weighted width in the 2^{nd} sampling
8	ClusterStripsEratio	Fraction of energy found in 1st sampling
9	ClusterStripsDeltaEmax2	Energy of 2^{nd} maximum in 1^{st} sampling
10	ClusterStripsDeltaE	Difference between 2^{nd} max. and 1^{st} min. in strips
11	ClusterStripsWtot	Energy weighted shower size in 1^{st} sampling
12	ClusterStripsFracm	Shower shape in shower core 1^{st} sampling
13	ClusterStripsWeta1c	Shower width weighted by distance from the max. one
15	ClusterStripsDEmaxs1	Difference between max and 2^{nd} max. in strips
16	TrackBlayer	Number of Pixel hits in the 1^{st} layer
17	TrackPixel	Number of Pixel hits
18	TrackSi	Number of Pixel and SCT hits
19	TrackA0	Transverse impact parameter
20	TrackMatchEta	$\lvert\eta_{cluster} - \eta_{track}\rvert$ in the 1^{st} sampling
21	TrackMatchPhi	$\lvert\phi_{cluster} - \phi_{track}\rvert$ in the 2^{nd} sampling
22	TrackMatchEoverP	Cluster energy divided by track momentum
24	TrackTRThits	Number of TRT hits
25	TrackTRTratio	Ratio of high to all TRT hits for isolated electrons
26	TrackTRTratio90	Ratio of high to all TRT hits for non-isolated electrons
27	TrackA0Tight	Distance of closet approach for tight selection
28	TrackMatchEtaTight	$\lvert\eta_{cluster} - \eta_{track}\rvert$ in the 1st sampling for tight selection
29	Isolation	Calorimetric and tracker isolation
30	ClusterIsolation	Calorimetric energy in ΔR <0.2
31	TrackIsolation	Summed track momentum in ΔR <0.2

Significant bias on electron resolution is introduced in the calorimeter crack region $1.37 < |\eta| < 1.52$. In this region the electron identification and measurement is degraded because of the large amount of material in front of the calorimeter and the crack between the barrel and extended barrel of the calorimeters [32]. Although electrons in this re-

gion may pass high quality selection they will be treated as poor quality because their resolution is poor.

There are two additional electron algorithms; a track-based algorithm and a forward cluster-based algorithm. These will not be used in this thesis and therefore will not be discussed further.

Electron reconstruction efficiencies were measure to be 94.3% for Medium with 4.2% relative uncertainty from data-driven methods. The electron performance in the EM calorimeters is quite good and leads to an electron energy scale known better to 1%. [70]

5.4.4 Muon Reconstruction

The muon reconstruction algorithms do not build one type of object as with the electrons. Instead of defining quality variables and cutting on them to determine quality, several different algorithms are defined. Each of these algorithms is independent of the others and has been optimized based on differing quantities. Some of these algorithms do essentially the same task as another and some are designed for specific purposes. There are four basic types of muons which could be said to be supplementary; Combined, StandAlone, Tagged and Calo muons. Six of the muon algorithms are grouped into two families of supplementary algorithms. Both of these families of 3 are essentially equivalent in performance so only one family will be discussed and used in this thesis.

The Staco muon reconstruction family contains the muons found by 3 different algorithms; STACO, Muonboy and MuTag. STAtistical COmbination (STACO) is an algorithm aimed to combine an ID track and MS track to produce a Combined muon. The algorithm works on two track containers, one for tracks reconstructed in the inner detector and one for tracks reconstructed in the muon spectrometer backtracked down to the z axis. First the tracks are filtered according to quality criteria. Then the algorithm forms pairs of ID and MS tracks. A crude matching in η and ϕ is required. The Combined muon comes from the combined track parameters obtained by a statistical averaging of

the ID and MS track parameters by means of their covariance matrices. This combination can be qualified according to a χ^2. A cut on the χ^2 could be applied at this point but would cause issues in overlap with the other algorithms in the family. For historical and debugging reasons, it is traditional to use a χ^2 cut which is so far into the tail that there are effectively no muons cut.

Since the ID has an acceptance limited at $|\eta| < 2.5$ and the muon system extends to $|\eta| = 2.7$, Combined muons cannot be formed in the $2.5 < |\eta| < 2.7$ region. Any MS track in this region must be considered a potential muon candidate. This is the purpose of the Muonboy algorithm. Muonboy starts from hit information in the muon spectrometer and produces standalone segments and tracks. Muonboy uses more complex muon tracks that are built by pattern recognition. These standalone tracks are extrapolated to the vertex to form StandAlone muons.

Due to the complex nature of the muon system, there are regions where there is a limited number of muon subdetectors. The most important of these regions is the $1> |\eta| >1.3$ region where there are a limited number of chambers in the transition region between horizontally laid and vertically laid chambers. Muon algorithms of the Tagged muon type are designed to account for the poor performance of the Combined algorithms in this region. The algorithm in the Staco family for this is MuTag. MuTag identifies muons by associating an inner detector track with Muonboy segments. Only ID tracks not combined in the STACO algorithm and segments not belonging to a STACO MS track already combined in the STACO algorithm are used for this identification.

By construction there is no overlap between the muons produced by the STACO and MuTag algorithms. The overlap between the STACO/MuTag muons and the Muonboy muons are removed during the AOD building when all muons in the containers are merged. This overlap is rare since it can only happen in the region $\eta \approx 2.5$.

As said before, it would take four algorithms to make a full supplementary set but only three are in each family. The fourth type of algorithm is the so called Calo muon. These

are designed to reconstruct muons in the region $\eta \approx 0$ where there are no muon detectors due to cabling. They use a track and an associated MIP calorimetric cluster recognizing algorithm. In some sense they have similar reconstruction to that of an electron but with very different clustering.

The term "Crack muons" is defined to be either StandAlone, Tagged or Calo muons defined in specific regions. StandAlone muons must only be taken if outside $|\eta|$=2.5. Tagged muons must only be taken if they are in the region 1< $|\eta|$ <1.3 and Calo muons are required to be in $|\eta|$ <0.1.

The ATLAS muons reconstruction was designed to have

$$\frac{\sigma_E}{E} = 10\% \tag{5.4}$$

for 1 TeV muons [36]. Figure 5.4 shows the di-muon invariant mass spectrum for data, from Combined opposite sign muons. The muon Event Filter trigger applies a pT threshold at $\approx$ 15GeV, which for consistency is reconfirmed offline for one of the two inner detector-muon spectrometer combined tracks.

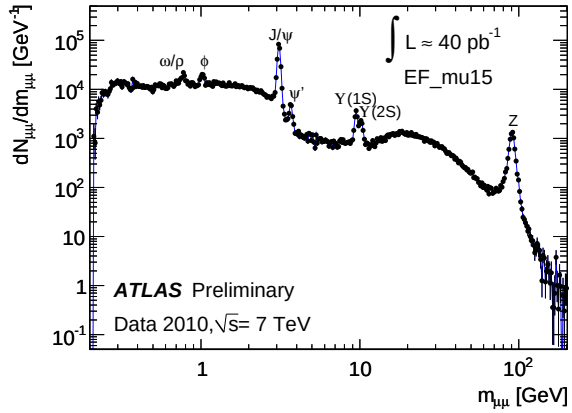

Figure 5.4: The invariant mass distribution of two oppositely signed Combined muons for data corresponding to an integrated luminosity of about 40 pb^{-1}. [71]

Inner Detector muon track reconstruction efficiency is greater than 99% [72]. Combined muon reconstruction efficiency 92.4% with 2.5% relative uncertainty from data driven methods [73]. The momentum scale of combined muons is known to better than

1% and resolution known better than 5% [72].

5.4.5 Missing Transverse Energy Reconstruction

Because particles like neutrinos and neutralinos only weakly interact with matter no detector system is built to detect them. Instead some information is inferred about the weakly interacting particles from the sum of the detected particles. Reconstructed energy should be balanced in the transverse direction unless the event contained weakly interacting particles. A significant discrepancy from a balancing sum should imply that a weakly interacting particle was present in the event. The quantity required to balance this sum is called Missing Transverse Energy,

$$\not{E}_T = \sqrt{\not{E}_x^2 + \not{E}_y^2}\,, \tag{5.5}$$

where $\not{E}_x^2$ and $\not{E}_y^2$ are the sum of cell energies in the $\hat{x}$ and $\hat{y}$ directions, respectively.

A cell-based algorithm which uses the energy deposits in each of the calorimeter cells is default for ATLAS. A correction is applied for the energy lost in the cryostat and an additional term is added for the muon energy. Clusters associated to electrons and jets used the corresponding calibration of those objects for the clusters.

The minimal definition of $\not{E}_T$ is to use calorimeter clusters on the uncalibrated EM energy scale. This algorithm is stable for early data taking, since it does not rely on the accurate reconstruction of physics objects. This will therefore be the definition used for the data analysis.

Additional corrections can be made by using cells once they have been calibrated. The cells calibrated with global weights depending on their energy density will be used for the preliminary MC studies. Only the cells that remain after a noise suppression procedure are used.

Chapter 6

Event Cleaning

There are several sources of fake objects in a detector environment. A fake object is a reconstruction object (a jet for example) which was not formed from a corresponding particle in the hard event. As previously mentioned when discussing overlap removal a particle can be reconstructed as an alternate object. For example, an electron can be reconstructed as a jet and is therefore a fake jet.

This chapter deals with fakes which do not come from the hard process at all. The two dominant sources of this are cosmic muons and detector noise. These are important because they can create a signature with fake $\not{E}_T$ or jets.

6.1 Detector Noise

All calorimetric energy above a threshold will create a jet. Since detectors are not perfect some detector effects can mimic energy above threshold and therefore fake a jet. Most of these jets come from coherent detector noise. All detectors have some intrinsic noise which is distributed throughout the detector. If a few calorimeter cells in a close region all have fluctuations above threshold this will be reconstructed as a jet. Clearly one would like to ignore such jets in an analysis but it is not clear exactly how to distinguish them from real jets. One then defines "bad jets" as jets reconstructed with properties that are

strongly correlated with the signatures of these detector effects. There are several such properties and a short review will be given here.

Some cells are known to be relatively noisy most of the time and can then be ignored when reconstruction is done. Detecting components are not the only source of this noise. For example, corrosion problems affecting the preamplifier chips result in sporadically noisy preamplifiers. Such cabling and electronics issues can be very problematic as one component typically represents a number of cells.

Dead and noisy cells are removed from reconstruction and are then corrected for in a parameterized way. Jets which receive large corrections from this parameterization are likely to be mismeasured. The variable fCor is the energy fraction in dead cells and can be used in the definition of bad jets.

Since it is known when the bunches cross, it can be estimated when there will be detector activity associated with a hard interaction. Bad jets are not associated to in-time real energy deposits in the calorimeters. This means that they can be reduced based by only using cells with appropriate timing.

Detector noise is typically of low p_T since it is related to fluctuations and therefore this noise reconstructs low p_T jets. SUSY searches generally only look at jets with relatively high momentum and ATLAS jets are always required to have $p_T > 7$ GeV. There can still be very high energy fake jets coming from detector effects. Also, a number of low p_T fake jets can serve to significantly bias the $\not{E}_T$.

The number of clusters or cells which form a bad jet should be smaller on average than real jets. This motivates using the number of clusters or cells to define bad jets. A more sophisticated variable for this is the so called n90 variable, which is the minimum number of cells required to contain at least 90% of the jet energy.

Being small in size also means that they are more likely to be located in one calorimeter or calorimeter region. A typical jet will pass through both the EM and hadronic calorimeter. Since this is not the case for a bad jet, the quantity EMfrac has been de-

fined. It is the fraction of energy in the EM calorimeter relative to the whole uncalibrated calorimeter. Similarly the variable HECfrac can be defined as the energy fraction in the Hadronic End Cap. Another such variable is fmax which is the maximum energy fraction in one calorimeter layer of any calorimeter.

The jet quality variable, Q, is another very powerful quantity. It is the fraction of LAr cells with a cell Q-factor greater than a cut off. The cell Q-factor measures the difference between the measured pulse shape, a_i^{meas}, and the predicted pulse shape, a_i^{pred}, that is used to reconstruct the cell energy. It is computed as,

$$Q_{cell} = \sum_{samples} (a_i^{meas} - a_i^{pred})^2. \tag{6.1}$$

All of these variable can be combined and optimized to define bad jets and therefore reduce the effect of fake jets.

6.2 Cosmic Muons

Cosmic rays are energetic cosmological particles which come into the Earth's atmosphere. The vast majority of all the incoming cosmic ray particles are protons. These strongly interact with the nuclei of atmospheric gases resulting in the production of unstable mesons. Many of these quickly decay into muons which can be of high energy because the originating proton can be. These muons will interact with the ATLAS detector just as would muons from collisions. This is the main reason that the LHC facility is 100m underground. The earth acts as a very good shield for the cosmic muons to interact with and stop before reaching the ATLAS detectors.

Despite the depth underground it is expected that TeV cosmic muons will hit the detector at a rate of 6×10^{-4} Hz, which translates to about 2 per hour. Cosmic muons will come at random times relative to detector timing so one expects only coincidental overlap with events.

Cosmic muons can interact with the detector in two ways to be reconstructed as fake objects. The obvious one is to be reconstructed as a muon. Additionally, a cosmic muon can have hard bremsstrahlung in the calorimeter which can fake a jet since it will deposit energy. It is even possible for multiple jets to be produced by showers outside the calorimeter. Both of these will affect $\not\!\!E_T$ because there will be a reconstructed object that did not come from the balanced hard interaction.

6.2.1 Cosmic Muon Removal

The ATLAS detector was functioning well before the LHC was ready to supply colliding beams. This allowed for time to analyze the cosmic background in the absence of beam. With the ATLAS detector on-line one could record many cosmic muon events to study their properties. The study here corresponds to a 16 hour long time period with a trigger set to fire on Cosmic Muons and Calorimetric activity*.

Muons which cause hits and segments in the muon system are not often reconstructed by a muon algorithm. This is mainly due to the fact that it is very rare for a muon to travel exactly through the center of the detector. Since muon algorithms will not reconstruct a muon which does not point at the expected interaction point, a cosmic muon must pass near this point to fake a muon. This motivates the cut to removed muons which are not associated to the vertex by a constraint on $|z_0 - z_{Vertex}|$. If a muon does pass through the detector one should reconstruct two muons since this is the same cosmic muon found going in and out. It is very unlikely that both will be reconstructed as Combined muons. Figure 6.1 shows the ϕ between the Combined muon and the farthest additional Staco family candidate muon. The muons were selected with $p_T > 20$ GeV, $|\eta| < 2.7$ and less than 10 GeV of calorimetric energy within $\Delta R = 0.2$. From comparing the SU4 SUSY point and $t\bar{t}$ MC to cosmic events it can be seen that cosmic muons are much more likely to be back to back in ϕ.

*More specifically the triggers were RNDM, CosmicMuons and L1Calo.

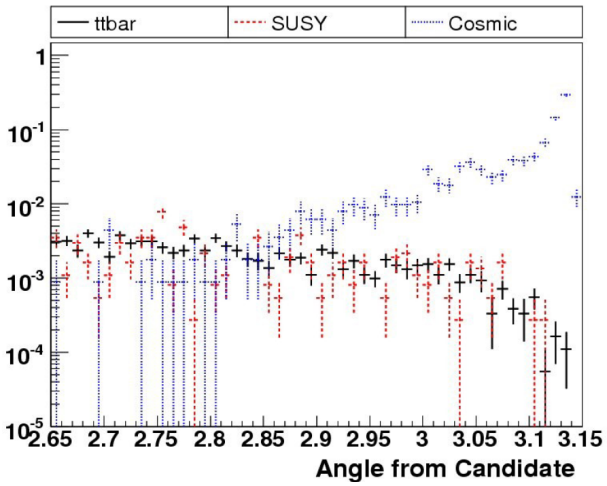

Figure 6.1: The ϕ between the Combined muon and the farthest additional Staco family candidate muon. All distributions are normalized to unity.

One could use this as a cut variable to reduce cosmic background in events where two muons were identified. If one were to cut at $\phi = 3$, then $(77.1 \pm 2.8)\%$ of the Combined muons would be correctly flagged as Cosmics. This also flags $(0.15 \pm 1.65)\%$ of the SUSY and $(0.13 \pm 0.64)\%$ of the $t\bar{t}$ Combined muons. This is likely to be mostly from events where there were two true hard muons in the event.

To reduce fake jets from cosmics one can use variables from section 6.1. As this work was done concurrently to the detector noise studies, not all variables were known or available. In addition to these, one can use the number of tracks in a jet. Tracks are defined with $p_T > 1$ GeV, $|d_0| < 100$ μm, $|z_0 - z_{vtx}| < 150$ μm, 1 B-layer hit, 2 pixel hits, 7 pixel plus SCT hits for this study. Most jets coming from a collision have tracks in them; 98.21% for $t\bar{t}$ and 97.72% for SUSY with negligible error. Jets from cosmics will only have a track by coincidence, although, this is likely to be worse when overlaid with collisions. Only $(0.48 \pm 0.17)\%$ of cosmic jets have a track inside $\Delta R = 0.4$. This implies one could only make cuts in the tracking region ($|\eta|$ <2.5), which is shown to contain most of these jets in figure 6.2. Jets from cosmics are more likely to be at low $|\eta|$ because that way they had to transverse less earth to reach the detector. Also, one would not like to make this requirement on a jet on the edge of the tracking region since half of it would then not have the possibility to contain tracks.

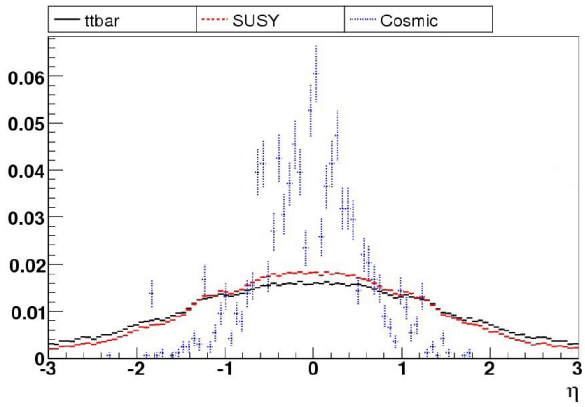

Figure 6.2: The η of jets for $t\bar{t}$, SUSY and cosmic events. It can be seen that jets from cosmics are much more central.

Since jets from cosmics are muon showers they should be smaller than real jets. The number of clusters represents the size of a jet. Cosmic muon showers should be localized in the detector so they will likely shower in either the EM or hadronic calorimeter. It is much more likely for them to shower in the Hadronic calorimeter since it is significantly larger. This implies that the EMfrac is a useful variable to cut on as well. Figure 6.3 shows the distributions for the number of clusters and EMfrac.

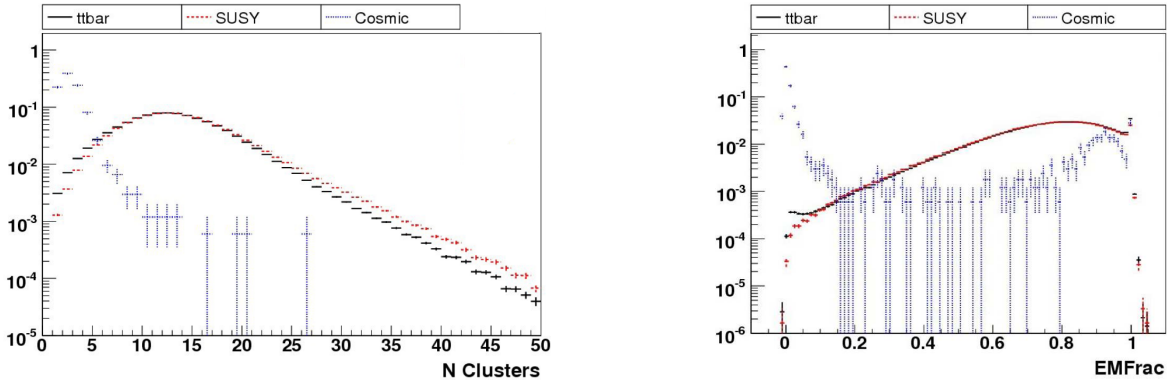

Figure 6.3: The distributions for the number of clusters (left) and EMfrac (right). All distributions are normalized to unity.

A cut based on these quantities was designed for jets with no tracks, $p_T > 20$ GeV and $\eta < 2.4$. Since the number of clusters and EMfrac are somewhat correlated the cut was based on the plane of these two variables. The cut was chosen to remove an event if it contained a trackless jet with the above criteria which had less than 7 Clusters and an EMfrac < 0.2 or had less than 2 clusters. This cut, in addition to the track requirement,

will flag $(91.9 \pm 2.13)\%$ of the jets from cosmics correctly. Only 0.18% of SUSY jets and 0.29% of $t\bar{t}$ jets are flagged as cosmics. If an event is cut when it has a jet flagged as a cosmic it has very little effect on an analysis. Since SUSY events have many jets the maximum effect this will have can be calculated by multiplying the average number of jets by 0.18%. This has a similar effect on the dominant backgrounds so the loss in significance is small.

It should be noted that no cut on high EMfrac is suggested. This can be motivated because radiative mechanisms of energy loss for muons become important at lower energies in the LAr calorimeter than in the Hadronic Tile Calorimeter. However, cutting on high EMfrac is ill advised because it cuts electrons without tracks. This can be related to overlap removal and will be demonstrated in section 7.3 that such an event is of poor quality. Preliminary investigations were done using a calibrated EMfrac to separate electrons. The hadronic energy is changed quite drastically when the jets are calibrated. This will shift the EMfrac distribution away from the high region for jets.

6.3 Cleaning Cuts Used for Data

The combination of several cosmic muon and detector noise studies was used to define an official ATLAS set of cleaning cuts for data events. The following will be used in the final analysis of this thesis.

All good events must have the good objects coming from a good primary vertex. A good primary vertex is defined as one with more than 4 tracks.

Good Jets are defined as Anti-k_T jets with R=0.4 built from Topological clusters. The jets are calibrated purely by adjusting for the Hadronic energy scale[†] from EM to the hadronic scale. The topological jet cuts are $p_T > 30$ GeV and $|\eta| < 2.5$.

Bad Jets are defined to be Good Jets which satisfy any of the following criteria:

[†]Internally this is referred to as EMJES.

1. EMFrac > 0.95 and Q > 0.8
2. n90 ≤ 5 and HECfrac > 0.8
3. $|Q| > 0.5$ and HECfrac > 0.5
4. It is out of time by more than 25 ns
5. EMFrac < 0.05
6. Fmax > 0.99 and $|\eta| < 2$

Chapter 7

Single Lepton SUSY Analyses

SUSY search methods have been standardized for some time in the ATLAS collaboration [28] [36]. SUSY searches are traditionally separated into final states according to the number of leptons and jets. The single electron or muon channels are discussed in this thesis.

Preliminary searches can be highly dependent on the Monte Carlo used. This issue is compounded when ATLFAST-II is used because it is expected to be farther from an exact model than the full simulation. One must ensure that MC does not add an unknown bias to results.

There are many subtle details for the selection of electrons and muons. The reconstruction algorithms are quite advanced but optimizations can be made for specific searches.

7.1 Overview of the 1 Lepton and 4 Jets Analysis

As mentioned above, the set of cuts which are useful for each channel have been studied for some time. This section will motivate and outline the cuts for a 1 lepton and 4 jets analysis. For convenience, the values given will correspond to the first study which will be discussed in this thesis. Following previous analyses the 4 Jet, 1 lepton channel is

defined with the following cuts:

1. One ℓ with $p_T > 15$ GeV and no additional ℓ with $p_T > 10$ GeV
2. At least 4 jets with $p_T > 40$ GeV within $|\eta| < 3$
3. Leading jet $p_T > 80$ GeV
4. $\not{E}_T > 80$ GeV
5. Transverse mass: $m_T > 100$ GeV
6. Effective mass: $\mathrm{M_{eff}} > 700$ GeV
7. Transverse sphericity: $S_T > 0.2$
8. $\not{E}_T > 0.2 \cdot \mathrm{M_{eff}}$.

The order of cuts and their values are not fixed since this is merely given as a template and of course the order will not influence results. The first two cuts define the channel. As usual the symbol ℓ refers to muons and electrons. As a standard the Medium isEM and the Combined muon requirements are applied for the electron and muon identification, respectively. Events with electrons in the calorimeter crack region ($1.37 < |\eta| < 1.52$) are removed due to the expected degradation of their measured quantities.

For both lepton flavours the isolation variable ETCONE20 is used to select prompt leptons. ETCONE20 is defined as the calorimetric energy in a cone of $\Delta R < 0.2$ around the lepton. For this cutflow ETCONE20 is required to be smaller than 5 GeV + $0.2 \cdot p_T$.

The second cut requires GCW calibrated Anti-k_T jets with specific p_T and η cuts. Such jets are referred to as preselected jets, although such a high p_T cut is atypical. Bad Jet cleaning cuts are often applied to define preselected jets as well as to veto events. Bad Jet variables were not well understood at the time of the following analysis so were not used until subsequent analyses.

The third cut, on the values of the jet p_Ts, as well as the fourth, on the $\not{E}_T$, represent the aforementioned SUSY phenomenology. For the SUSY models which are relevant in this thesis, several hard jets and large $\not{E}_T$ is expected. The cut values are optimized for significance over background, although, this is model, beam energy and luminosity

dependent. The leading jet p_T and the $\not{E}_T$ distributions showing the SU4 point compared to the dominant $t\bar{t}$ background can be seen in figure 7.1.

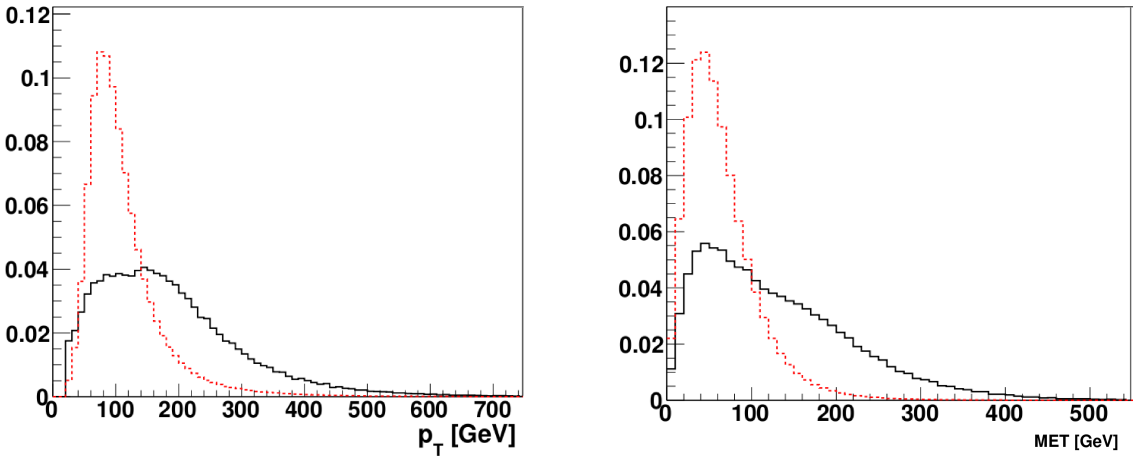

Figure 7.1: Comparison plots for the SU4 point (black) and $t\bar{t}$ (red) for the leading jet p_T (left) and the $\not{E}_T$ (right) distributions. The ATLFAST-II samples from the following study were used here for illustrative purposes. The distribution's integrals are normalized to unity.

The fifth cut is a requirement on the so called transverse mass which is defined as:

$$m_T = \sqrt{(\not{E}_T + p_T^\ell)^2 - (\not{E}_x + p_x^\ell)^2 - (\not{E}_y + p_y^\ell)^2} \ . \tag{7.1}$$

The purpose of the m_T cut is to reduce the Semileptonic $t\bar{t}$ and W+Jets backgrounds. In these events nearly all of the $\not{E}_T$ comes from the neutrino. This means that one could reconstruct the mass of the W Boson in the transverse direction using the $\not{E}_T$ in place of the neutrino. As seen in figure 7.2 there is a maximum at the W mass. SUSY, on the other hand, should have not such a property since the $\not{E}_T$ comes from at least two LSPs.

The effective mass is the 6^{th} cut and is defined as follows:

$$M_{\text{eff}} = \not{E}_T + \sum_0^4 p_T^J + p_T^\ell \ . \tag{7.2}$$

It represents the momentum sum of all the hard objects in the transverse direction. This should be strongly correlated with the energy scale of the process. Since SUSY particles

are heavy their M_{eff} should be high relative to SM events. Note that the convention is to take the sum over only the hardest* four jets while it is possible to have more than four jets in the event. In ATLAS, this is the general case for SUSY searches which require a fixed number of jets but need not be done in general. M_{eff} distributions showing the SU4 point compared to the dominant $t\bar{t}$ background can be seen in figure 7.2. The structure in the distribution is a result of the differing production and decay channels that are combined to make the SU4 sample.

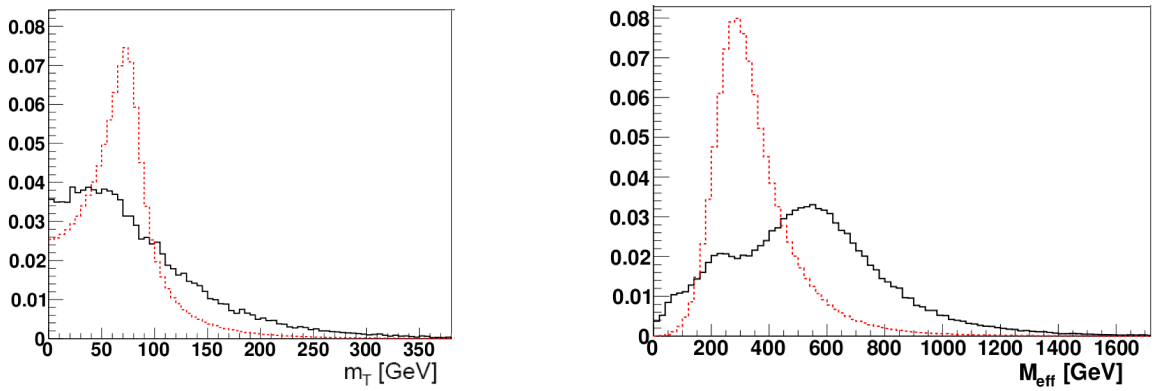

Figure 7.2: Comparison plots for the SU4 point (black) and $t\bar{t}$ (red) for the m_T and (left) and the M_{eff} (right) distributions. The ATLFAST-II samples from the following study were used here for illustrative purposes. The distribution's integrals are normalized to unity.

The seventh cut is the transverse sphericity which is defined as:

$$S_T = \frac{2\lambda_2}{\lambda_1 + \lambda_2} \tag{7.3}$$

where λ_1 and λ_2 are the eigenvalues of the sphericity tensor $S_{ij} = \sum_k p_{ki} p^{kj}$ for the sum over all preselected objects. SUSY events tend to be relatively spherical ($S_T \approx 1$) since the initial heavy particles are usually produced approximately at rest in the detector and their cascade decays emit particles in all directions. QCD events are dominated by back-to-back di-jet configurations ($S_T \approx 0$) so this is an effective variable for reducing QCD background. $t\bar{t}$ pairs on the other hand are often also produced nearly at rest. Since this

*Hardest refers to the highest in p_T.

is the dominant background this cut has limited discriminatory power.

The final cut is motivated by the fact that a lot of energy is carried away by the LSPs. This means that the fraction of total energy in the event which is contained in the $\not{E}_T$ should be large. This is also the case for events with neutrinos coming from a W decay. Since this is the case for both of the largest backgrounds this cut has relatively limited effectiveness.

7.2 ATLFAST-II Validation

Because it is unknown which (if any) model of SUSY will be found, several differing models must be tested. This means that MC must be generated in a wide variety of models and parameter spaces. This is often accomplished by making grids in parameter spaces of highly constrained models such as mSUGRA. To generate a large number of samples, the fast simulation of ATLFAST-II is useful. If one would like to use this in place of fully simulated MC its quality must be ensured.

A detailed comparison of the ATLFAST-II simulation to full simulation was performed for both individual particle signatures as well as for selected physics benchmark processes [74]. Since only the calorimeter has a fast simulation, the full GEANT simulation is used for all tracking systems up to the surface of the calorimeter. This means that the ATLFAST-II tracks are simulated using GEANT whereas the energy depositions in the calorimeters are based on the fast shower parameterization. Muons are tracked through the full detector using the GEANT simulation; i.e. inner detector, calorimeters and muon system use GEANT for muons in ATLFAST-II.

The full simulation data sets were simulated with Athena release 14.2.10.1 and reconstructed with release 14.2.25.8. The latter release was used for both simulation and reconstruction of the ATLFAST-II samples. All of the samples were produced at 10 TeV center of mass energy.

The parameterization of the fast calorimeter simulation was derived in ATHENA release 10. On the electromagnetic energy scale, it shows differences of 5-10% with respect to the full simulation. These differences were taken into account in the object calibration. Thus for electrons, photons and jets special calibration weights were determined for ATLFAST-II. Specific GCW calibration weights were fitted on di-jet samples in ATHENA release 13.0.40, using the same code to obtain the energy calibration as for full simulation. This specific calibration was also used in the calculation of the $\not\!\!E_T$.

Since the fast calorimeter simulation itself did not change between ATHENA releases 13 and 14, no new calibration weights were determined for release 14. However, due to the changes in the inner detector material the calibration was no longer optimal, in particular the response to low energy calorimeter clusters were affected.

This ATLFAST-II version provided an excellent reproduction of jets relative to the full simulation. Minor deviations in Jet Energy Scale (JES) are seen and are reviewed in the note [74]. Deviations are visible if detailed shower-sensitive identification variables are compared. The electron energy resolution is smaller because many of these variables were modelled with overly optimistic assumptions about the shower and calorimeter resolution. Since such variables are used in the reconstruction of electrons and photons, ATLFAST-II significantly over estimates their reconstruction efficiency, especially in the low p_T region. For these cases deviations in the identification efficiencies at the level of 2-5% appear. The majority of these effects can be reduced with additional corrections applied to ATLFAST-II as seen in figure 7.3.

The most problematic issue with regards to electron modelling is the inability to reproduce the rate of fake electrons. The number of fake electrons with $p_T > 5$ GeV in $t\bar{t}$ events normalized to the total number of events passing the Loose, Medium or Tight isEM selections in the $t\bar{t}$ sample are shown in Table 7.1.

Muons do not suffer from many of the issues affecting electrons and photons because the full simulation is used in ATLFAST-II. However, it must be noted that secondary

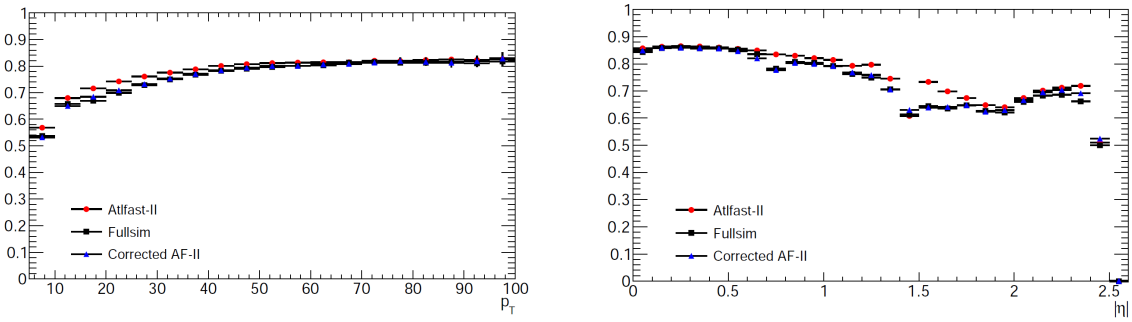

Figure 7.3: The electron p_T and η distribution for the comparison of ATLFAST-II to full simulation. Better agreement is seen with additional corrections. [74]

Table 7.1: Comparison of Electron fake rate between ATLFAST-II and GEANT.

	Full Simulation	ATLFAST-II
Loose electrons	30.8%	28.0%
Medium electrons	1.47%	0.37%
Tight electrons	0.15%	0.02%

muons that are produced in the development of hadronic showers in the calorimeter are not included in the ATLFAST-II simulation. Additionally, the shower parameterization only reproduces the energy depositions inside the calorimeter. This implies that no punch-through[†] particles are included in the ATLFAST-II simulation. Both effects contribute to an underestimation of the occupancy in the muon chambers and of the rate of reconstructed fake muons.

7.2.1 ATLFAST-II for SUSY

Since this thesis deals with SUSY it is important to understand how these discrepancies propagate to SUSY analyses. The SUSY selection described in the beginning of this chapter will be considered here. The SUSY model chosen for signal is the so called benchmark point SU4 mentioned previously. The SU4 mass spectrum and branching ratios were calculated using ISAJET [75] version 7.75 and it was generated with the HERWIG++ generator [76] version 2.4.2 using the MRST2007 LO* parton distribution

[†]Punch-through is when jets exit the calorimeters to provide hits in the muon system.

functions [77]. The inclusive SUSY production cross section was calculated by Prospino [78] at next-to-leading order.

MC@NLO v3.41 [63] with PDF set CTEQ66 [79] was used for the generation of $t\bar{t}$ events. The $t\bar{t}$ sample generated is a so called Leptonic $t\bar{t}$ sample meaning that there are no fully hadronic decays.

Comparison plots for the signal and dominant backgrounds were made for the analysis defined in section 7.1. The SUSY distributions for the p_T of the leading jet, the $\not{E}_T$, the M_{eff} and the S_T are shown in figure 7.4 before the respective cuts are applied. The distributions do not show significant discrepancies. However, the jet p_T spectrum and the $\not{E}_T$ show discrepancies for low values.

The expected event numbers for the signal and for the dominant $t\bar{t}$ background are summarized in Table 7.2 after each selection cut. The numbers are normalized to an integrated luminosity of 1 fb^{-1} and are given for full simulation as well as for ATLFAST-II. There is quite good agreement but some discrepancies are clear. The discrepancies found in the SUSY analysis were all consistent with what was seen for the individual objects analyses discussed in the above. Comparisons were also made for the second most dominant background, W+Jets. No new phenomena were seen with these samples. Additionally, due to the rejection efficiency of the cuts very few events passed to later cut stages and thus no conclusion can be made.

The largest source of discrepancies was the out of date parameterization of the calorimeter. As discussed above, the calorimeter parameterization and jet calibration were calculated in ATHENA release 10 and 13 respectively. It is expected that a reparameterization could significantly reduce these effects [80]. The other clear issue is with the muon fake rate. This is a well understood implementation issue and several possibilities to solve this issue are being explored. For example, a parameterization of the fake muon rate from jets could be made to compensate for this discrepancy.

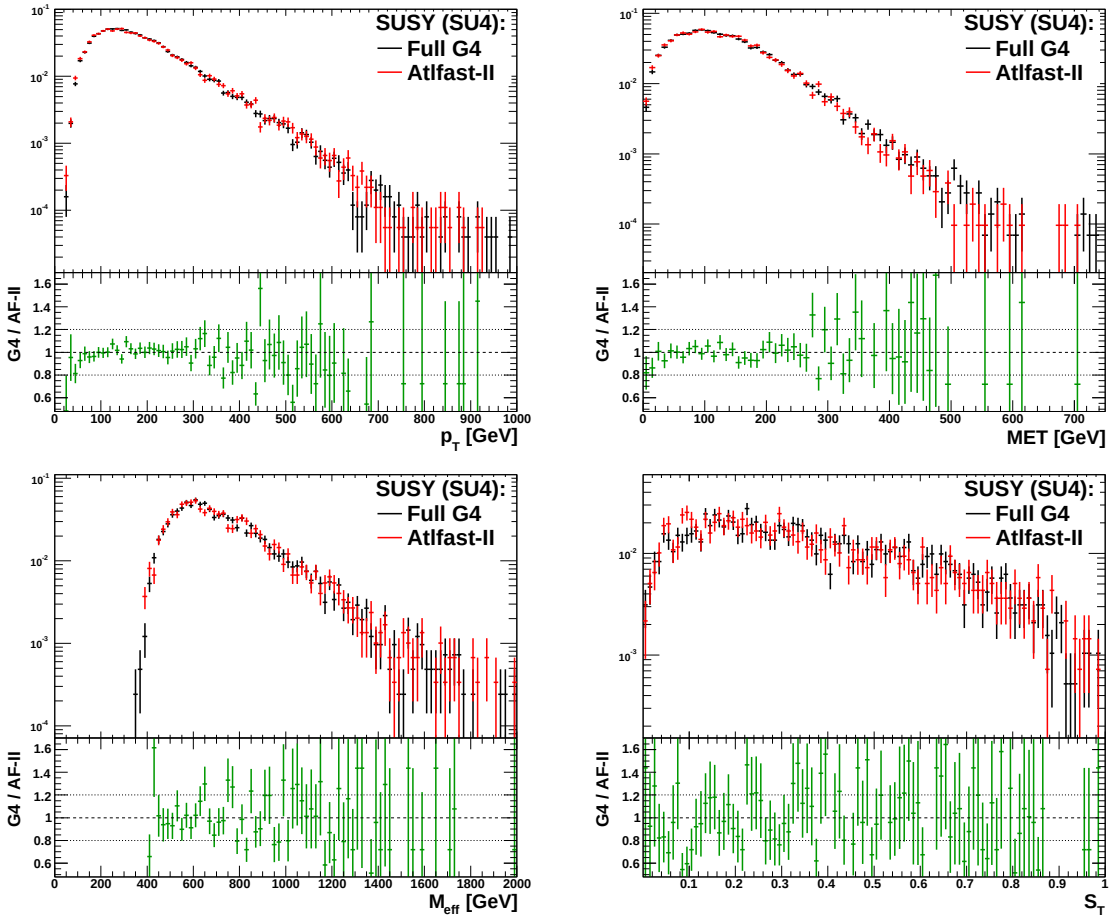

Figure 7.4: The distributions of the p_T of the leading jet (after cut2), the $\not{E}_T$ (after cut 3), the M_{eff} (after cut 5) and the S_T (after cut 6) for SUSY signal events. The results obtained from full simulation (black) and ATLFAST-II (red) are superimposed.

With the corrections to the electrons applied ATLFAST-II simulation constitutes a reliable simulation for SUSY analyses. Care must be taken in analyses where fake electrons or muons from QCD jet production are important. Following the study done here several changes were made in an attempt to account for the issues found. A repetition of this work after these updates will likely show significantly improved results.

Table 7.2: Expected numbers of SUSY signal and background events from $t\bar{t}$ production normalized to 1 fb^{-1} for full simulation and ATLFAST-II. The relative efficiencies of the various selection criteria are given in addition. The quoted errors result from the available Monte Carlo statistics.

SUSY signal	Full Simulation		ATLFAST-II	
	# events	ϵ (%)	# events	ϵ (%)
Lepton (ID and p_T)	23,409 ± 122	21.8	23,581 ± 145	21.9
4 Jets, $p_T > 40$ GeV	16,889 ±104	72.1	17,200 ± 124	72.9
$p_T^1 > 80$ GeV	9679 ± 76	57.3	9799 ± 93.7	57.0
$\not{E}_T > 80$ GeV	7055 ± 67	72.9	7074 ± 80	72.2
$m_T > 100$ GeV	2604 ± 41	39.4	2806 ± 50	39.7
$M_{\text{eff}} > 700$ GeV	1281± 28	46.1	1295 ± 34	46.2
$S_T > 0.2$	891± 24	69.5	866 ± 28	66.9
$\not{E}_T > 0.2 \cdot M_{\text{eff}}$	615 ± 20	69.1	578 ± 23	66.8
Leptonic $t\bar{t}$	Full Simulation		ATLFAST-II	
	# events	ϵ (%)	# events	ϵ (%)
Lepton (ID and p_T)	105,749 ± 125	48.7	106,907 ± 79	49.3
4 Jets, $p_T > 40$ GeV	69,875 ± 102	66.1	71,653 ± 65	67.0
$p_T^1 > 80$ GeV	20,498 ± 55	29.3	20,755 ± 35	29.0
$\not{E}_T > 80$ GeV	5945 ± 30	29.0	5743 ± 18	27.7
$m_T > 100$ GeV	550.7 ± 9.0	9.3	533.6 ± 5.6	9.3
$M_{\text{eff}} > 700$ GeV	166.4 ± 5.0	30.2	161.3 ± 3.1	30.2
$S_T > 0.2$	89.9 ± 3.6	54.0	87.4 ± 2.3	54.19
$\not{E}_T > 0.2 \cdot M_{\text{eff}}$	33.4 ± 2.2	37.2	32.8 ± 1.4	37.5

7.3 Lepton Definition Optimization

In order to increase signal efficiency a correct understanding of the event is necessary. This is important, not only for selecting the signal, but for removing the background. This means that one would like to reconstruct all of the primary partons with low resolution through a selection which has a low fake rate. Of course this is never possible but improvement can always be attempted towards this goal. This analysis deals with optimization of the selection of reconstructed leptons. For the first studies the event cuts were taken as:

1. One isolated ℓ with $p_T > 15$ GeV and no additional ℓ with $p_T > 10$ GeV
2. At least 4 jets with $p_T > 20$ GeV within $|\eta| < 3$

3. Leading jet $p_T > 100$ GeV with the following 3 having $p_T > 50$ GeV
4. $\not{E}_T > 100$ GeV
5. Transverse mass: $\mathrm{m}_T > 120$ GeV
6. Transverse sphericity: $S_T > 0.2$
7. Effective mass: $\mathrm{M}_{\mathrm{eff}} > 700$ GeV
8. $\not{E}_T > 0.2 \cdot \mathrm{M}_{\mathrm{eff}}$

The first cut can be interpreted as two lepton definitions for both the e and μ. One to select what will be used as a lepton and one to remove events if an additional object of that type is found. The former will be referred to as the "good lepton" and the latter will be referred to as the "secondary veto lepton".

Only hadronically decaying taus are referred to as taus in this context. The leptonically decaying taus are considered as their decay particle in the generation. For example a tau which decays to an electron is considered an electron. Changing our definition for this discussion, the symbol ℓ is used to refer to electrons, muons and leptonic taus whereas the word "lepton" refers to all charged leptons. When speaking of truth, the terms electron and muon will additionally refer to the corresponding leptonic tau decays. Hadronic taus will most likely be reconstructed as a jet and therefore will be treated as such.

The m_T cut is intended to reduce the Semileptonic $t\bar{t}$ background. 87% of the $t\bar{t}$ background in the above cutflow is Semileptonic before the m_T cut. As can be seen from figure 7.5 this is a very powerful cut to reduce $t\bar{t}$ background. The separation power is increased for SUSY points higher in m_0 and $m_{\frac{1}{2}}$. Additionally most of the high m_T "tail" is composed of Di-leptonic $t\bar{t}$ events.

The purpose of the secondary veto lepton is to reduce Di-leptonic $t\bar{t}$ background. In the standard ATLAS analysis [36] secondary veto leptons only differ from good leptons by the p_T cut. It is quite possible to reconstruct leptons to p_T lower than 15 GeV but lowering the p_T of the lepton will increase the fake rate as well as the acceptance.

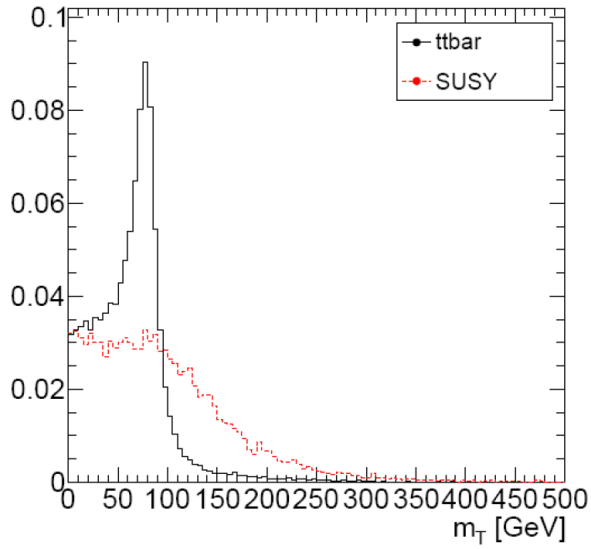

Figure 7.5: The m_T distribution before the cut is applied with distributions normalized to unity.

Additionally lower p_T leptons typically have a worse energy resolution and one would not like to use poor quality leptons as selected ℓ, even when it still has a fairly high probability of originating from a parton level ℓ. This implies that an optimization of the good lepton and the secondary veto lepton is analysis dependent. An optimization of the ℓ definition should increase the significance in total but will also change the background composition by reducing the Di-leptonic $t\bar{t}$ background.

After cut 5 there were 1124 $\pm$ 32 SUSY events with 862 $\pm$ 28 of these corresponding to the 1 ℓ decay channel for 1 fb^{-1}. The $t\bar{t}$ background had 108 $\pm$ 3 events remaining. As explained above, the composition of $t\bar{t}$ background is of interest here. Of these 108 events only 14.7% are Semileptonic because the m_T is very efficient at reducing them. There are other methods for reducing the Semileptonic channel which will be dealt with in other studies. This implies that an increase in the significance for the Leptonic $t\bar{t}$ is not as problematic as it may seem.

Additionally, a better understanding of the event leads to better possibilities for cuts. The secondary lepton veto not only eliminates the Di-leptonic $t\bar{t}$ events but also eliminates events which contain ambiguous or poorly measured objects. These objects are unwanted because they lead to a less certain understanding of each event. It is also quite possible

that these poor quality leptons could be fakes. One would expect similar fake rates from objects such as these between signal and background but in a SUSY region the $t\bar{t}$ is biased toward strange events. These events are more common to have issues so they should be eliminated.

Of these 108 events, the Di-leptonic events comprise 38.0% and the remaining 47.3% are the tau events. There are specific SUSY tau searches ongoing. There are also tau veto analyses which are the same as a single ℓ search but veto if a tau is found. This would serve to eliminate a good portion of the tau background. Since tau reconstruction is not available with early data these analyses are not possible with early data either.

The two lepton events passed to this cut stage because a lepton from the ME was not reconstructed with values to pass the selection. 24.8% of these leptons were electrons, 20.1% were muons and 54.6% were Hadronic Taus. This implies that an optimization of the secondary veto lepton definition may increase significance by eliminating the events with the missed ℓ. Loosening the secondary veto lepton definition will also cut additional SUSY events. In principle a 2 ℓ SUSY search could accept a 2 lepton event removed by this cut.

7.3.1 Isolation Optimization

This portion of the study was done with ATLFAST-II in version 14 on the same samples validated in the previous section. This is mainly a background study and the full GEANT4 $t\bar{t}$ simulation only had 535,250 events so the choice was made to use ATLFAST-II with 5,000,000 events. The mSUGRA SU4 point was also used with ATLFAST-II in order to be consistent.

The selection defined above had the isolation set to ETCONE20 $<$ 10 GeV. It was hypothesized that adding p_T dependence to the isolation cut could improved efficiency without degrading the purity. This was based on the fact that a higher energy ℓ would have more calorimetric energy outside the electron cluster. An optimization study was

done on Medium electrons and Combined muons. They were were tuned to a linear cut of the form,

$$\text{ETCONE20} < A + B \cdot p_T^{\ell} \ , \tag{7.4}$$

where A is a constant with units of GeV and B is a dimensionless constant. The parameters $A \in [0, 15]$ GeV and $B \in [0, 0.35]$ were varied. This was done first for the good leptons then for the secondary veto leptons. The electrons and muons were done separately but similar patterns and results implied that the same cut values could be chosen.

Several figures of merit were considered, such as signal significance ($\frac{S}{\sqrt{B}}$), the Di-leptonic $t\bar{t}$ rejection and the single ℓ channel SUSY selection. The signal relative to the Di-Leptonic background was more important than to the whole Leptonic sample. Cuts were chosen as the loosest values for which the rate of change for cutting Di-leptonic $t\bar{t}$ events was significant. This means that the rate of change of Di-leptonic $t\bar{t}$ events for loosening the values was small. This was somewhat complicated by a lack of statistics in the high ETCONE20 region. Since this was ATLFAST-II MC and ETCONE20 is a calorimetric variables, one would expect differences to full simulation as well as in data. The final values chosen were:

$$\begin{aligned} \text{Good Leptons} &: \text{ETCONE20} < min(5\ GeV + 0.25 \cdot p_T^{\ell}, 50\ GeV) \\ \text{Secondary veto} &: \text{ETCONE20} < min(10\ GeV + 0.25 \cdot p_T^{\ell}, 50\ GeV) \end{aligned} \tag{7.5}$$

with the additional hard cut at 50 GeV being a cut on the region where statistics were too limited and extrapolations were therefore untrusted. Following this choice each of the 4 isolation cut choices were tested. This was done by varying the A and B values of one of the isolation requirements again to see if the chosen value was acceptable. With the

limited statistics available no further optimization was strongly motivated. The variation of the secondary veto muon is shown in table 7.3 as an example.

7.3.2 Lepton Quality Investigation

Changing the p_T and isolation is not the only way to loosen the secondary veto lepton definition to identify Di-leptonic $t\bar{t}$ events. Quality criteria and different algorithms can be used to recover the missed ℓ. The most obvious quality requirement to change is to eliminate events where there was a crack muon[‡] which was not reconstructed as a Combined muon. This means adding them to the secondary veto muons. Additionally, the secondary veto electron definition was lowered to the Loose quality. These changes were applied to the analysis of the previous section along with the isolation criteria of equation 7.5. There were some independent studies that attempted to optimize the isolation cuts for MuTag and StandAlone muons but proved to not be useful. On the other hand, it proved more profitable for Calo muons since their fake sources are more dramatic. The isolation cut was taken as ETCONE40 $< \frac{1}{3}p_T$ for Calo muons.

If one would like to optimize the ℓ selection one needs to select a region which represents the final topology. Doing the optimization after cut 5 allows for a SUSY region to be selected as well as leaving more statistics than if optimization was done after all cuts. The event requirements following cut 5 (m_T) are not expected to have a significant effect on the $t\bar{t}$ background composition or the lepton distributions. This is because these cuts are simply enhancement cuts and do not significantly change the phase space selected.

Following these changes to the analysis there were 889 ± 28 SUSY events with 695 ± 25 from the single ℓ channel after cut 5. Of the 84 ± 2 remaining $t\bar{t}$ events, 14.9% were Semileptonic, 35.6% were Di-leptonic and the remaining 49.5% were tau events. This is compared to 38.0% of the 108 event in the standard analysis being Di-leptonic. Clearly the fraction of Di-leptonic events was lowered but so was the total number of events (862

[‡]Crack muons are Calo, Tagged and StandAlone muons.

Table 7.3: Table showing variations done on the secondary veto muon for 1 fb^{-1} at 14 TeV. Event numbers shown are after all event cuts.

Cut Parameter		SU4		$t\bar{t}$	
B	A	All	1Lept	All	DiLept
0.00	0	313	250	16.2	4.7
0.05	0	291	243	13.9	3.5
0.10	0	286	239	13.6	3.5
0.15	0	282	236	13.6	3.5
0.20	0	277	234	13.2	3.3
0.25	0	275	233	12.9	3.3
0.30	0	274	231	12.8	3.3
0.35	0	273	231	12.8	3.3
0.00	5	277	234	13.5	3.4
0.05	5	273	231	13.1	3.3
0.10	5	270	229	13.0	3.2
0.15	5	269	227	12.9	3.3
0.20	5	266	225	12.8	3.3
0.25	5	266	225	12.8	3.3
0.30	5	263	221	12.7	3.3
0.35	5	262	221	12.7	3.3
0.00	10	266	225	13.2	3.3
0.05	10	265	224	12.9	3.3
0.10	10	265	223	12.8	3.3
0.15	10	263	221	12.7	3.3
0.20	10	260	219	12.7	3.3
0.25	**10**	**257**	**216**	**12.7**	**3.3**
0.30	10	256	215	12.7	3.3
0.35	10	256	215	12.6	3.3
0.00	15	261	220	12.9	3.2
0.05	15	261	220	12.7	3.2
0.10	15	259	218	12.8	3.3
0.15	15	257	216	12.6	3.2
0.20	15	256	215	12.5	3.2
0.25	15	256	215	12.3	3.2
0.30	15	256	215	12.3	3.2
0.35	15	256	215	12.3	3.3
∞	∞	233	197	10.6	2.5
Ave. Stat. error		15	13	1.1	0.3

$\rightarrow$ 695). It is obvious that there should be fewer events because loosening the secondary veto lepton is effectively making cut 1 tighter.

The two lepton events which passed cut 5 deserve further investigation. They passed cuts because a lepton was missed; 23.0% because of an electron, 19.3% because of a muon and 57.3% because of a hadronic tau. Ideally one would like to find all missed electrons and muons. However this is impossible because even with looser definitions one would not expect to find all leptons. Detector coverage and inefficiency is an inescapable source of missed objects.

Of the missed electrons only 51.5% were eGamma candidates, so nearly half of those missed were not reconstructed as an electron even without any quality criteria. Recall that to become an eGamma candidate a track must be matched to a cluster. 62.7% of those which were not found as candidates had an electron cluster matched to the truth particle. The issue here is that no track was found. If a track is found then there is almost always a cluster so a looser definition of what qualifies as an electron track would recover a significant amount of electrons. These may have poor resolution or a high fake rate, so the track quality must be considered carefully.

Many of the electron candidates reconstructed would not have passed the p_T or η topological cuts. Although no η cut is applied before requiring isEM bit 0, it is clear that an electron outside the tracking region will not be found. 27.7% passed these topological cuts as well as being a candidate but 17.5% additionally passed Loose criteria. The question of why $\approx$ 10% failed Loose can now be addressed in context. 64.3% of those failing Loose failed the second isEM bit, ClusterHadronicLeakage[§]. The hadronic leakage cut imposes a maximal value for the amount of hadronic energy in the first layer relative to the electron cluster energy. This was found to be problematic in the $\eta \approx 1.1$ region as the first layer is not adequately covering this region. This problem can be solved by using an additional hadronic calorimeter layer in the $0.8 < |\eta| < 1.37$ region. Another

[§]See table 5.2.

25% of those failing Loose failed ClusterMiddleWidth. This is a very powerful variable for reducing background and this cannot be omitted without an unacceptable increases in fakes.

The muons are slightly more complicated. By including the crack muons in the secondary veto muons events which have muons of reasonably high quality are being cut. This implies the possibility of using the crack muons of sufficient quality as good muons.

7.3.3 Lepton Quality Optimization

Since events are cut based on the difference between good and secondary veto leptons they must be optimized together. The expected performance of each algorithm was discussed with the combined performance groups to determine an educated choice of initial lepton selection. The properties of leptons which failed the selection criteria of good and secondary veto leptons were studied. Alternative good lepton definitions were tested for the most obvious possible changes but the focus was on the optimization of the secondary veto leptons. All foreseeably useful modifications to the definitions for the secondary veto leptons were attempted and the optimal selection was chosen. Several figures of merit were considered in order to quantify beneficial in this context. The exact manner in which the optimal selection was chosen will be discussed at length in the following verification section.

The final optimization study discussed here was done with Athena release 15. The major purpose of the update from version 14 was that several of the more important failure modes mentioned in the last section were corrected. Between Athena release 14 and 15 the eGamma candidate definition loosened to include lower tracking quality as was motivated. There were a number of changes in the tuning and the range division for the parameterized isEM bit cuts. Also, many bug fixes and MC production modifications were made which would subtly affect the analysis.

The final study was done on fully simulated events in with the same generation as

above but reconstructed in Athena 15.3.1.6. The subtleties dealt with here cannot be assumed to be adequately represented by ALTFAST-II so full simulation was used for this study. In release 15 Anti-k_T jets became available. For reasons not discussed here this is a clear choice over a simple cone algorithm [81]. Also events with jets flagged as bad are removed because there is a subtle interplay with the ℓ and overlap removal. The bad jet definition here is to remove events where there is a jet with $p_T > 20$ in the $|\eta| < 3$ region which satisfies any of the following criteria:

1. It is out of time by more than 50 ns
2. n90 ≤ 5 and HECfrac > 0.8
3. EMFrac > 0.95 and Q > 0.8
4. It has no tracks and is $|\eta| < 2.4$ with less than 7 clusters and EMFrac < 0.2 or less than 2 clusters
5. fCor > 0.50

The final good electron selection was found to be a standard[¶] reconstructed electron with Medium quality. It is required to have $p_T > 15$ GeV, not to be in $1.37 < |\eta| < 1.52$ and to be isolated according to equation 7.5. Overlap removal is applied.

The final good muon selection was taken as all isolated muons in the Staco family with $p_T > 15$ GeV with the following additional cuts. MuTag muons with only one segment and no TGC phi hits are excluded because it is very unlikely for them to pass through so many detectors without interactions. Overlap removal is applied.

In a standard style analysis the secondary veto leptons differ by only the p_T and the good electrons not being in the crack region. A standard analysis where the secondary veto leptons are defined as such can be attempted. This will serve to illustrate how the final choice of the secondary veto leptons is motivated. To lower statistical error, the cuts were loosened to:

1. One good lepton, and no additional secondary veto leptons

[¶]Standard in this context means not the forward or low p_T algorithms.

2. At least 4 jets with $p_T > 20$ GeV within $|\eta| < 3$ and no bad jets
3. Leading jet $p_T > 80$ GeV with the following 3 $p_T > 40$ GeV
4. $\not{E}_T > 80$ GeV
5. Transverse mass: $m_T > 120$ GeV
6. Effective mass: $M_{\text{eff}} > 700$ GeV
7. Transverse sphericity: $S_T > 0.2$
8. $\not{E}_T > 0.2 \cdot M_{\text{eff}}$

This cutflow for $1fb^{-1}$ is given in table 7.4. As cut 5 is the important stage it is bracketed by lines. Only the numbers at this cut stage were used as a tool for optimization.

Table 7.4: Cutflow for an analysis which is intended to be taken as a standard for ATLAS mSUGRA 1 ℓ plus 4 jets searches.

Cut	1 truth ℓ SUSY	Di-Leptonic $t\bar{t}$	S/B	$S/\sqrt{B}$	Leptonic $t\bar{t}$	S/B	$S/\sqrt{B}$
No Cuts	35955	26772	1.34	219.75	217060	0.17	77.17
Lepton	18001	8875	2.03	191.07	108736	0.17	54.59
4 Jets,	13587	2986	4.55	248.62	76647	0.18	49.08
Jet p_T	7570	600	12.61	308.96	21819	0.35	51.25
$\not{E}_T$	5613	293	19.11	327.48	6466	0.87	69.80
m_T	1660.47	90.45	18.36	174.60	311.05	5.34	94.15
M_{eff}	822.90	32.31	25.47	144.77	108.62	7.58	78.96
S_T	576.86	20.50	28.14	127.40	56.71	10.17	76.60
$\not{E}_T/M_{\text{eff}}$	439.82	10.25	42.90	137.37	24.79	17.74	88.34

For this standard style analysis, 21% of the $t\bar{t}$ events which pass cut 5 are Semileptonic. 50% of the events are tau events. The remaining 29% are the Di-leptonic events which are relevant for optimizing the secondary veto leptons. It is clear that the optimizations are highly dependent on choice of good lepton. As mentioned above the good lepton choice was largely based on recommendations from the performance groups.

As before the two lepton events pass selection because of missed leptons. 21% of those missed were electrons and 17% were muons.

Of the electrons that were missed 22% had no candidate found. This is significantly reduced from Athena release 14 because of the lowered tracking. Tracks are never found matching to the truth lepton for any reasonable track quality so this cannot be lowered further. However, for 46% there was a cluster found. This means that they could be reconstructed as a jet if the energy was significant. 18% of these unreconstructed missed electrons did reconstruct as a good jet. For the electrons which were reconstructed as candidates 52% had a $p_T > 10$ GeV and half of those passed Loose. This means that the lowering of the electron quality to Loose is well motivated.

For the muons there were 35% which were not reconstructed by one of the Staco family algorithms. Most of these muons in the tracking region were within $|\eta| < 0.1$, which motivates the use of Calo muons to recover them. Of the muons that were reconstructed 39% failed only because of the p_T cut at 10 GeV. This motivates a reduction of the secondary veto muon p_T. Of those that pass the $p_T > 10$ GeV cut 3% are lost by lack of muon hits. The rest were cut by isolation. This implies an issue with the overlap removal with jets which cause punch-through. There is of course the possibility of not applying the overlap removal for the secondary veto leptons. This would then cut events where there was a reconstructed jet and muon which both had moderate quality.

After many iterations the secondary veto leptons were optimized. The secondary veto electrons are defined as standard electrons of Loose quality with $p_T > 10$ GeV and the isolation of equation 7.5. The muons use all Staco family candidates with the addition of Calo muons with $p_T > 5$ GeV. The isolation of equation 7.5 is applied for the Staco family and ETCONE40 $< \frac{1}{3}p_T$ for Calo muons. No overlap removal was applied for any secondary veto leptons.

The final cutflow with the modified secondary veto leptons can be seen in table 7.5. It shows clear improvement over the standard style analysis in table 7.4. For the single ℓ SUSY channel compared to the Di-leptonic $t\bar{t}$ the $\frac{S}{B}$ is increased by 53.8% and the $\frac{S}{\sqrt{B}}$ is increased by 12.3%. Of the $t\bar{t}$ events which pass the m_T cut 21% are Di-leptonic (from

29%) and there are 48.27 remaining events of the 90.45 events in standard analysis for 1 fb^{-1}.

Table 7.5: The cutflow for the optimized selection in the 1 ℓ plus 4 jets search.

Cut	1 truth ℓ SUSY	Di-Leptonic $t\bar{t}$	S/B	$S/\sqrt{B}$	Leptonic $t\bar{t}$	S/B	$S/\sqrt{B}$
No Cuts	35955	26772	1.34	219.75	217060	0.17	77.17
Lepton	14626	5142	2.84	203.97	87671	0.17	49.40
4 Jets,	10707	1545	6.93	272.39	61864	0.17	43.05
Jet p_T	5961	319	18.65	333.47	18366	0.32	43.99
$\not{E}_T$	4482	158	28.31	356.24	5373	0.83	61.15
m_T	1362.79	48.27	28.23	196.14	227.35	5.99	90.38
M_{eff}	692.87	17.91	38.69	163.73	81.10	8.54	76.94
S_T	485.07	12.20	39.77	138.89	41.14	11.79	75.63
$\not{E}_T/M_{\text{eff}}$	366.51	5.84	62.76	151.67	16.35	22.42	90.64

There are still some two lepton events remaining and only 81% of them are because of a missed tau. 21% of them are because of a missed electron where 74% of those were candidates. Of the candidates 48% passed the topological cuts and 14% of those additionally passed Loose to be cut by isolation. Since only 14% of the candidates in a good topological region passed Loose one could attempt to reoptimize the Loose selection. A reparameterization of the isEM bit cuts for the Loose definition is outside the scope of the work done here.

All of the missed electrons which had no candidate reconstructed had no track but a cluster was found for 41%. 15% of the non-reconstructed electrons would have faked jets without tracks if the bad jet criteria was not enforced. A subsequent study was done on this effect. Of all the jets in the $t\bar{t}$ sample, 0.29% were flagged as bad and 24% of these matched to missed electron. This implies that the bad jet definition plays a subtle role in the optimization of the secondary lepton veto.

The remaining 8% of two lepton events were not cut because of a missed muon. 24% of these muons were candidates and nearly half of those passes the $p_T > 5$ GeV cut but were eliminated by isolation. Further optimization of the isolation cut for these muons

was not possible because of limited MC events. The nearly three quarters of the missed muons which were not reconstructed as candidates were investigated. It is shown in figure 7.6 that these remaining muons were missed in the high or low η regions. This is a direct result of the detector coverage. The Calo muons were specifically intended for recovery in the $\eta \approx 0$ region. They have a very difficult task but some dedicated studies could make improvements there. The $|\eta| > 2.7$ region is clearly a lost cause since there is no tracking or muon systems.

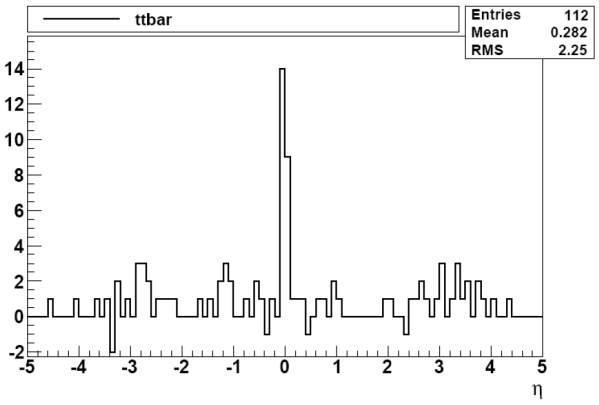

Figure 7.6: The η distribution of the missed muons which were not found by any algorithm. The negative bins are a result of the negative weights in MC@NLO.

7.3.4 Verification of Optimization

One would like to verify that the new definition of the secondary veto lepton given above is optimal in some clearly defined metric. It is obvious that it is an improvement over the standard in table 7.4 but it is not clear that all the changes are necessary or useful. This section deals with a verification using the same figures of merit used to decide upon the final cuts.

To test if this is a stable minimum each of the changes were reverted back to their original value individually to see if the new value was beneficial. To quantify beneficial all of the four figures of merit at cut stage 5 were considered with ordered importance. The $\frac{S}{B}$ is deemed to be more important than $\frac{S}{\sqrt{B}}$ because if one removes some percentage of bad events (those with detector noise for example) the $\frac{S}{\sqrt{B}}$ would decrease while $\frac{S}{B}$ would

be unaffected. The Di-leptonic $t\bar{t}$ reduction is more important than the reduction of the whole leptonic $t\bar{t}$ sample as it is the background that this cut is intended to reduce.

Table 7.6 shows the cutflow for the optimized analysis with the muon p_T cut reverted to 10 GeV. Clearly the 5 GeV cut is a benefit under the metric defined here, since all cut quantities increase except for the least important.

Table 7.6: Cutflow for an analysis identical to the optimized selection but with the muon p_T reverted to the standard value of 10 GeV.

Cut	1 truth ℓ SUSY	Di-Leptonic $t\bar{t}$	S/B	$S/\sqrt{B}$	Leptonic $t\bar{t}$	S/B	$S/\sqrt{B}$
No Cuts	35955	26772	1.34	219.75	217060	0.17	77.17
Lepton	15565	6164	2.53	198.25	93760	0.17	50.83
4 Jets,	11480	1800	6.38	270.59	65712	0.17	44.78
Jet p_T	6390	360	17.73	336.62	19140	0.33	46.19
$\not{E}_T$	4793	182	26.38	355.63	5625	0.85	63.91
m_T	1452.67	57.62	25.21	191.38	244.74	5.94	92.86
M_{eff}	736.22	21.54	34.18	158.62	86.42	8.52	79.19
S_T	522.04	14.66	35.60	136.33	44.64	11.69	78.13
$\not{E}_T/M_{\text{eff}}$	393.92	7.66	51.45	142.37	18.95	20.79	90.50

Table 7.7 shows the cutflow if the Loose electron cut is reverted back to Medium. This shows that this cut is clearly beneficial in the same pattern.

Table 7.7: Cutflow for an analysis identical to the optimized selection but with the electron quality reverted to the standard value of Medium.

Cut	1 truth ℓ SUSY	Di-Leptonic $t\bar{t}$	S/B	$S/\sqrt{B}$	Leptonic $t\bar{t}$	S/B	$S/\sqrt{B}$
No Cuts	35955	26772	1.34	219.75	217060	0.17	77.17
Lepton	15885	6033	2.63	204.51	94691	0.17	51.62
4 Jets,	11802	1984	5.95	264.94	67295	0.18	45.50
Jet p_T	6612	423	15.63	321.50	19925	0.33	46.85
$\not{E}_T$	4957	200	24.71	350.03	5848	0.85	64.83
m_T	1494.74	60.99	24.51	191.40	261.09	5.72	92.51
M_{eff}	747.69	21.54	34.71	161.10	91.36	8.18	78.23
S_T	526.51	14.40	36.55	138.73	47.24	11.15	76.61
$\not{E}_T/M_{\text{eff}}$	398.39	6.75	59.04	153.36	19.47	20.47	90.30

Table 7.8 shows the cutflow for the analysis where the MuTag muons with few hits and the Calo muons are not included in the secondary veto leptons. This is a clear benefit as well. The predominant amount of this comes from the Calo muons. This is because the particular failure mode of the MuTag algorithm is quite rare.

Table 7.8: Cutflow for an analysis identical to the optimized selection but with the same muon algorithms use for good and veto.

Cut	1 truth ℓ SUSY	Di-Leptonic $t\bar{t}$	S/B	$S/\sqrt{B}$	Leptonic $t\bar{t}$	S/B	$S/\sqrt{B}$
No Cuts	35955	26772	1.34	219.75	217060	0.17	77.17
Lepton	14656	5370	2.73	199.98	88023	0.17	49.40
4 Jets,	10725	1601	6.70	268.00	62003	0.17	43.07
Jet p_T	5971	332	17.93	327.23	18399	0.32	44.02
$\not{E}_T$	4489	164	27.33	350.25	5386	0.83	61.17
m_T	1365.34	50.35	27.12	192.42	230.47	5.92	89.94
M_{eff}	694.78	18.43	37.70	161.85	82.01	8.47	76.72
S_T	485.71	12.59	38.59	136.90	41.79	11.62	75.14
$\not{E}_T/M_{\text{eff}}$	366.51	5.84	62.76	151.67	16.48	22.24	90.28

Isolation had a very minimal effect. The muon isolation cut mainly just cut events where there were fake muons from punch-through. This resulted in a decrease in both of the significances at cut 5. Specific methods for reducing punch-through jets are underway. The isolation was optimized for with ATLFAST-II and this has no punch-through.

Overlap removal is similar in this way to isolation. The cutflow for an analysis identical to the optimized selection but where the overlap was applied for the secondary veto leptons is shown in table 7.9. This shows a clear degradation which implies that overlap removal should not be applied. The three most important figures of merit again decrease relative to the optimal definition. It is interesting however that at the last cut stage they all decrease. The larger effect comes from the overlap from muons but the effect from electrons is also significant.

Table 7.9: The cutflow for an analysis identical to the optimized selection but where the overlap was applied for the secondary veto leptons.

Cut	1 truth ℓ SUSY	Di-Leptonic $t\bar{t}$	S/B	$S/\sqrt{B}$	Leptonic $t\bar{t}$	S/B	$S/\sqrt{B}$
No Cuts	35955	26772	1.34	219.75	217060	0.17	77.17
Lepton	16343	6706	2.44	199.57	98694	0.17	52.02
4 Jets,	12186	2205	5.52	259.48	69906	0.17	46.09
Jet p_T	6760	438	15.42	322.90	20012	0.34	47.79
$\not{E}_T$	5034	220	22.81	338.85	5895	0.85	65.57
m_T	1497.29	65.79	22.76	184.59	262.65	5.70	92.39
M_{eff}	754.70	24.79	30.45	151.59	93.43	8.08	78.08
S_T	527.78	16.22	32.54	131.04	48.14	10.96	76.06
$\not{E}_T/M_{\text{eff}}$	400.93	7.66	52.37	144.90	19.85	20.19	89.98

7.3.5 Summary of Proposed Selection

The initial and defining cut of the one lepton channel is the cut on the number of leptons. A modification to this cut was optimized based on Monte Carlo and is expected to become useful with data once the detector is well understood. The cut method is to require one good lepton and veto events with a secondary veto lepton of lower quality. The work here is intended to show that this sort of method is useful for SUSY analyses more than predict the selection which is optimal for data. An additional benefit of this work was the identification and correction of specific failings of the lepton algorithms.

The final good electron selection was found to be a standard reconstructed electron with Medium quality. It is required to have p_T >15 GeV, not to be in 1.37< $|\eta|$ <1.52 and to be isolated according to equation 7.5. Overlap removal is applied in the standard way.

The final good muon selection was all muons in the Staco family except MuTag muons with only one segment and no TGC phi hits. Only muons which are found in the region specified for that algorithm are used. They are required to have p_T >15 GeV and to be isolated according to equation 7.5. Overlap removal is applied in the standard way.

The secondary veto electrons are standard electrons of Loose quality with $p_T > 10$

GeV and the isolation of equation 7.5. The muons use all Staco family candidates with the addition of Calo muons with $p_T > 5$ GeV. The isolation is of equation 7.5 is applied for the Staco family and ETCONE40 $< \frac{1}{3}p_T$ for Calo muons. No overlap removal was applied for any secondary veto leptons.

The Calo muons have an atypical issue concerning them. Their development and optimization was discontinued during the work of this chapter. This implies they will not be appropriate for selection until their development is continued.

7.3.6 Object Definition used in Data

Object definitions have been thoroughly investigated during the initial data taking period. Some aspects have changed relative to the MC studies of this chapter. However, the work here influenced the final definition used for data. Some of the changes in definition were foreseen modifications which amount to simplifications of the algorithms or calibration for early data. Commissioning of complicated algorithms takes more time than simplistic algorithms, so the simple algorithms produce more robust objects for early data. The other cause of modification is the optimization and accommodation for using a real detector. Many unforeseen complications arose from such issues and only the relevant issues will be discussed here.

Muons were defined from within the Staco family of muons. A track isolation requirement of PTCONE20 < 1.8 GeV was applied. The η coverage of the muon trigger system is $|\eta| < 2.4$ so only muons in this region were used. This directly implies that StandAlone muons are not useful. Both MuTag and STACO muons were used in the whole acceptance. Although the MuTag algorithm is not intended for use to recover missed muons in the central region, it was chosen to be used for two reasons. Firstly, no Calo muons are used and the Tagged muons can recover some of the missed muons in the $\eta \approx 0$ region. Secondly, data studies showed that the Tagged muons recovered the STACO muons which were missed because of detector effects. These two algorithms

used in tandem give nearly 100% consistent efficiency between data and MC. STACO muons had an additional cut on their χ^2 of 150. This cut is intended to be high enough into the tail of the distribution to have very little effect but it is still imposed such that muons with anomalously high χ^2 are cut. There was a problem in STACO algorithm for Athena release 15 related to incorrect association of low $p_{T_{MS}}$ muon spectrometer tracks with high $p_{T_{ID}}$ inner detector tracks. This is solved by an explicit cut on muons with $p_{T_{MS}} < 50$ GeV of,

$$\frac{p_{T_{MS}} - p_{T_{ID}}}{p_{T_{ID}}} < -0.4 \ . \tag{7.6}$$

Additional tracking requirements were placed on muons. They were required to have at least 1 Pixel hit and at least 6 SCT hits. For tracks inside the TRT region ($|\eta| < 1.9$) they were required to have greater than 5 hits where no more than 10% were outliers. Outliers are defined as hits which are greater than 5 standard deviations from the fitted track. For tracks outside the TRT region which had greater than 5 hits it was also required that no more than 10% were outliers. Good muons and Secondary Veto muons are defined by the same quality selection. A good muon is required to have $p_T > 20$ GeV and a Secondary Veto Muon is required to have $p_T > 10$ GeV.

Since only the muon channel will be investigated with data for this thesis no electron will pass the Good Electron requirement and all electron events are vetoed by the secondary veto electron. Secondary veto electrons are defined as having the RobustMedium quality. The RobustMedium quality is a modification of the Medium quality which is less sensitive to problematic simulation shapes. Additional topological cuts are $p_T > 10$ GeV and $|\eta_{Cluster}| < 2.47$. Electrons outside $1.37 < |\eta_{Cluster}| < 1.52$ are required to have ETCONE20/$E_T < 0.15$ where electrons inside have no isolation requirement. The optical transmitter data links for the LAr calorimeter which have have failed result in regions with unreliable measurements [33]. Any event containing an electrons built using a cell which feeds into one of these "dead" regions is vetoed.

Chapter 8

Determination of Jet Energy Scale

As seen in the ATLFAST-II study of section 7.2.1, cuts on particular variables can be very sensitive. Similarly, if a distribution is different between data and MC then predictions can be drastically altered. One very important quantity is the so called Jet Energy Scale (JES). This can be represented by the mean of the jet p_T residual defined by:

$$Res_J = \frac{p_T^{reco} - p_T^{truth}}{p_T^{truth}} \ , \tag{8.1}$$

where "reco" refers to reconstructed jets and "truth" refers to truth jets. Another important quantity is the fractional resolution, which is the variance of the residual. Clearly, the intent of JES calibration is to achieve a residual with a mean of 0. Since the p_T distribution can have a large slope, a selection cut can cause a large difference between data and MC when JES is miscalibrated.

The JES is often represented as an energy correction factor, $\frac{E'}{E}$, where E is the measured jet energy and E' is the corrected jet energy. The jet energy is modified such that the 4-vector is varied as the energy scale,

$$E \to E' \implies p^\mu = \langle E, p_x, p_y, p_z \rangle \to \left\langle E', \frac{E'}{E}p_x, \frac{E'}{E}p_y, \frac{E'}{E}p_z \right\rangle = p'^\mu \ . \tag{8.2}$$

There is a large infrastructure in place to calibrate jets but this is time consuming so it may not be up to date. It is unlikely that the JES will be calibrated correctly before all methods have been applied to verify and correct it. Because of this, one would like to attempt to determine the JES from data in the p_T range of interest for analysis.

8.1 Sources of JES Uncertainty

The sources of uncertainty in the jet energy will be outlined in this section. It is important to distinguish between those which result in a general bias to all jets in a particular region and those which give a jet by jet uncertainty. The constant biases will shift the JES and methods to correct for this are discussed in this chapter.

When the detector is simulated in MC production, choices must be made about how the detector is represented. The detector is made to extreme precision but the exact position of all the components can never be known. This results in uncertainty because jets passing through different material have different interaction and detection properties. Issues such as these generally cause shifts in the JES which can be corrected for by parameterization. Updates to the detector description in the MC simulation can also be done but it is a rather long and complicated process to rederive all the calibration constants for a new detector description.

The noise level in each of the calorimeters is also something that must be chosen in MC. If these values are mismodelled then there will be a shift in the JES because of the jet calibration applied. The noise levels in the calorimeter in the absence of genuine signals can be used to constrain the expected noise level when signal is present.

For the LAr calorimeters, the EM calorimeter energy scale uncertainty has been measured in test beam studies, translating into a 3% uncertainty in the scale for operation of the calorimeter [82]. For the tile calorimeter, the EM scale uncertainty of 4% is obtained by comparing test beam, cosmic ray muons and simulation [83]. These values have a

dependency on the jet energy deposited.

Another uncertainty comes from how the calibration weights in the GCW method are derived. Since Truth Jets are used matched to reconstructed jets to derive weightings, small deviations may occur. This can be caused by, for example, the fact that the JES calibration is derived using isolated jets, while most analyses use jets of arbitrary ΔR from each other. This uncertainty is referred to as the closure test of the JES calibration.

GEANT4 has a particular model for the hadronic interaction and shower. Although this is quite well studied with single pion test beam, [84] it is parameterized and as such has an associated uncertainty.

8.2 Hadronic W Decays in $t\bar{t}$ Events

For a search it would be convenient if a data driven determination of the JES was done with one of the major backgrounds. This would mean that most of the jets at the final stage of the cutflow would be calibrated using the exact same sample. It is also practical to have the calibration done with events from the same event stream with the same trigger. Since $t\bar{t}$ production is the dominant background to a SUSY search, a method based on $t\bar{t}$ events will be discussed here. The generator MC@NLO in Athena release 14.2 was used for the sample production.

The first method described below was done for a 14 TeV center of mass energy while the second was done for 10 TeV. During the time of this work it was believed that the LHC would take early data at 10 TeV and then go to the LHC design energy of 14 TeV. Sadly this is no longer the case. The first data was taken at 7 TeV and the energy of upcoming data taking periods has not been fixed yet. This work is intended as a proof of principle for the method. The method should work equally well at different energies with the only effect being a change in luminosity required to accumulate an appropriate number of $t\bar{t}$ events.

The method is to reconstruct the hadronic W decay in the Semileptonic decay channel of $t\bar{t}$ production. Calibration to an invariant mass peak is useful because it directly calibrates to parton level. This requires a selection of the final state $t\bar{t} \to (jjb)(\ell\nu b)$ with the correct jet assignment for the hadronically decaying W Boson. The event selection is chosen to be quite loose in order to get as many events as possible. It is as follows:

1. One isolated lepton with $p_T > 10$ GeV
   (The medium isEM and the Combined muon requirements are applied for the electron and muon identification respectively. Events with electrons in the crack region ($1.37< |\eta| <1.52$) are vetoed.)
2. At least 4 jets with $p_T > 20$ GeV within $|\eta| < 3$
3. At least two of these jets with $p_T > 30$ GeV
4. $\not{E}_T > 20$ GeV

This selection is expected to select $> 40\%$ of the Leptonic $t\bar{t}$ events [36]. It is not expected that all the hadronic W Bosons form two distinct jets. This is predominantly caused by the decay of high p_T W Bosons which will produce two quarks at a small angle. Furthermore, many jets are cut by the preselection requirements. Of the Semileptonic events less than 80% have a W Boson which forms 2 distinct jets passing the preselection. If one would like to reconstruct all 4 jets of the $t\bar{t} \to (jjb)(\ell\nu b)$ topology this issue is compounded. Less than half of the Semileptonic events are reconstructable in this sense. A further issue is that there are often more than just these 4 jets in the event, even when the quarks and jets are matched 1 to 1. This is because of ISR, FSR, underlying event and pile-up.

A combinatorial algorithm produces all the jet assignment hypotheses for each event. First, the 4 jets for a hypothesis of the $t\bar{t}$ event are chosen giving $\binom{N}{4}^*$ combinations where N is the number of all jets. Next, the three jets from the Hadronic top decay are chosen from these 4. This amounts to $\binom{4}{3} = 4$ additional combinations. Then one wants to select the W Boson from within the hadronic top decay, yeilding $\binom{3}{2}$ combinations.

*$\binom{N}{M} \equiv \frac{N!}{M!(N-M)!}$.

Note that the assignment of the 2 light quarks to the W Boson need not be permuted as they are combined to make the mass under consideration.

8.2.1 High Luminosity Method

The first method discussed will be tuned for an integrated luminosity of 200 pb^{-1} at 14 TeV. The selection described above selects predominantly Semileptonic $t\bar{t}$ events. This means that the dominant background is the combinatorial background from incorrect jet assignments. There are

$$\binom{N}{4}\binom{4}{3}\binom{3}{2}, \tag{8.3}$$

hypotheses from each event with only one being correct. Jets can come into an event for a number of reasons and it is not ensured that the 4 hardest jets will be the jets from the $t\bar{t}$ decay. N will be taken as the 6 hardest preselected jets, which yields a maximum of 180 combinations. This choice was based on attempting the full method for several values and choosing the one which resulted in the lowest error on the JES determination.

One can select a hypothesis by making cuts on each combinatorial hypothesis to eventually choose a jet assignment hypothesis. The hypothesis selection method shown here has been tested against other similar methods and found to be superior in all figures of merit. These included the percentage of correctly assigned hypotheses, error on JES determination and stability of fit. The first requirement is to require that the χ^2 is the minimum of all possible combinations. It is defined as

$$\chi^2 = \left(\frac{M_{t_{had}} - 175}{19}\right)^2 + \left(\frac{M_{t_{lept}} - 175}{21}\right)^2 \tag{8.4}$$

where the all number are in GeV. The values for $\sigma_{t_{had}} = 19$ and $\sigma_{t_{lept}} = 21$ were taken from variance of the respective truth matched mass plots. The 175 GeV value is taken from the top mass used in MC generation. In data studies it may be advantageous to

update to the currently measured top mass. The leptonically decaying W Bosons is reconstructed from the lepton and the $\not\!\!E_T$ with an additional $\hat{z}$ component chosen to give the W mass. There are clearly two possible Leptonic W solutions since the choice of the $\hat{z}$ sign is arbitrary. The W Boson is chosen which gives the a Leptonic top mass closer to 175 GeV.

This now leaves $\binom{3}{2} = 3$ possible choices for the Hadronic W. The assignment of the W was taken as the combination with the highest p_T where the jets were within ΔR <1.8. If no such combination is possible then the next best χ^2 is taken.

It is very important to note that any selection biases the mass peak. This means that the JES must be adjusted to match the biased peak. This can be derived from the truth matched distribution. A Gaussian fit to the peak is shown in figure 8.1 with a mean of 78.87 ± 0.24 GeV. A Gaussian is chosen because the shape is expected to be dominated by jet resolution not the natural Breit-Wigner width of a few GeV.

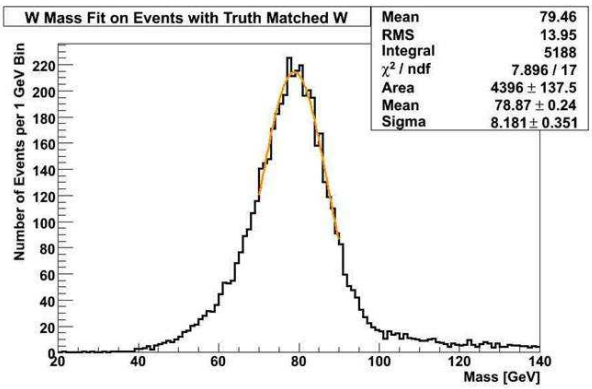

Figure 8.1: The Gaussian fitted W mass distribution biased by the 200 pb^{-1} method.

The combinatorial background has a very distinct shape which is largely determined by the selection. The combinatorial background is fitted to a 8^{th} order Chebyshev polynomial. The fit of the combinatorial background is given in figure 8.2. Both of these fits were done with the total available statistics.

The largest additional background to the combinatorial background is expected to be W+Jets. This and all others are ignored in this study because they are assumed to be negligibly small or easy to model in the Chebyshev fit. This assumption asserts that the

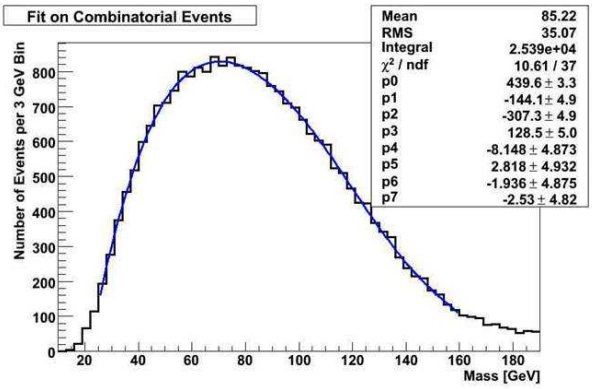

Figure 8.2: The Chebyshev fitted W mass combinatorial background distribution determined by the 200 pb^{-1} method.

optimal choice of method only using the combinatorial background would be the same if all backgrounds were included. Initial studies support this assumption [85]. The relative size of the W+Jets background is shown in the plots of figure 8.3 where each of the W+nJets subsamples are shown overlaid. The sum of these distributions has a similar shape and is smaller than the combinatorial background.

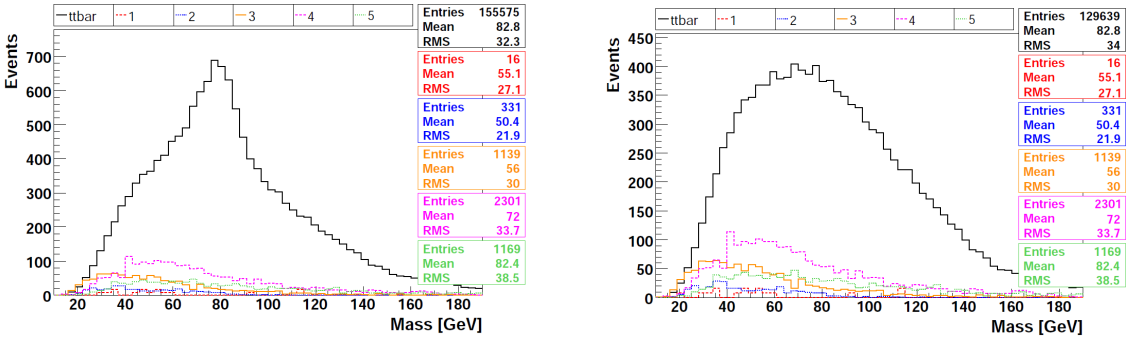

Figure 8.3: The W mass distribution from $t\bar{t}$ with the W+nJets (n $\in$ [1,5]) samples overlaid for 100 pb^{-1}. The left plot shows all samples while the right plots has the correctly assigned hypotheses removed and therefore only shows background.

To reproduce statistical variations relevant for 200 pb^{-1} the number of events expected for this integrated luminosity was used. A combined fit to this "fake data" is then performed with the shape of the Chebyshev polynomial fixed. The parameters of the fit are the W mass (Gaussian μ), the W mass resolution (Gaussian σ), the number of predicted W Bosons (Gaussian normalization), the normalization of the background shape (Bkg Scale) and the mass axis shift of the background shape (Bkg Shift). All of

these parameters are needed to be variable for the fit to avoid unnecessary bias. Fixing anything more than the shape of the background would make unacceptable assumptions about the JES. Although only the W mass and the Bkg Shift are directly related to the JES, correlations in the fit imply that all parameters are JES dependent. The fit is shown in figure 8.4.

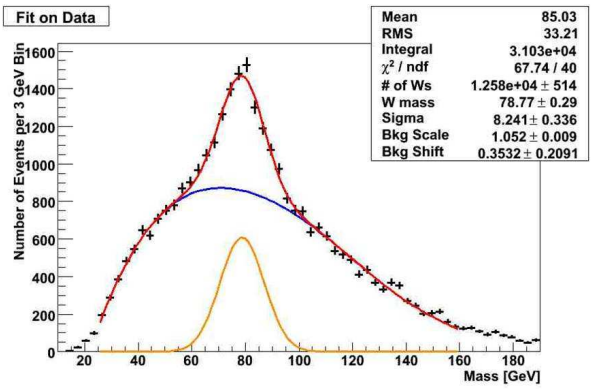

Figure 8.4: The combined fit to extract the W mass for the 200 pb^{-1} JES method.

The most important number in the fit is the extracted W mass of 78.77 ± 0.29 GeV. This compares quite well to the 78.87 ± 0.24 GeV expected from a perfect method. It is also comforting that the variance is reproduced from the Gaussian.

8.2.2 Systematic Error

The statistical error of the fit was given but there may be a substantial systematic error in the method. The dominant source of systematic error in the fit is assumed to be the background shape. The shape of the W mass peak is well understood as a Gaussian shape and all variables in it are allowed to vary. The shape of the background is taken purely from the MC and one would not expect this to be a perfect representation of reality.

To obtain an estimate of the systematic error the background shape is modified in a systematic way in an effort to reproduce possible mismodellings. The Chebyshev polynomial is multiplied by a sinusoidal form:

$$\left(1 - A\ sin(\frac{1}{f}x + \phi)\right)\ . \tag{8.5}$$

The sinusoid is varied in frequency ($f \in$ [3,10]), phase ($\phi \in [0, 2\pi]$), and magnitude ($A \in$[0,0.1]). The order for the polynomial was also changed from 8 to 6, 7 and 9. These parameters form a 4 dimensional grid for possible modifications to the background shape. Equidistant discrete steps are taken in each dimension such that several thousand modifications are made. This modified background shape is then used in the background fit. Because a sinusoid is difficult to model by a polynomial, the free parameters in the polynomial fit will try to compensate for this added shape. This causes the background to no longer be well modelled and the resulting combined fit is worse. If the fitted masses are plotted they form a distribution with a peak at the value of the unmodified background. This should clearly be the case since for low values in the magnitude dimension the shape is minimally modified. An example of such a distribution is shown in figure 8.5 for illustrative purposes.

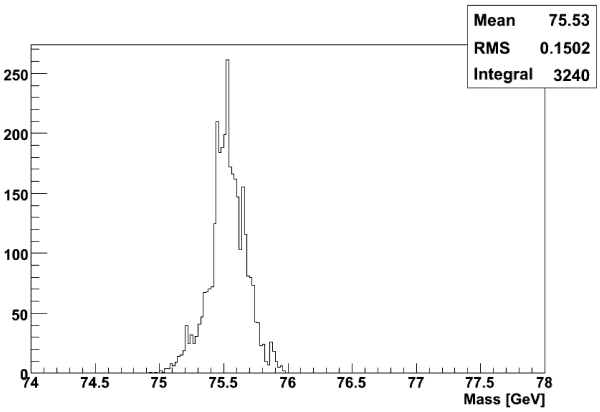

Figure 8.5: Example of a distribution used to determine the systematic error.

The space of these modifications is taken to represent all possible modifications. It is clear that this could not possibly be true but it is quite possible that it spans the space of all reasonable shapes. Several distinct shapes were also attempted, to make sure that some of the sinusoidal modifications were clear over estimates. These included other polynomial forms and clearly ill advised shapes. Fit ranges were also varied to ensure the

fit was robust. The distribution of masses from the sinusoidal fit was found to span this space. The systematic error is then taken to be twice the RMS of the distribution. The extracted W mass is then 78.77 $\pm$ 0.29($stat$) $\pm$ 0.47($syst$) GeV.

8.2.3 Non-global Determination

The method discussed above does not treat jets of different p_T or η differently. In this sense it can be said to be a global calibration. Of course the selection biases the jet distributions, for example no jets below 20 GeV could form the W mass. In SUSY one is generally interested in high p_T jets. Considering SUSY analyses 50 GeV is taken to be high. Although this is somewhat arbitrary it should be clear that one does not want to select jets which are much more than twice the W mass. This is illustrated in figure 8.6 where one can see a peak for the quark p_T around half the W mass. Additionally one can see that the SU4 SUSY point has many jets with high p_T.

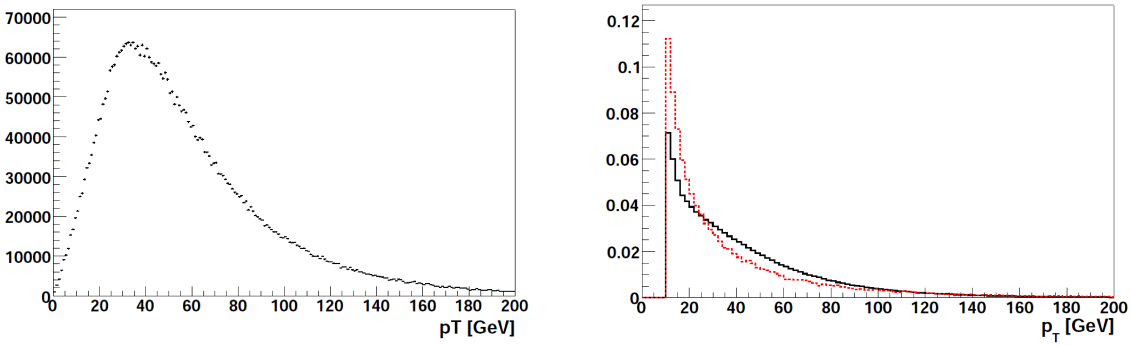

Figure 8.6: The p_T of the light quarks coming from the W decay (left) and jet p_T spectrum (right) for all preselected jets. The SU4 SUSY point is additionally shown overlaid in red with a normalization to unity integral.

The calorimeters are roughly divided into 3 η sections. Although there is some overlap, the barrel calorimeters are inside $|\eta|$=1.5 and the endcap calorimeters are between 1.5< $|\eta| < 3.2$. Outside this are the forward calorimeters which are not commonly used so a maximum jet $|\eta|$ of 3 is imposed. Since these calorimeters are independent subdetectors it is quite possible that there are problems specific to them individually. This implies

that jets in the barrel and endcap regions should be investigated separately.

The analysis is completed as before but events where the W is reconstructed by two jets in the barrel with p_T >50 GeV are separated. These additional cuts significantly change the biases to the shapes. The truth matched W Boson is given as 80.11 $\pm$ 0.30 GeV much closer to the PDG mass than for the global method. The Chebyshev background fit is also rerun and is shown in figure 8.7. The combined fit as well as the systematic error estimation was done to yield a mass extraction of 80.41 $\pm$ 0.35($stat$) $\pm$ 0.35($syst$) GeV. The results are again quite good when compared to the truth matched value. The statistical error is increased due to the further restrictions applied.

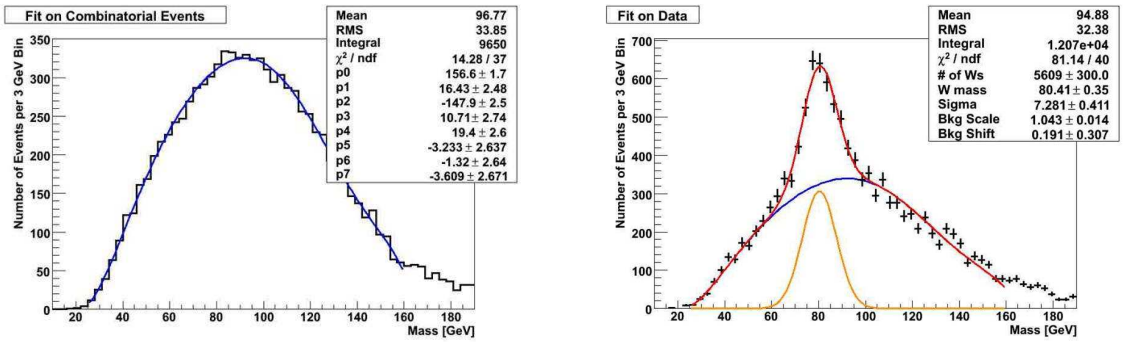

Figure 8.7: The background (left) and combined (right) fits for the barrel region.

This process was repeated for the endcap region, again with both jets having $p_T > 50$ GeV. The truth fit had a mean of 79.14 $\pm$ 0.52. The combinatorial and combined fits are shown in figure 8.8. The extracted mass was 78.22 $\pm$ 0.73($stat$) $\pm$ 0.53($syst$) GeV. Again these results are quite consistent.

8.2.4 Low Luminosity Method

One would also like to see if such an analysis is possible for a data set with which SUSY sensitivity marginally passes existing limits. The value of 10 pb^{-1} was chosen as a goal and a new analysis was designed around it for 10 TeV. The 10 TeV MC was actually 14 TeV MC reweighted to 10 TeV using the relative changes in the parton distribution

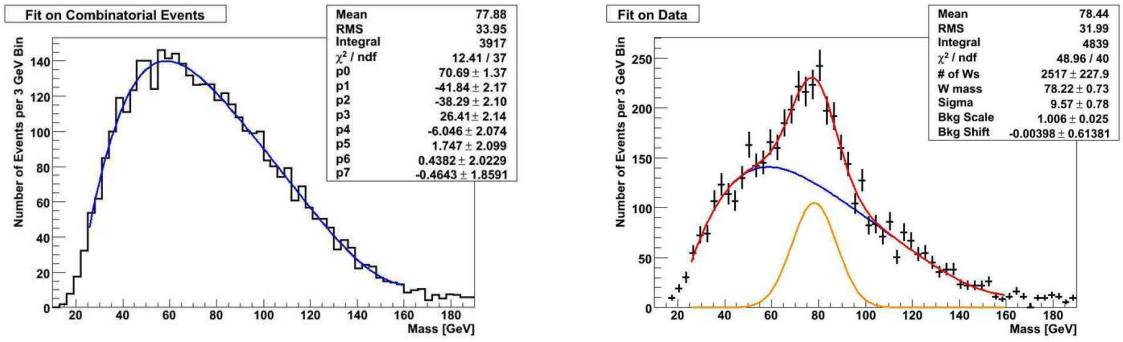

Figure 8.8: The background (left) and combined (right) fits for the endcap region.

functions [86].

The method above uses a combinatorial algorithm which produces many hypotheses. As can been seen from the area of the Gaussian peak relative to the combinatorial background in figure 8.4 an incorrect W Boson hypothesis is chosen more often than not. The method relies more on the modelling of the background than the reduction of it. Certain background shapes are easier to model or produce a better fit for a number of reasons. For example, if the background is relatively flat in the region of the mass peak it is easy to separate the two shapes in the combined fit. The biggest issue when trying to use very early data is of course the statistical error. This inspired the idea to take all combinations. It would be naive to take all the possible combinations since one only wants the correct jet assignment for the hadronic W Boson. If one tries all possible assignments of hadronically decaying W Bosons, there are

$$\binom{N}{2} \tag{8.6}$$

combinations. As before optimization found N=6 to be the best value for the maximum jets to be considered. This gives a maximum of 15 and a minimum of 6 entries per event. One can then proceed as before and fit the truth W mass to obtain 76.9 ± 1.3 GeV. The background fit and the combined fit are shown in figure 8.9. As before a combined fit gives good results, extracting a mass of $75.38 \pm 1.47(stat) \pm 1.71(syst)$ GeV. The higher

errors are a result of the lower statistics.

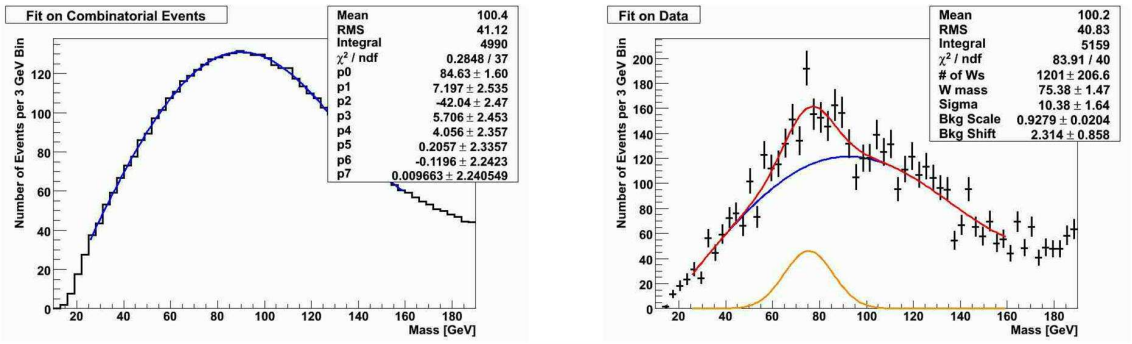

Figure 8.9: The background fit (left) and the combined fit (right) for the 10 pb^{-1} JES method.

8.2.5 Conclusion

There are several methods aside from these to determine the JES. The official calibration methods are more sophisticated than what is presented here and many will be applied before these methods are attempted in data. Up to this point it has only been demonstrated that this method is adequate to confirm the calibration done by these other methods. The methods discussed here are intended as an in-situ calibration as well as a cross check.

To test if these methods can determine the JES miscalibration, the JES was modified as in equation 8.2. All jets were varied up and down by 10% in this manner and the methods were then applied to reproduce the scale factors, $\frac{E'}{E}$.

For the 10 pb^{-1} JES method, these were extracted as $0.905 \pm 0.025(stat) \pm 0.022(syst)$ for 10% too low JES and $1.080 \pm 0.031(stat) \pm 0.022(syst)$ for 10% too high JES. The corresponding fits are shown in figure 8.10. The 200 pb^{-1} methods were also tested for variations of 10%. Barrel and endcap miscalibrations could be determined independently.

The results from the 4 methods in this chapter are summarized in Table 8.1. The precision with which the JES scale, $\frac{E'}{E}$, can be extracted is given under the assumptions stated. When additional backgrounds such as W+Jets are used the peak significance over

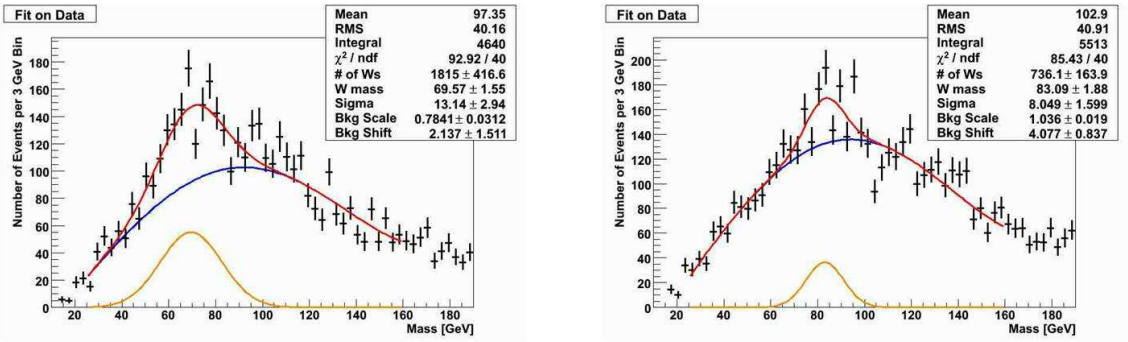

Figure 8.10: The combined fits to extract the scale shift for the 10% low (left) and 10% high (right) scale variations for the low luminosity method.

the background will be reduced and may therefore yield a less precise JES determination. This method is sufficiently robust to use as a JES extraction method for SUSY analyses.

Table 8.1: Summary of the W Boson mass extraction for the 4 JES calibration Methods.

Method	Matched W		Extracted W			Precision
	Mass	*stat*	Mass	*stat*	*syst*	% JES
200 pb^{-1}	78.87	0.24	78.77	0.29	0.47	0.82
Barrel	80.11	0.30	80.41	0.35	0.35	0.73
Endcap	79.14	0.52	78.22	0.73	0.53	1.34
10 pb^{-1}	76.90	1.30	75.38	1.47	1.71	3.5

8.3 Official JES Uncertainty Measurement

As mentioned above, there are several methods for determining the JES. These were performed by the Jet group and the uncertainty was assessed [87].

JES for jets with $p_T > 20$ GeV is known to values $< 10\%$ for all η regions less than 2.8. The η regions used for the estimate of the jet energy scale uncertainty have boundaries at 0, 0.3, 0.8, 1.2, 2.1 and 2.8. This binning closely matches the binning in rapidity of the calorimeter geometry. All individual JES uncertainties are added in quadrature except that from the closure test, which is conservatively treated as fully correlated and added linearly.

Figure 8.11 shows the fractional JES systematic uncertainty as a function of p_T for jets in the two of the η regions; one barrel and one endcap. The total systematic uncertainty is shown as the solid light blue area. The individual sources are also shown, with statistical errors if applicable.

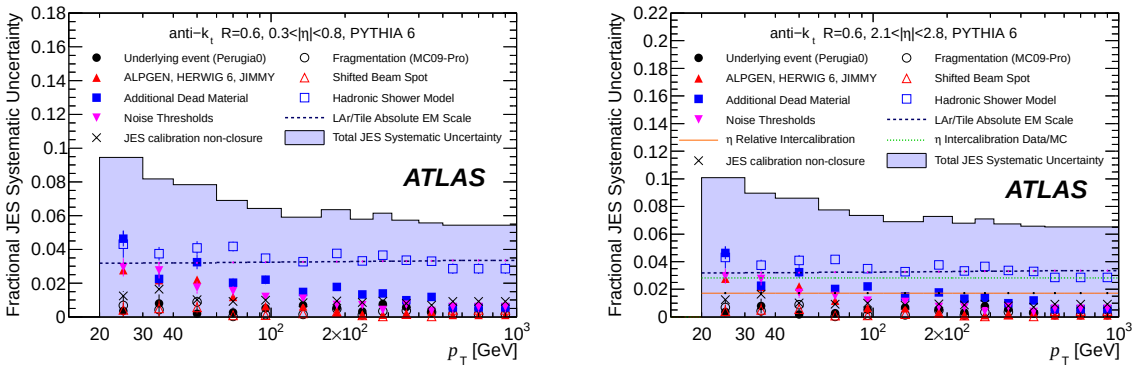

Figure 8.11: The fractional jet energy scale systematic uncertainty as a function of p_T for jets in a barrel region (left) and an endcap region (right). The total systematic uncertainty is shown as the solid light blue area. [87]

The dominant contributions to the uncertainty come from the hadronic shower model, the EM scale uncertainty, the detector material description, and the noise description. The contributions to the JES uncertainty from the hadronic shower model are evaluated using two MC samples, one in which the Bertini nucleon cascade is not used, and one in which the Fritiof model is used instead of the Quark Gluon String fragmentation model. The effect of additional dead material on the jet energy scale has been evaluated with a dedicated geometry model in the simulation, which includes the presence of additional material in front of the barrel calorimeters. The uncertainty on the JES due to possible discrepancies between data and the description of the calorimeter electronic noise in the Monte Carlo was evaluated using MC simulation samples reconstructed with signal-to-noise thresholds for topological cluster seeds and cell neighbours modified to be 10% higher and 10% lower than their nominal values.

Chapter 9

W+Jets Production and Uncertainties

The second largest background to a Single Lepton SUSY search is the W+Jets background where the W Boson decays leptonically. The "+Jets" refers to the additional quarks or gluons that can be produced in association to the W Boson. As was explained in section 5.1 there are many sources of such jets. In this section effects from pile-up will be ignored and the focus will be on the other sources of jets.

Perturbative calculations of jet production in QCD processes have only been performed to next to leading order (NLO) in most cases. Another order in α_s has been calculated for few observables. W+Jets with a high jet multiplicity is a region of phase space where the higher order terms are enhanced. Enhanced higher order terms are associated with kinematic configurations for which the relevant QCD matrix elements are large. In particular, there are enhancements when a soft gluon is emitted or when a light coloured parton splits into two nearly collinear partons. The leading contributions of these soft and collinear terms can be summed to all orders, which significantly improves the convergence of the perturbative series.

The soft and collinear effects can be taken into account by Shower Monte Carlo (SMC)

programs. These programs evolve parton showers down to hadronization scale and run a parameterized hadronization model. The parton shower in SMC programs is a series of successive time-like branchings where each line becomes a source of new branchings. At each branch, a parton with a time-like momentum is emitted and the emitted parton moves to a lower virtual mass. This shower evolves in virtual mass until a no branching step is determined by the Sudakov form factor for a given cut off. Eventually all outgoing parton lines will have terminated branching and the parton shower will cease. At this point all outgoing partons have to be converted into hadrons by the hadronization model. SMC programs are intended to model the hadronization process to all orders through parameterizations but as with all parameterizations it is not exact.

The partons which initiate the parton shower come from a Matrix Element (ME) generator. For a particular diagram the matrix element is exact but the diagrams end in hard, well separated partons. Therefore these must be interfaced with a SMC program to evolve them to low scales. This interface method is normally referred to as the jet matching method. The choice of SMC as well as the interface method is known to provide systematic error [88]. Systematic studies of these issues are of interest when one wants to understand the error on the production of such samples [89].

Several systematic uncertainties which arise in W+Jets production will be discussed in this chapter. Each uncertainty is accessed by generating MC samples with differing values of a related and under-constrained parameter. ALPGEN samples were produced privately on the Mainz tier-3 and each contain about 3,750,000 events of inclusive W+Jets. The cross section differences will be normalized out by the use of a k-factor. The FEWZ cross section of 10,460 $\pm$ 520 pb [42] will be used for all samples.

In order to save time a full chain production as in figure 5.1 was not completed. Instead only the generation stage was done and reconstruction objects were built from the resulting truth particles. This should be acceptable since including the detector effects via simulation should have the same effects on any sample. Reweighting methods

for the largest systematic uncertainty will be discussed in section 9.4.2. Additionally, only samples with the decay $W \to \nu\mu$ were used since the effects for electrons should be similar. Jets used were Anti-k_T Truth Jets of size parameter 0.4. The $\not{E}_T$ was calculated from all calorimetrically interacting truth particles in $|\eta| \leq 3.2$ with the addition of hard muon.

9.1 ALPGEN

ALPGEN [62] is an event generator designed for the generation of Standard Model processes in hadronic collisions with emphasis on final states with large jet multiplicities. This makes it an ideal generator for a process such as W+Jets and is used in ATLAS as the standard W+Jets generator. It is a tree-level matrix element calculator for a fixed number of partons in the final state. It uses the exact leading order calculations for partonic matrix elements in order to provide predictions for final state particle multiplicities. The actual ME calculations are done by the ALPHA algorithm [90]. No contributions from virtual loop corrections in diagrams are used. All mass effects are included in the case of massive quarks. The calculations are done after having selected, on an event-by-event basis, polarization, flavour and colour configurations, in order to be able to provide the SMC with the information necessary for the shower evolution. The sum over polarizations and colours is performed by summing over multiple events.

In a ME generator the term "W Boson" is used as short hand, since what is actually calculated is the matrix element for a Fermion anti-Fermion final state. All spin correlations and finite width effects are therefore accounted for. Since there is choice of the electroweak parameters some specific options are available. Only the default settings were used for the electroweak parameters in this study.

The possible SMC programs are HERWIG [60] and PYTHIA [59]. These are interfaced using the Les Houches format [58] following a specific Jet-Parton Matching scheme.

ALPGEN version 2.13 with Athena version 15.6.8 will be used for all studies in this chapter. Generation is done at a center of mass energy of 7 TeV with the CTEQ6L1 parton distribution function [91].

9.2 Jet-Parton Matching

Parton showers are used to relate the partons produced in a simple, hard interaction characterized by a large ($>> \Lambda_{QCD}$) energy scale to the partons at a lower energy scale where hadronization occurs. At this lower scale a transition is made to a non-perturbative description of hadronic physics. A hadronization model is intended to convert these low scale partons into physical particles. Quarks and gluons will never be detected as single particles in the ATLAS detector because confinement forces them to quickly form colour singlet objects.

ME calculations give a description of a specific parton topology, which is valid when the partons are energetic and well separated. Furthermore, it includes interference between diagrams with the same external partons but different internal structure. The description in terms of a fixed order of emissions is not valid for soft and collinear kinematics because it cannot include the interference between multiple gluon emissions which cannot be resolved. If an external line of a QCD Feynman diagram with momentum, p, and mass, m, emits a gluon of momentum, q, then there is a propagator factor of,

$$\frac{1}{(p \pm q)^2 - m^2} = \frac{\pm 1}{2p \cdot q} = \frac{\pm 1}{2\omega E(1 - v cos\theta)}, \tag{9.1}$$

where ω is the energy of the gluon, E and v are the energy and velocity of the parton emitting it and θ is the angle of emission. This results in collinear ($\theta \to 0$) enhancements for light ($v \approx 1$) partons and soft ($\omega \to 0$) enhancements.

Parton showering from the hard parton to the hadronization scale is possible, because highly virtual partons obey an evolution equation that can be solved analytically or

numerically [92]. However, the evolution equation only includes the soft and collinear fragmentation that is logarithmically enhanced, so that non-singular contributions are ignored. This means that not enough energetic or large angled gluons are emitted from the shower.

It is quite convenient that the ME and SMC have opposite issues. The matrix element is problematic in the soft collinear region while the parton shower is the most accurate in this region. The parton shower description of hard scattering would be improved if information from the matrix element were included when calculating emission probabilities. A systematic method for this can be developed by combining the SMC and ME for fixed topology given by the ME. The parton shower description can be improved by using the exact clustered ME prediction. This clustering is essentially a backward evolution of the parton shower which results in a probable shower history. The clustering sequence is stopped after the eventual identification of a 2 - 2 configuration which is taken as the hard process and defines the starting conditions. It is used to reweight the matrix element by factors which assume the clustered structure was the actual parton shower. The parton shower is then used to continue the evolution of the ME external partons down to hadronization scale. The starting scale of each parton given to the parton shower is determined by the invariant mass of the mother parton belonging to the QCD splitting identified by clustering. This ensures that the correct transverse energy*, k_T, is used to start the shower. Subsequent showering must be done under the constraint that any emission harder than the cut off in k_{T0} is vetoed. This cut off represents the softest parton created by the ME and the hardest parton created by the SMC.

The rate for a given topology from simple born level processes is the product of 3 factors:

1. The Born level cross section for the hard process
2. Analytical Sudakov form factors representing the probability of no emission on each

*Transverse relative to the previous line not the beam as with p_T.

quark and gluon line

3. The strong-coupling branching factors at each clustered vertex

It is vital to ensure that α_s is calculated at the correct scale, and that the Sudakov form factors are inserted on all of the quark and gluon lines. This then provides an interpolation scheme between the parton shower and the matrix element prediction.

The general rate prediction for a given topology is somewhat more complicated. First, one needs to calculate the cross section for the full initial and final state. Then, one needs to specify a particular internal topology. It can be determined by the clustering algorithm which is only permitted to make physically allowed parton combinations on the initial matrix element configuration. The identified cluster vertex k_T values are taken as scales in the strong-coupling constants, α_s, and replace the predefined choice in the initial generation. The Sudakov weight attached to the matrix elements accounts for having no further radiation resolvable below the cut off scale.

The rate is more accurate the more similar the final topology is to that of the ME. Events with additional hard jets from the parton shower have a much less accurate rate than for the same topology calculated from a ME with one more jet. This is because gluons which are not generated by the ME do not have their interference terms taken into account. Additionally, the assumption of soft and colinear radiation is no longer valid. A practical solution is to choose the cut-off scale low enough that the matrix element calculations saturate the dominant part of the cross section. Then, an ordinary parton shower can be used to evolve the parton virtualities from the cut off down to the hadronization scale. As mentioned above, it has been shown that the correct method for doing this consists of starting the parton showers at the scale where a parton was created in the clustered topology, and then vetoing branchings with virtualities larger than the cut off within the parton shower. This whole method is referred to as jet matching.

There are several ways this can be accomplished but the different matching procedures follow a similar strategy:

1. A jet measure is defined and all relevant cross sections including jets are calculated for the process under consideration. For the production of a final state W Boson in pp-collisions, the cross sections for the processes pp $\rightarrow$ W + n jets with n $\in$ [0,N] are evaluated.

2. Hard parton samples are produced with a probability proportional to the respective total cross section, in a corresponding kinematic configuration following the matrix element.

3. The individual configurations are accepted or rejected with a dynamical, kinematics dependent probability that includes both effects of running coupling constants and of Sudakov form factors.

4. The parton shower is invoked with suitable initial conditions for each of the external lines. In all cases the parton shower is constrained not to produce any extra jet above a cut off.

The original implementation is the so called CKKW prescriptions [93]. In this scheme the separation of the ME and SMC domains for different multijet processes is achieved through the k_T-measure. k_{T0} is a fixed value used for the cut off called the merging scale. There is a systematic uncertainty associated with how one chooses to perform the matching. It has been shown explicitly for the CKKW prescription that the dependence on k_{T0} cancels to NLL accuracy for e^+e^- collisions. For the case of hadron-hadron collisions the algorithm has been constructed in analogy to the e^+e^- case. However, it should be stressed that it has not been shown that the CKKW algorithm is correct at any logarithmic order in this kind of process.

If matching is done incorrectly a topology can be created such that a jet from the ME and one from the SMC are both created when there should have only been one. This will overweight the cross section in the region with more jets and can be thought of as a double counting. The opposite issue can also occur when a jet which should have been created is not created by either the ME or the SMC. This would result in gaps in the phase space and an underweighting. To avoid this, one should allow branchings from each intermediate and final lines of the clustered ME that were not included in the original ME calculation.

9.2.1 MLM Matching

The CKKW matching requires a full interface between the SMC and the ME such that the appropriate shower information can be shared. This complicates matters computationally. To avoid this one can run the matrix element generation of the hard process, reweight it and then give the partons to the SMC program. The MLM [94] matching prescription is an approximation of the CKKW method which accomplishes this. This is the method which is used in ALPGEN. The algorithm is as follows:

1. The generation of ME configurations for all final-state parton multiplicities, n, up to a given N (W + n partons) is performed. They are defined by the following kinematical generation parameters:

$$\begin{aligned} p_T^{part} &> p_T^{min} \\ |\eta^{part}| &< \eta^{max} \\ \Delta R_{ij}^{part} &> R^{min} \end{aligned} \tag{9.2}$$

   where p_T^{part} and η^{part} are the transverse momentum and pseudo-rapidity of the ME partons, and R_{ij}^{part} is their minimal separation in ΔR.

2. The clustered history structure is defined for each event which is consistent with the colour structure of the event [95]. The renormalization scale of α_s at each vertex is set according to the CKKW prescription for the strong-coupling weight.

3. The k_T-value at each vertex is used as to scale the value of α_s. The factorization scale for the parton distribution is given by the hard scale of the process and determined by a functional form based on the kinematics.

4. Events are vetoed according to the combined weight to get an appropriate phase space distribution.

5. Events are then given to a SMC program. The upper veto cut off to the shower evolution is given by the hard scale of the process. After evolution, a jet cone algorithm is applied to the partons produced in the SMC. Jets are defined by a cone algorithm with a set of matching parameters:

$$\begin{aligned} E_T^{clus} &= p_T^{min} + 5 \text{ GeV (or } 0.2 \times p_T^{min}) \\ |\eta^{clus}| &< \eta^{max} \\ R^{clus} &= R^{min} \end{aligned} \tag{9.3}$$

where E_T^{clus} is the minimum transverse energy, η^{clus} is the maximum η and R^{clus} is the cone size.

6. Starting from the hardest ME parton, the jet, which is closest to it in ΔR is selected. If the distance between the parton and the jet is smaller than 1.5 $\times R^{clus}$, one says that the parton and the jet match. The matched jet is removed from the list of jets, and the matching test for subsequent partons is performed. The event is fully matched if each parton matches to a jet with the possibility of extra jets being present.

7. Events from the parton samples with n < N, which survive matching, are then required not to have extra jets to enforce exclusiveness. The rejection of these events replaces the Sudakov reweighting used in the CKKW approach. This prevents the double counting of events, which will be present in, and more accurately described by, the n+1 sample. In the case of n = N, events with extra jets can be kept since it is not possible to generate samples with higher n.

When all the resulting samples from n ∈ [0, N] are combined with appropriate cross sections one obtains an inclusive W+Jets sample. To reiterate; in ALPGEN W+Jets production, N=5 so in one generation one creates 6 subsamples, namely W + 0 Partons, W + 1 Partons, W + 2 Partons, W + 3 Partons, W + 4 Partons and W + 5 Partons. These are then added with weights dependent on their individual ALPGEN cross sections.

9.2.2 Systematic Variations

To evaluate the systematic error which comes from the MLM matching, ALPGEN generation was made with varying parameters. These can then be compared to the Nominal sample which has ATLAS default values. The largest effect from varying the parameters in equations 9.2 and 9.3 comes from p_T^{min}. The Nominal sample has p_T^{min} = 15 GeV[†]. Clearly one would like to vary this value to see the effect on the resulting W+Jets samples. The variations were chosen to be up and down by 5 GeV.

Comparison plots of jet multiplicity and p_T for the two varied samples relative to the Nominal can be seen in figure 9.1. The shape differences are seen in the p_T^{min} region of the p_T distribution. Above p_T^{min} the distribution is relatively flat which implies no large

[†]Other ATLAS defaults will be discussed as their issues arise.

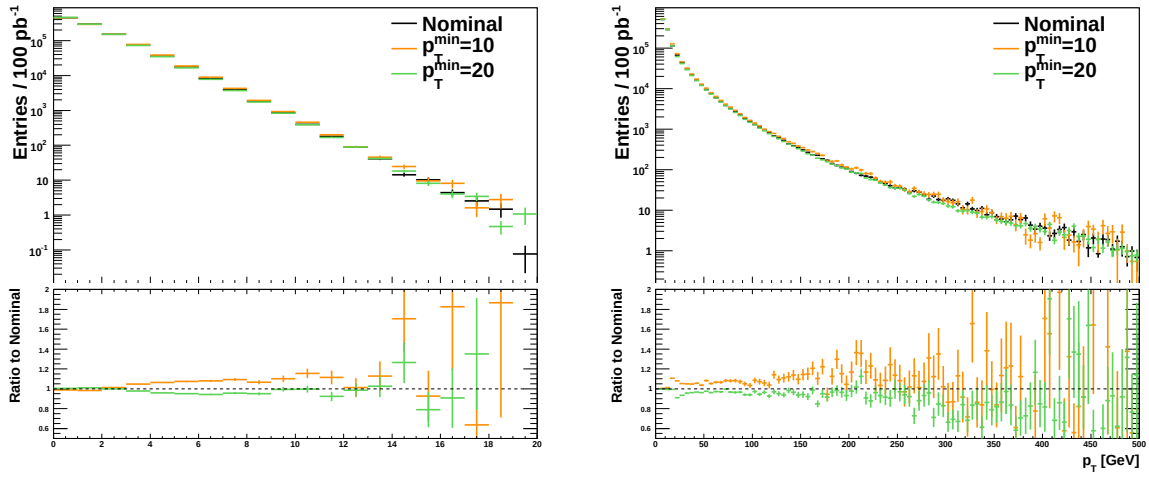

Figure 9.1: Jet multiplicity (left) and p_T (right) distributions for the comparison of ALPGEN with varied p_T^{min}. All jets with $eta < 2.5$ are plotted.

change at that scale. A harder threshold for the energy of the jets, p_T^{min}, means that fewer events are rejected by the extra-jet veto. This implies that a bigger role is given to the shower approximation in the production of jets. Using lower thresholds would instead enhance the role of the matrix elements and reduce the role played by the shower in generating jets.

The jet multiplicity also shows discrepancies in figure 9.1. If a p_T cut above the matching scale is applied the effect should be reduced. Figure 9.2 shows the multiplicity for jets with $p_T > 30$ GeV and the p_T of the hardest jet. Discrepancies can still be observed in these plots.

As seen before in the ATLFAST-II validation, it is easy for small discrepancies to propagate to large changes in cutflows. To understand this, event numbers in specifically chosen regions were compared. The first is the "1 Jet region", which has the simple requirement of at least one jet with $p_T > 30$ GeV. This means that it is expected that the dominant source of hadronic activity is created by the ME. The second region is the "W Boson Control Region" which is normally defined by cuts on $\not{E}_T$ and m_T to preferentially select W events. The W Boson Control Region was chosen to be 30 GeV $< \not{E}_T <$ 80 GeV and 40 GeV $< m_T <$ 80 GeV with the additional requirement of 2 jets with $p_T >$

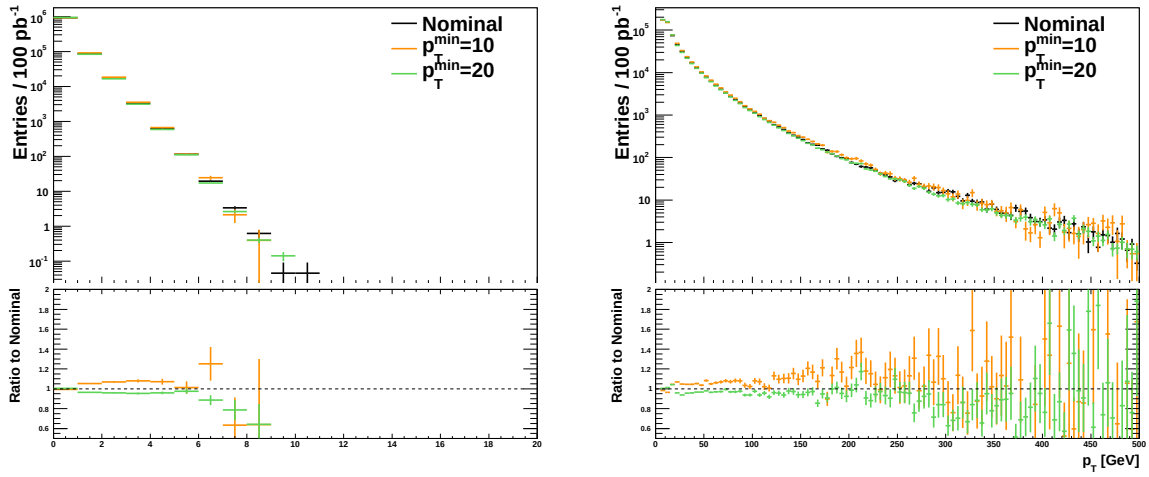

Figure 9.2: Jet multiplicity distributions with $p_T > 30$ GeV (left) and p_T distributions of the hardest jet (right) for the comparison of ALPGEN for varied p_T^{min}.

30 GeV and a lepton of $p_T > 20$ GeV in $|\eta| < 2.5$. The third is a "SUSY Region" which is defined by SUSY cuts mimicking those in the data analysis at the end of this thesis. They are

1. One lepton with $p_T > 20$ GeV
2. 4 jets with $|\eta| < 2.5$ and $p_T^{Jet_1} > 60$ GeV, $p_T^{Jet_{2,3,4}} > 30$ GeV
3. $\not{E}_T > 120$ GeV
4. $M_{\text{eff}} > 500$ GeV
5. $m_T > 100$ GeV
6. $\not{E}_T > 0.2 \cdot M_{\text{eff}}$

The number of events for these three regions evaluated at 100 pb^{-1} can be seen in Table 9.1. There are statistically significant discrepancies from these variations for all regions. This implies an asymmetric systematic uncertainty of $+(19 \pm 32)\%$/$-(20 \pm 111)\%$ when extrapolating to the SUSY region. Because the statistical error on this systematic error was large, differing definitions for the SUSY region with relaxed cuts were investigated. For example, with the m_T cut or the 4^{th} jet cut removed. These looser cuts resulted in lower statistical error on the systematic error and gave comparable results.

Table 9.1: Comparison of ALPGEN events for varied p_T^{min} for three different regions in phase space assuming an integrated luminosity of 100 pb^{-1}.

Region	Nominal	p_T^{min}=10	p_T^{min}=20
1 Jet	107,655 ± 162	113,701 ± 264	103,675 ± 121
W Control	5,475 ± 40	5,774 ± 65	5,251 ± 29
SUSY	0.95 ± 0.33	1.11 ± 0.95	0.77 ± 0.16

9.3 Hadronization

After the parton shower has terminated, partons with virtualities on the order of the cut off scale remain. From this point on, the parton is in the low momentum transfer, long-distance regime in which non-perturbative effects become important. The dominant of these effects is hadronization, which converts partons into observable hadrons. No exact theory for hadronization is known but there are two successful models for parameterization.

The possible choices of SMC for ALPGEN are PYTHIA and HERWIG. Each of these correspond to one of the two parameterization models. The difference between them will allow for the study of systematic errors which can arise from such models. Since each of these models are based on parameterizations, several parameters must be chosen based on data. These so called "tunes" have evolved over time by attempts to constrain particular parameters with data. Because of the large number of parameters and correlations between them, it is quite difficult to know with certainty how well the tunes are performing relative to each other.

9.3.1 PYTHIA

The hadronization in PYTHIA is implemented via the Lund string fragmentation framework [96]. This is a successful implementation of the string model of hadronization [97]. In this model quarks and anti-quarks move out in opposite directions, losing energy to the colour field. The energy in the colour field is modelled as a string of pair particles which collapses. Colour connection is preserved and they then form hadrons. Since gluons

contain multiple colours they connect to two strings to form kinks in the resulting string. Because the particles are space-like separated, the temporal sequence of their breaking is frame dependent. A solution to this issue with the addition of several refinements was the basis for JETSET [98]. JETSET gives hadronic final states for e^+e^- collisions. PYTHIA is the generalization of JETSET to hadron-hadron collisions.

9.3.2 HERWIG

HERWIG hadronization is done through the so called cluster hadronization model. The cluster hadronization is based on the colour preconfinement property of angular-ordered parton showers [99]. This postulates that there exists a preconfinement stage consisting of finite mass colourless clusters of quarks and gluons where the colour neighbouring partons are close in phase space. After the parton shower phase all partons can be uniquely formed into colour singlet clusters. The gluons that remain after the parton shower are split nonperturbatively into $q\bar{q}$ pairs. Due to colour preconfinement, the distribution of the cluster mass spectrum is strongly peaked at low masses. The high mass clusters are split into low mass clusters using a string-like mechanism which is followed by the decay of the low mass clusters to the final state hadrons. It should be noted that HERWIG needs the addition of JIMMY [61] to model underlying event.

9.3.3 Systematic Variations

To evaluate the systematic uncertainty which comes from the SMC and Hadronization models, a comparison between PYTHIA and HERWIG[‡] was made using ALPGEN. The Nominal sample uses HERWIG with a tune which is based on pre-LHC data called ATLAS MC09. The sample with ALPGEN + PYTHIA was made with a newer tune that used early ATLAS data to restrict some parameters. This tune is called ATLAS AMBT1[§] [100]

[‡]When HERWIG is mentioned it is implied that it is used with JIMMY.
[§]This tune is internally called ATLAS_20100001.

and focused on the tuning of the UE. A corresponding newer tune for HERWIG, AUET1 [101], is available and is expected to be the new default for ATLAS ALPGEN production. No fit could be found that described Tevatron and ATLAS data at all energies at the same time so AUET1 was chosen to fit the ATLAS data preferentially. To be consistent with the current Nominal setting the new tune was not used.

The jet multiplicity and the jet p_T distributions are shown in figure 9.3. The jet multiplicity has a significant difference for all values above 4. It is clear that there are differences in the number of low p_T jets and a portion of the ratio plot is expanded to illustrate this. The lack of jets in ALPGEN + PYTHIA is mainly below 20 GeV. This is the sort of discrepancy one would expect since the SMC handles jets in the soft region and $p_T^{min} = 15$ GeV. Additionally, the high multiplicity jets must have been created by the SMC since the ME for ALPGEN can make at most 5 partons.

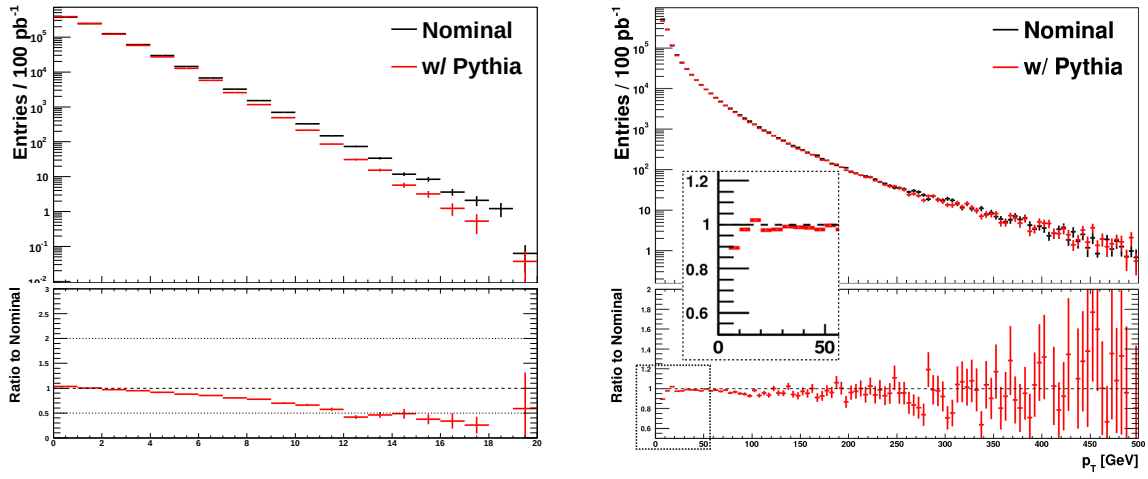

Figure 9.3: Jet multiplicity (left) and p_T (right) distributions for the comparison of ALPGEN with PYTHIA or HERWIG.

As shown in figure 9.4 the discrepancy is enhanced towards large η which additionally points to the fact that this is predominantly an UE discrepancy. The ALPGEN + PYTHIA sample is tuned to early ATLAS UE data whereas the ALPGEN + HERWIG sample is not. Additional studies could be done to verify this by turning off the underlying event in both models.

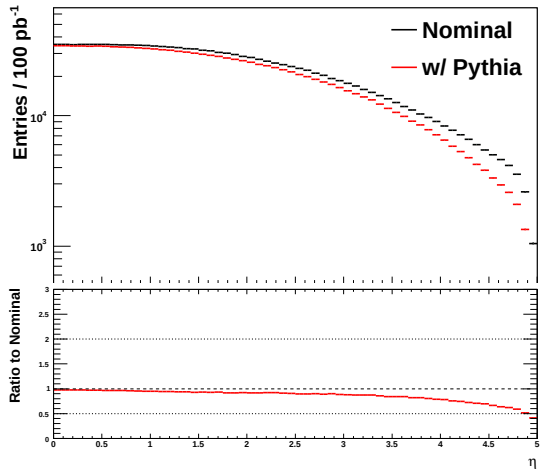

Figure 9.4: $|\eta|$ comparison of ALPGEN with PYTHIA or HERWIG. Discrepancies are enhanced toward large $|\eta|$.

Since this is predominantly an effect coming from the SMC one would expect that it is gone above the merging scale of 20 GeV. Most ATLAS analyses only use jets which are preselected with $p_T > 20$ GeV and $|\eta| < 2.5$. The multiplicity and $|\eta|$ plots are shown in figures 9.5 for jets with these preselection requirements. It can be seen that these effects are no longer significant for $|\eta|$ but the multiplicity discrepancies remain.

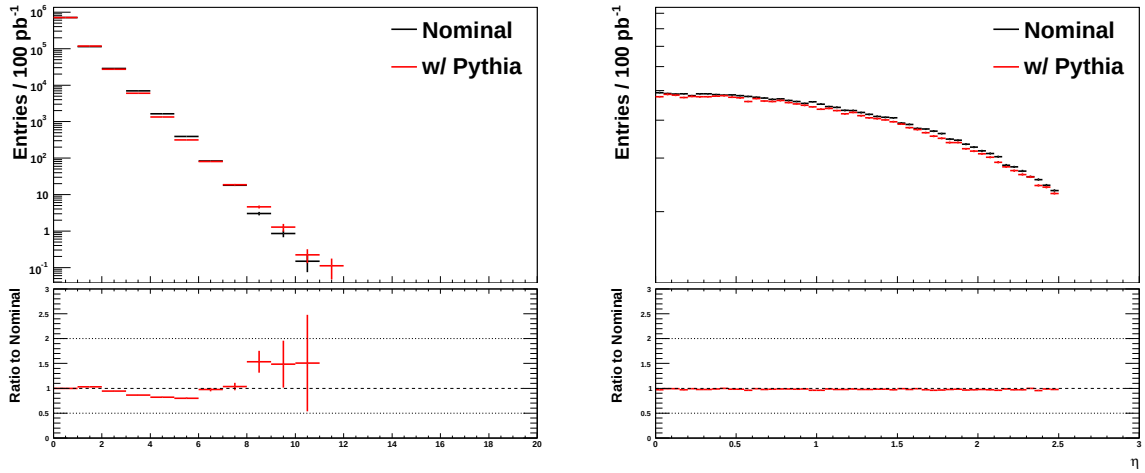

Figure 9.5: Jet multiplicity (left) and η (right) distributions of preselected jets for the comparison of ALPGEN with PYTHIA or HERWIG.

This effect can cause significant systematic error in analyses if they are dependent on low p_T jets. In SUSY analyses jet p_T cuts are typically above 20 GeV. Quantities like M_{eff} and S_T are also built from preselected jets, although, since they are the sum of many

objects small deviations can accumulate. The most sensitive quantity to low p_T jets is $\not\!\!E_T$, which is also used in the calculation of M_{eff}. The comparison plot for $\not\!\!E_T$ is shown in figure 9.6. No significant discrepancies are seen.

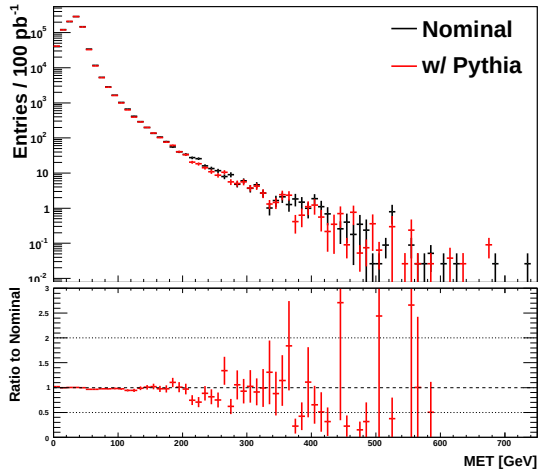

Figure 9.6: $\not\!\!E_T$ comparison of ALPGEN with PYTHIA or HERWIG.

To assess the possible effects of this on analyses the events are compared in the regions described in the previous section. The number of events for these three regions evaluated at 100 pb^{-1} can be seen in Table 9.2. This results in an estimated $\pm(8 \pm 50)\%$ systematic error for extrapolations to the SUSY region.

Table 9.2: Comparison of ALPGEN events between SMC with PYTHIA and HERWIG for 100 pb^{-1}.

Region	w/ HERWIG	w/ PYTHIA
1 Jet	107,655 ± 162	107,604 ± 162
W Control	5,475 ± 40	5,045 ± 39
SUSY	0.95 ± 0.33	0.87 ± 0.39

A more in depth analysis of these systematics could involve using several tunes for each SMC program. Each tune is dependent on a particular parton distribution function so these variations should be done in conjunction.

9.4 Scale

There are two choices of scale which cannot be determined from first principles. The first is the Factorization scale, which determines the energy scale which is given to the proton's parton distribution function to determine the initial state particle momentum. This is generally taken as some functional form dependent on the ME topology. The default for the Nominal ALPGEN W+Jets sample is that the Factorization scale, Q, is determined by:

$$Q^2 = Q^2_{fac}\left[m^2_W + \sum_{partons}\left(m^2 + p^2_T\right)\right]. \tag{9.4}$$

Other choices are available but are either clearly poor choices or are very similar [102]. Since the scale choice comes from neglected higher orders, there is the possibility of an overall scale factor, Q_{fac}, to account for this.

The second scale is the Renormalization scale for the strong coupling, α_s, used in the reweighting factors at each cluster vertex. ALPGEN uses the CKKW prescription for the selection of the renormalization scale. This means α_s thus gets rescaled after the ME evaluation so that each clustered vertex has a local scale. This is the k_T scale used by CKKW defined by

$$k_T = \sqrt{t}z(1-z), \tag{9.5}$$

where t is the scale of the initial particle and z is the fraction of the initial particles energy acquired by the harder outgoing particle [103]. Since it is unclear that this is the correct scale there is an arbitrary choice of scale factor, $k_{T_{fac}}$, available for systematic studies. This then implies that the scale at each local vertex is given by $\alpha_s(k_{T_{fac}} \cdot k_T)$. Error can also arise in the implementations of $\alpha_s(k_{T_{fac}} \cdot k_T)$ because of varying methods for clustering and shower ordering. As with the functional form of Q the k_T functional form is known to be imperfect. Performing a large variation in the multiplicative factors

of these forms is used to get an estimate on their uncertainties.

Any modification of these scale factors will destroy tuning in both the hadronization and the parton distribution function. In ALPGEN the scale factor, $k_{T_{fac}}$, is only changed in the ME not in the SMC so the effects are expected to be artificially small below the merging scale.

9.4.1 Systematic Variations

To find a measure on the systematic uncertainty $k_{T_{fac}}$ and Q_{fac} were varied in tandem. The variation in tandem is motivated by the complex way scales are set within ALPGEN. The ME generation is not entirely independent of $k_{T_{fac}}$, since one has to do the "α_s reweighting" in order to go from the ME calculation with all powers of α_s evaluated at the same scale, to the case where each power of α_s has the scale of the given local vertex. To optimize the unweighting efficiency, information of the value of $k_{T_{fac}}$ is already used at the generation level. This does not imply that they have to be varied in tandem but this justification allows for less MC production.

Two samples were created with a variation by a factor of 2 in both directions, meaning $k_{T_{fac}}$ and Q_{fac} were set to 0.5 and 2 for the creation of these samples. All other parameters were kept consistent to the Nominal sample. Because the tuning in both the hadronization and the parton distribution function are dependent on the scale, it is expected that the variation is larger than what would be obtained if a retuning were performed for each scale.

Additionally, the choice of a factor of 2 is only a rule of thumb. The variations from this are not expected to give a $\pm\sigma$ variation and there is no methodical way to achieve such an estimate. Plots of the jet multiplicity and the p_T distribution are shown if figure 9.7 for the Nominal sample and the two samples with varied scale.

It can clearly be seen that large discrepancies arise from this variation. The HERWIG + PYTHIA distribution is kept to show that the effects are contrary between the ME

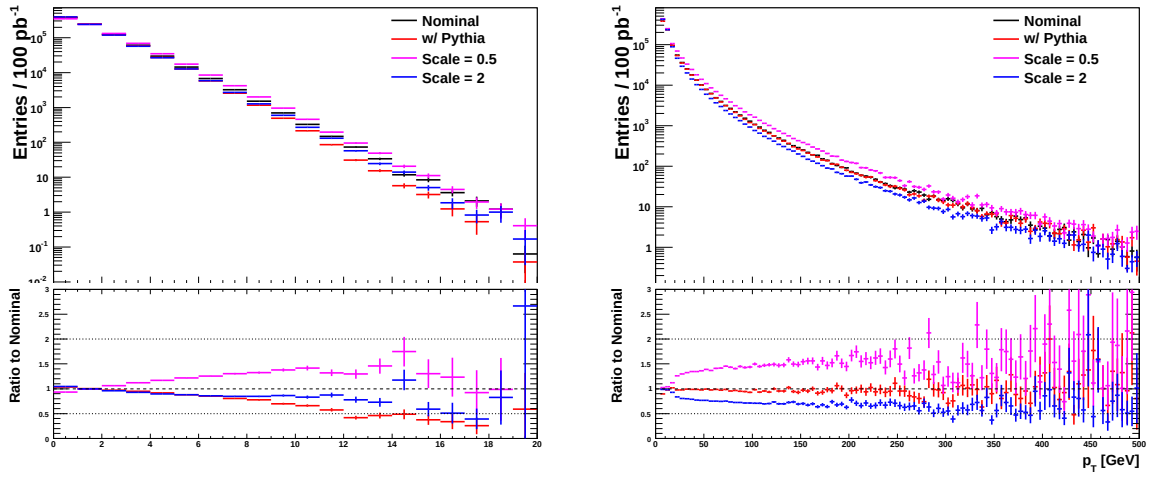

Figure 9.7: Jet multiplicity (left) and p_T (right) distributions for the comparison of ALPGEN for varied scales. Clear differences in jet p_T and multiplicity are seen.

scale and the SMC choice. The scale variation mainly affects the jet p_T for high values whereas the SMC affects the low p_T. This is expected because of the phase space each variation can affect.

Increasing the scale results in fewer and softer jets whereas decreasing the scale results in more and harder jets. It is important to recognize that these variations are affecting the partons coming from the matrix element. This means that the effects seen in figure 9.7 will be present at all parton energies. Figure 9.8 shows the jet multiplicity for preselected jets with $p_T > 30$ GeV. The hardest jet is also shown to be significantly affected.

Figure 9.9 shows the $\not{E}_T$ and H_T distributions for the comparison of ALPGEN for varied scales. The effects propagate to these distributions as expected.

Again a comparison of the event numbers was made in the defined regions and is shown in table 9.3. From this the systematic error for extrapolations to the SUSY region resulting from the scale variation can be estimated as $+(74 \pm 11)\%$/-$(9 \pm 73)\%$.

It is unclear what other functional forms would be theoretically justifiable. The form chosen as the default for the Nominal sample shown in equation 9.4 is the only clearly distinct good choice. Choices in the past have been to neglect either the first or second term in equation 9.4. These have been shown to be poor choices. One possibility for a

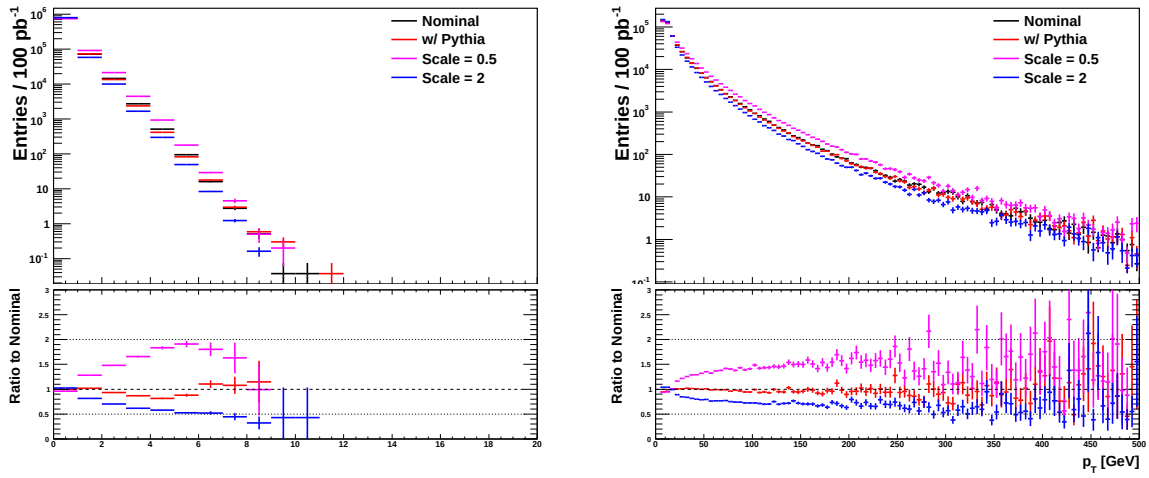

Figure 9.8: Jet multiplicity distributions for preselected jets with $p_T > 30$ GeV (left) and the p_T distribution for the hardest jet (right) for the comparison of ALPGEN for varied scales.

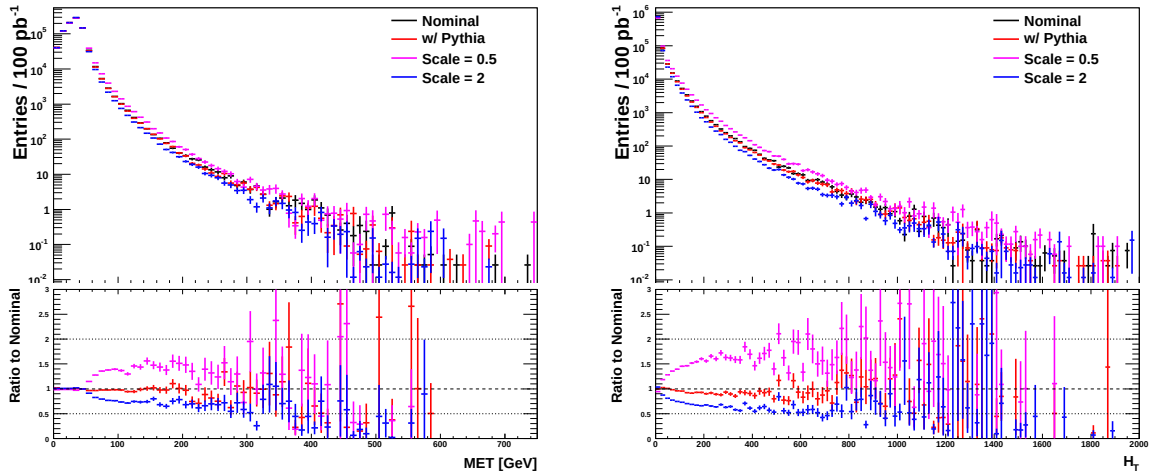

Figure 9.9: $\not\!\!E_T$ (left) and H_T (right) distributions for the comparison of ALPGEN for varied scales. Clear differences are seen for scale variations.

Table 9.3: Comparison of ALPGEN events for varied scales for 100 pb^{-1}.

Region	Nominal	Scale = 0.5	Scale = 2
1 Jet	107,655± 162	143,112 ± 222	84997 ±129
W Control	5,475 ± 40	8,310 ±61	3,825 ± 29
SUSY	0.95 ± 0.33	1.04 ±0.60	0.249 ± 0.065

distinct yet reasonable choice is

$$Q^2 = Q_{fac}^2 \left[m_W^2 + p_{T_W}^2 \right]. \tag{9.6}$$

which effectively has a slightly lower scale. Comparison was done for this but the differences from Nominal sample were minimal. It is quite clear that the $k_{T_{fac}}$ and Q_{fac} variations more than account for any reasonable choice of Factorization scale functional form.

9.4.2 Unscaling Systematic Variations

The changes in scale from $k_{T_{fac}}$ and Q_{fac} can be interpreted in a very simple way. A by-product of the MLM method is that each parton multiplicity, n, in W + n Jets must be generated in its own subsample. These are then added with their corresponding cross sections to form an inclusive sample. To a crude first order approximation each subsample can be thought of as a single tree level Feynman diagram. When $k_{T_{fac}}$ is varied it takes values for the vertexes and lines to adjust the cross section. When Q_{fac} is varied it adjusts the scale which is entered into the parton distribution function. This also effectively only adjusts the cross section. This means that for each of the individual subsamples of the W+Jets sample, only their individual cross sections are changed by the scale variations. As discussed above the total cross section from ALPGEN is experimentally irrelevant so it is only the relative ratios between each sample that change. This is expected to be a better approximation for Q_{fac} than for $k_{T_{fac}}$.

This statement would clearly not be true at higher orders in α_s. Based on k-factors the higher order diagrams can account for up to 20% of the cross section. This means that the distributions contain physics which is not accounted for by ALPGEN and so this is only an acceptable approximation because it is already ignored.

To test this theory one can apply the subsample cross sections of the Nominal sample

to the scaled subsamples. If these distributions agree within a reasonable amount one can then say that this approximation is valid. The plots of this unscaling is shown in figure 9.10. The distributions are statistically consistent.

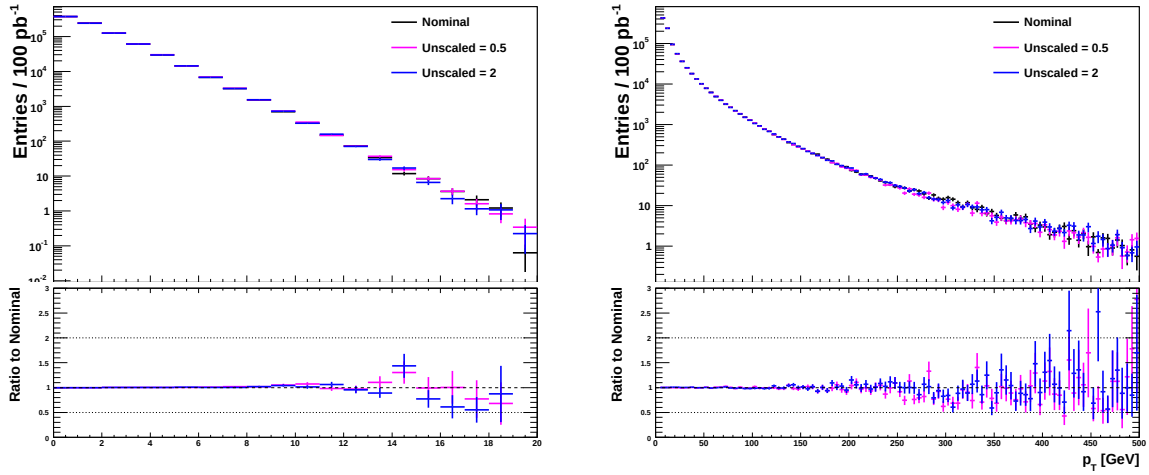

Figure 9.10: Jet multiplicity (left) and p_T (right) distributions for the proof of the unscaling method.

A comparison was also done in the selected phase space regions as above. As can be seen in Table 9.4 there are some differences. One would not expect this crude approximation to work perfectly but it is acceptable for applications. The differences seen are the result of selecting a phase space through multiple requirements where each results in a small discrepancy.

Table 9.4: Comparison of ALPGEN in control regions as proof of the unscaling method.

Region	Nominal	Unscaled = 2	Unscaled = 0.5
1 Jet	107,655 ± 162	107,599 ± 163	108015 ± 162
W Control	5,475 ± 40	5,603 ± 40	5,385 ± 41
SUSY	0.95 ± 0.33	0.48 ± 0.13	0.59 ± 0.36

The accuracy of this approximation means that one can normalize each subsample independently to account for scale uncertainty. The scale could therefore be constrained from measurements in data. Such a method could not be attempted until the other contributions to the jet multiplicity are well understood. This includes UE, JES and

higher order corrections. This being said, there is no fundamentally inconsistent issue with trying to normalize each subsample independently if one admits that they are normalizing out a number of effects.

A safer way to deal with this error is to take the whole variation at face value. If one ran the analysis once for each sample one would get three results. For searches these would correspond to a nominal value and the upper and lower systematic variation. This is how the limits were presented in figure 4.6. Hopefully one would have enough statistics to exclude the sample for a scale of 0.5 and 2 and thus confirm the variation in a data driven way.

Where the unscaling method helps here is with practical considerations. To run three analyses one would need to generate three samples. Because of the statistics required, this would take significant computer power to simulate, even with ATLFAST-II. Instead what one could do is apply a pseudoscaling to the nominal sample to reproduce the scaling. As argued above this could be achieved by changing the nominal subsample cross sections to that of the scaled subsamples. Keeping the overall normalization constant this is then translated to a set of scale factors to adjust the Nominal subsample cross sections by.

Table 9.5: ALPGEN pseudoscaling factors to reproduce the scaled samples from Nominal MC.

Subsample	W+0j	W+1j	W+2j	W+3j	W+4j	W+5j$^+$
Scale up	1.0498	0.8564	0.7230	0.6283	0.5545	0.4846
Scale down	0.9257	1.1947	1.4293	1.6507	1.9276	2.1206

9.5 Normalization in Control regions

The uncertainty values previously given for SUSY extrapolation are large and can be reduced by normalizing first in W control region then extrapolating to the SUSY region. Normalization will reduce a significant portion of the systematic error from each of the effects discussed. Typically one would normalize to the number of data events in a

control region. Instead all samples will be normalized to the Nominal sample. It is only the relative difference that matters so this choice is irrelevant. The expected number of events in the SUSY region are shown before and after control region normalization in table 9.6.

Table 9.6: The effect normalization has on the differing systematic variations.

Sample	SUSY Events		% from
	Before	After	Nominal
Nominal	0.95 ± 0.33	0.95 ± 0.33	–
p_T^{min}=10	1.11 ± 0.95	1.05 ± 0.9	10 ± 100
p_T^{min}=20	0.77 ± 0.16	0.8 ± 0.17	16 ±33
w/ PYTHIA	0.87 ± 0.39	0.94 ± 0.42	1 ± 55
Scale=0.5	1.04 ± 0.60	0.69 ± 0.4	27 ± 49
Scale=2	0.249 ± 0.065	0.356 ± 0.093	63 ±16

The effect from the systematic error can now be derived as the variations from the nominal. It can be seen that this method works as expected for all variations except the lowered scale.

One must take great care when applying a method such as this. In the previous sections the focus has been on the variations which give a large systematic effect when extrapolating from an inclusive W region to a SUSY region. If one normalized in a W control region the systematic uncertainties which are large when extrapolating from there to the SUSY region are of importance. It is possible that the dominant variations are not scale, hadronization and p_T^{min}.

9.6 Sherpa

The systematic uncertainty values derived above are based solely on ALPGEN. The variations done are expected to comprise the dominant portion of the possible MC generation uncertainties. As a cross check an independent generator was investigated to determine if the variations contain those which can come from other generators.

Sherpa [104] is a multi-purpose Monte Carlo generator with special emphasis on

matrix-element/parton-shower matching. The parton-level matrix elements used within Sherpa have been obtained from the internal ME generator AMEGIC++ [105]. Parton showering is conducted by CSshower++ [106], which is based on Catani-Seymour subtraction terms. The combination of the matrix elements with this parton shower is accomplished according to an improved CKKW procedure [107]. The hadronization of the shower configurations is performed by the internal fragmentation module AHADIC [108]. The merging scale, k_{T0}, is fixed to 30 GeV.

In Sherpa both the scale of the ME $k_{T_{fac}}$ and the α_s used in the shower are modified when the scale is varied. A small statistics study was done with privately generated Sherpa 1.1 events to understand this effect. The more consistent handling of α_s gave a lower variation when these scales are varied. Although the scale for the variation was somewhat reduced the overall effect was similar to that of ALPGEN. Figure 9.11 shows the relevant distributions. When comparing with figure 9.7 one can see that the scale variation is not as large. Additionally, with Sherpa the p_T spectrum varies for the whole range whereas with ALPGEN it was suppressed below the p_T^{min} value.

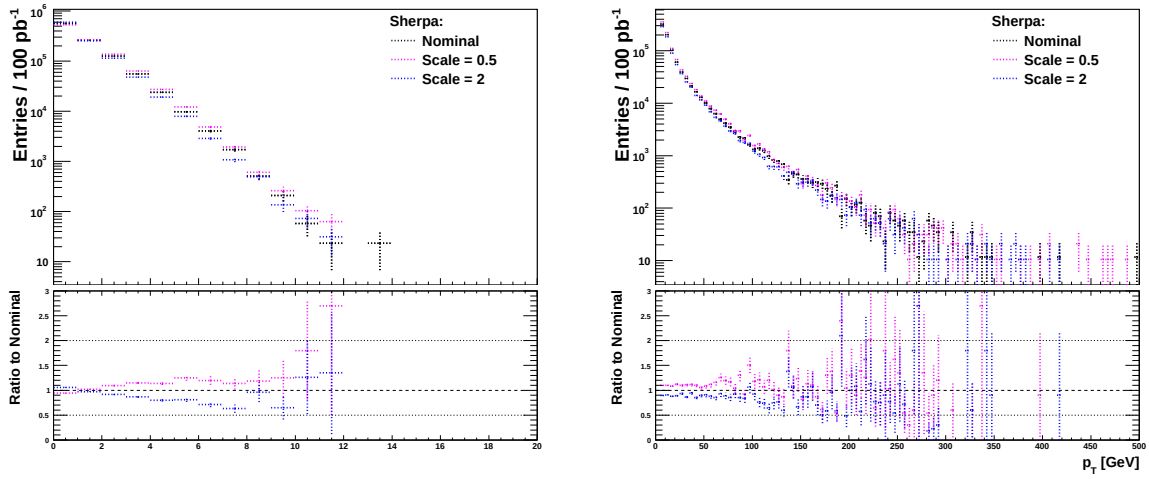

Figure 9.11: Jet multiplicity (left) and p_T (right) distributions for the comparison of Sherpa for varied scales. The variations have similar trends to that of ALPGEN.

Since Sherpa is so different from ALPGEN from the theoretical point of view it is interesting to see if the results are consistent. If this is not the case then an additional

systematic uncertainty is needed to account for this. 1,700,000 Sherpa events were generated officially with Sherpa 1.2. The events were weighted such that events with higher multiplicity would have higher statistics. The jet comparison to the various ALPGEN samples are shown in figure 9.12. It is clear that the multiplicity plot has large discrepancies. The jet p_T only has large shape differences for low values. Additionally these should represent the same inclusive sample so effects which are only due to cross section normalization cannot be ignored.

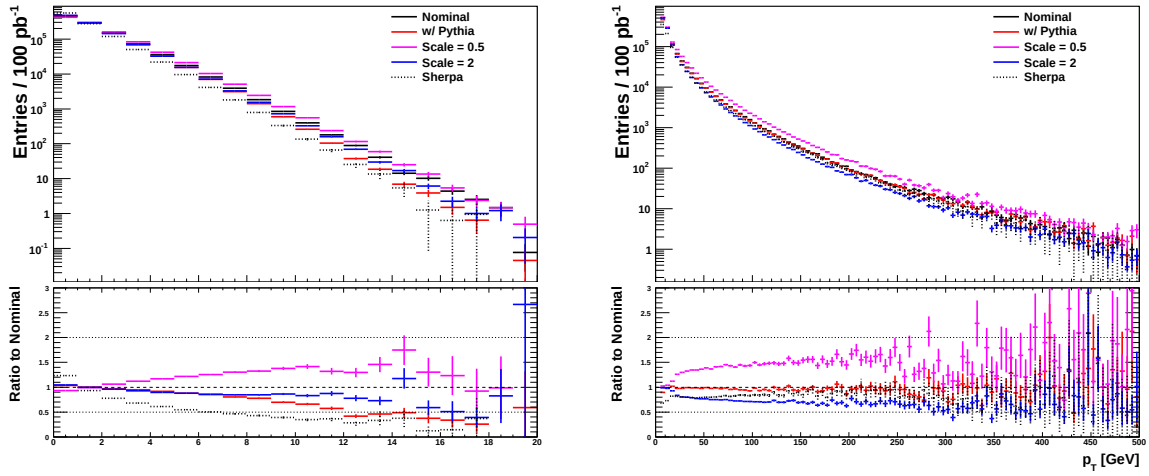

Figure 9.12: Jet multiplicity (left) and p_T (right) distributions for the comparison of ALPGEN with Sherpa.

The effects from underlying event are expected to be visible since there are differing models. This is represented in the η plots shown in figure 9.13. As one would expect the η dependence is largely gone for jets with $p_T > 30$ GeV. The shape differences can also be seen in $\Delta\phi(\not{E}_T, Jet_i)$ and lepton p_T.

These discrepancies in jet multiplicity persists for higher jet cuts as can be seen in figure 9.14. The leading jet p_T is also shown to have a large difference to ALPGEN.

The default parton distribution function used in ATLAS for ALPGEN is CTEQ6L1 with a $\alpha_s(m_Z)$=0.1298 [91]. However Sherpa uses CTEQ66 with $\alpha_s(m_Z)$=0.118 [79]. Having $\alpha_s(m_Z)$ so much lower in Sherpa does somewhat correspond to choosing the scale higher. The Sherpa deviations are within the scale uncertainty and in the direction

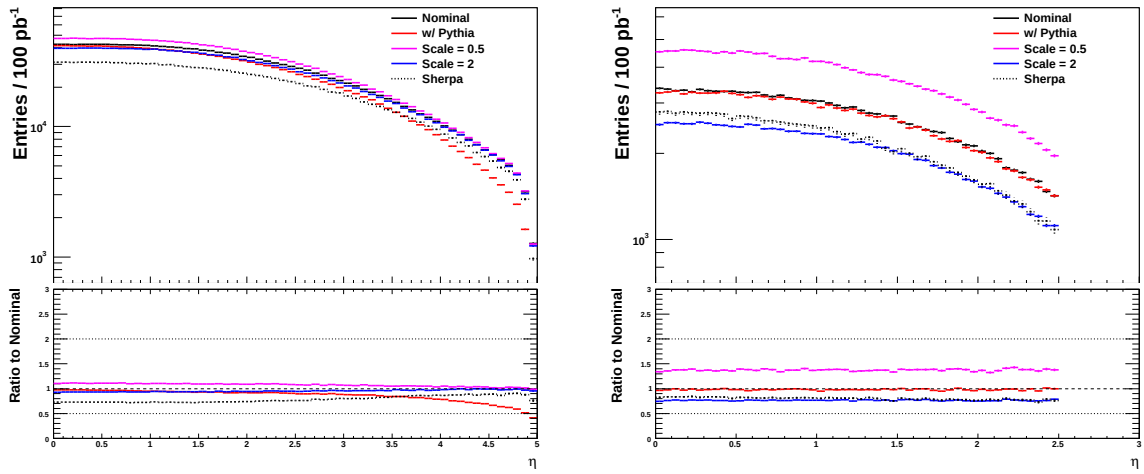

Figure 9.13: η distributions for the comparison of ALPGEN and Sherpa. All jets are shown on the left and preselected jets with $p_T > 30$ GeV are shown on the right.

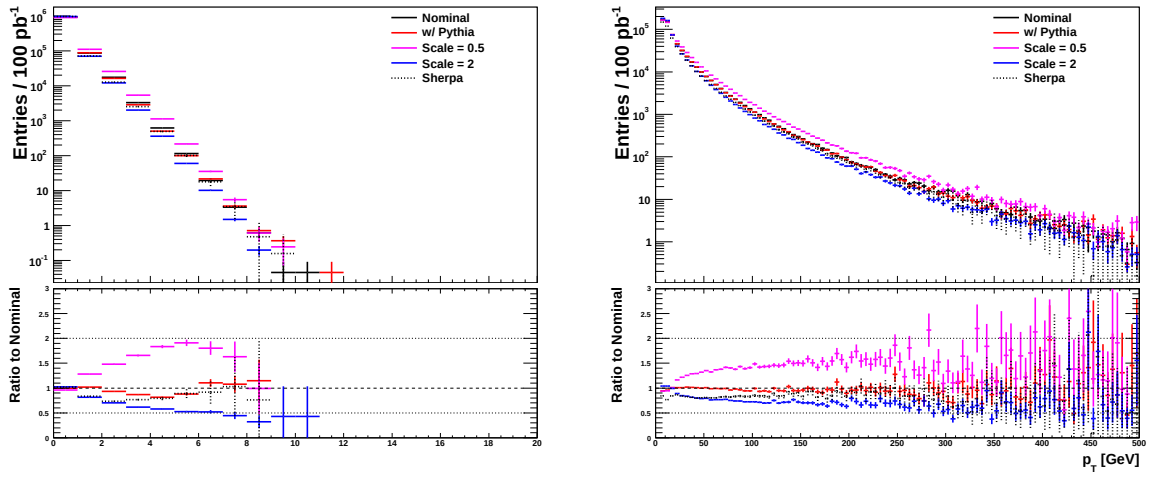

Figure 9.14: Jet multiplicity distributions for preselected jets with $p_T > 30$ GeV (left) and the p_T distribution for the hardest jet (right) for the comparison of ALPGEN with Sherpa.

one would expect from this argument. Better agreement is expected if the same parton distribution function is used for Sherpa and ALPGEN. If one changes the PDF one also has to adjust the value of $\alpha_s(m_Z)$ accordingly and retune the multiple parton interactions. This is outside the level of work here so only the default was used.

The differences seen in Sherpa are highly correlated with the three effects already discussed above. The dominant effect seems to come from the intrinsic choice of scale and the PDF used. This is expected to be studied with data and hopefully constrained. No additional systematic is needed to account for the choice of ALPGEN as the generator. This is not surprising since the major differences between ALPGEN and Sherpa are exactly what have been accessed in this chapter.

Chapter 10

Analysis on Data

All SUSY searches completed to date found data to be consistent with the Standard Model. Of particular interest here are the early searches with lepton requirements [109]. The culmination of this thesis is an extension of the previous ATLAS single muon SUSY searches. Due to several practical constraints the final analysis was only done on muons. The electron channel will be covered in other work and contained in the official SUSY group paper. Much of the work in this thesis will be contained in or overlap with this paper [110].

10.1 Samples Used

Data samples from periods E-I corresponding to the events which were triggered by a single muon were used. Specifically these triggers were EF_mu10_MSonly for periods E-F, EF_mu13 for periods G-H and EF_mu13_tight for period I. These correspond to the lowest unprescaled trigger for the corresponding data taking period. The estimated integrated luminosity for this period is 34.4 pb^{-1} recorded with an 11% systematic uncertainty. This luminosity uncertainty is dominated by the uncertainty on the measurement of the beam current.

The EF_mu10_MSonly was used for all MC events because the triggers used in data

were not all applied in MC. The corresponding trigger efficiency correction is given in table 10.1. These values were measured using a tag and probe method on the Z Boson mass peak.

Table 10.1: Relative trigger efficiencies used to adjust MC to data [111].

	EF_mu10_MSonly	EF_mu13	EF_mu13_tight
Barrel	0.906	0.979	0.962
Endcap	0.975	1.031	0.988
Luminosity (pb^{-1})	2.6	12.7	19.0

The MC samples were created with various generators by the ATLAS MC group. The $t\bar{t}$ background was generated with a modern generator following the MC@NLO scheme called POWHEG [103]. The single top sample however still use the old MC@NLO generator as the POWHEG samples were not available yet. Showers were done with HERWIG for both $t\bar{t}$ and single top. The $t\bar{t}$ cross section was taken as 79.12 pb with a k-factor of 1.13 [112]. For single top, the t-channel cross section was taken as 7.15 pb and the s-channel cross section was taken as 0.469 pb for each lepton flavour. The Wt-channel cross section was taken as 14.58 pb for all lepton flavours combined.

All vector boson samples were generated with ALPGEN using HERWIG showers. The FEWZ NNLO cross section of 10,460 $\pm$ 520 pb was used to calculate a k-factor of 1.2 for the W+Jets samples. Similarly a k-factor of 1.25 was applied to the Z+Jets samples to correct to the cross section of 1,069 $\pm$ 53 pb. Drell-Yan samples were also produced in this fashion.

QCD multijet production was done with PYTHIA standalone. Di-boson samples were made with HERWIG standalone [113].

A grid for signal samples was created in the mSUGRA $m_0 \times m_{\frac{1}{2}}$ plane. The other parameters were fixed to $A_0 = 0$ GeV, $tan(\beta) = 3$ and $sign(\mu) > 0$. m_0 was chosen in the range [40,440] GeV and $m_{\frac{1}{2}}$ in the range [100,220] GeV. Step sizes were 40 GeV for m_0 and 15 GeV for $m_{\frac{1}{2}}$. Generator level cuts were made to require that one of the particles of the hard process was a coloured sparticle. The mass spectrum and branching ratios

were calculated using ISAJET version 7.75 and it was generated with the HERWIG++ generator version 2.4.2 using the MRST2007 LO* parton distribution functions. The inclusive SUSY production cross section was calculated by Prospino at next-to-leading order and is plotted in figure 10.1. As no pile-up was added to the grid points the SU4 sample will be used for distribution comparison plots.

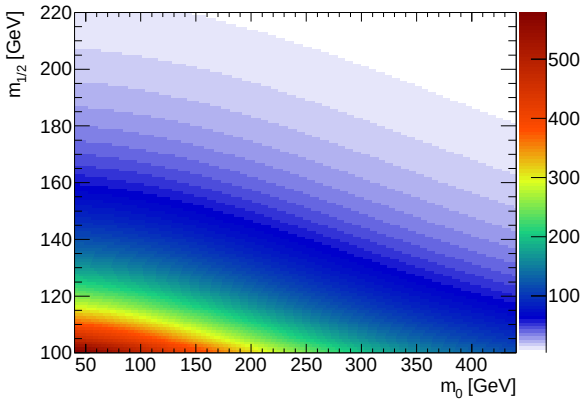

Figure 10.1: The cross sections for the SUSY signal grid in *pb*.

10.2 Event Selection

Events passing the triggers listed above were recorded in a specific muon trigger stream. The event cuts used here closely resemble those used and motivated in previous sections. The following cuts were applied to the samples:

1. Labelled as good by the Data Quality Group
2. Passing specified trigger
3. No bad jets (See section 6.3)
4. One good primary vertex and all high quality muons are associated to this vertex with $|z_0 - z_{PV}| < 10$ mm
5. One Good Muon with $p_T > 20$ GeV (See section 7.3.6)
6. No additional Secondary Veto Leptons
7. The Good Muon is matched to the trigger object
8. $\not{E}_T > 30$ GeV and $m_T > 30$ GeV

9. $p_T^{Jet_1} > 60$ GeV
10. $p_T^{Jet_1} > 60$ GeV and $p_T^{Jet_2} > 30$ GeV
11. $p_T^{Jet_1} > 60$ GeV, $p_T^{Jet_2} > 30$ GeV and $p_T^{Jet_3} > 30$ GeV
12. $p_T^{Jet_1} > 60$ GeV, $p_T^{Jet_2} > 30$ GeV, $p_T^{Jet_3} > 30$ GeV and $p_T^{Jet_4} > 30$ GeV
13. $\not{E}_T > 120$ GeV
14. $M_{\text{eff}} > 500$ GeV
15. $m_T > 100$ GeV
16. $\not{E}_T > 0.2 \cdot M_{\text{eff}}$

Numbers and plots will only be shown after cut stage 5 is applied. The first 4 cuts are mainly to do with cleaning and hold no relevant physics content. They are not expected to be modelled by MC and are mentioned purely to illustrate the selection clearly. These cut stages were compared with other groups for consistency. Cut 8 is applied only to remove QCD from the following cut stages. The MC statistics for the QCD multijet events were low because a muon must be faked for it to enter the analysis. The cuts 9-16 were chosen based on an iterative yet data blind selection. This primarily involved MC investigation and the desire to have SUSY events passing to the final cut stage.

10.3 Pile-up

Various pile-up conditions were present in the running periods used. To accommodate for this the MC samples were generated with pile-up. They were then reweighted such that the vertex multiplicity distributions for vertexes with at least 5 tracks matched with data. This was done in a W control region defined by 30 GeV $< \not{E}_T <$ 80 GeV and 40 GeV $< m_T <$ 80 GeV in addition to cut 7. The same weights were applied to all SM MC samples.

The SUSY signal grid was not produced with pile-up so no reweighting was applied. This is then the most conservative estimate for the pile-up in a SUSY event. Pile-up

would only add additional energy to the event and therefore bring it more towards the SUSY region.

The distribution for the number of vertexes at cut stage 7 is shown in figure 10.2. The nearly flat ratio is a result of the fact that this region is similar to the W control region which it was measured in.

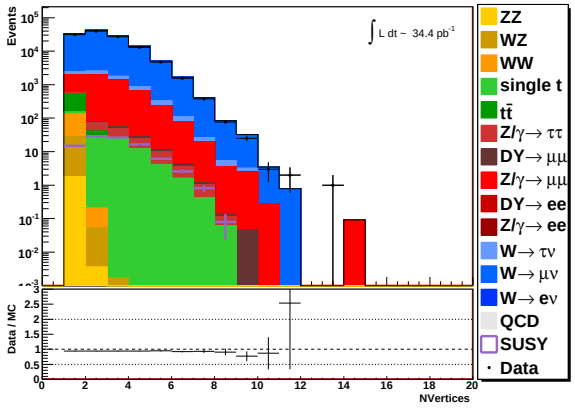

Figure 10.2: The number of vertexes with at least 5 tracks at cut stage 8.

10.4 Results

The cut flow for this analysis is given in table 10.2. The errors given are statistical only. Although the data MC agreement is quite good, it can be seen that there is an overestimate by the MC for some of the intermediate cut stages. There is an 11% uncertainty on the luminosity which is sufficient to account for this discrepancy. Other sources of systematic error will be discussed in the following section. Data and MC are in agreement well within the total uncertainty.

At cut stage 5 the secondary lepton veto has not yet been applied. This means that there are possibly two leptons in each event. The distribution of invariant mass of the two hardest leptons around the Z Boson mass peak is shown in the left plot of figure 10.3. From this it can be seen that the muon resolution is slightly degraded in data. A parameterized muon smearing provided by the ATLAS muon group has already been

Table 10.2: Comparison for 34.352 pb^{-1}.

Cut	QCD	DY	Di-Boson	W+Jets	Z+Jets	Single t	$t\bar{t}$	SUM	DATA
5	71745±16744	3043±20	256.97±0.74	169130±182	25865±49	148.7±1.7	702.6±3.3	270892±16745	270974
6	71293±16739	1853±17	204.72±0.68	168740±182	11392±32	135.4±1.6	574.3±2.9	254192±16740	254551
7	71270±16739	1842±17	203.94±0.67	168076±181	11294±32	134.8±1.6	570.9±2.9	253391±16740	245691
8	1.98±1.23	22.7±1.1	132.74±0.55	118726±153	5495±22	94.3±1.3	401.5±2.5	124874±155	117684
9	1.98±1.23	1.82±0.40	38.96±0.30	3881±22	169.5±3.8	57.2±1.1	342.8±2.3	4493±23	4346
10	1.98±1.23	0.52±0.14	20.06±0.21	1616±12	73.9±2.5	42.61±0.95	329.0±2.2	2084±12	2017
11	0.19±0.07	0.10±0.07	5.77±0.11	426.6±5.9	22.2±1.3	18.29±0.66	263.0±2.0	736.1±6.4	731
12	0.09±0.05	0.00±0.00	1.04±0.05	99.9±2.8	5.37±0.65	4.70±0.32	145.4±1.5	256.5±3.3	255
13	0.00±0.00	0.00±0.00	0.15±0.02	8.73±0.82	0.10±0.07	0.48±0.09	15.52±0.48	24.96±0.96	24
14	0.00±0.00	0.00±0.00	0.08±0.01	6.69±0.73	0.10±0.07	0.44±0.10	10.70±0.40	18.01±0.84	18
15	0.00±0.00	0.00±0.00	0.01±0.01	0.55±0.23	0.04±0.04	0.07±0.05	1.60±0.15	2.27±0.28	4
16	0.00±0.00	0.00±0.00	0.01±0.01	0.28±0.16	0.04±0.04	0.03±0.03	1.27±0.14	1.63±0.22	2

applied to partially correct for this effect. At cut stage 7 it is expected that a well understood muon is chosen. The p_T distribution is shown in the right plot of figure 10.3. Good shape agreement between data and MC is seen.

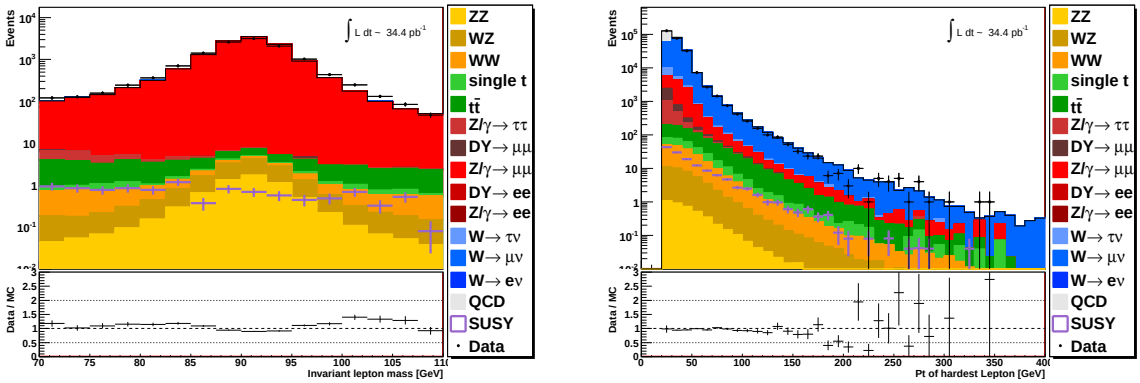

Figure 10.3: The invariant mass of the two hardest leptons at cut stage 5 (left) and the lepton p_T distribution at cut stage 7 (right).

Although the QCD contamination is still large at cut stage 7 it is predominantly at low values of $\not\!\!E_T$. As discussed for the motivation of cut 8, the $\not\!\!E_T$ and m_T distributions should be relatively free of QCD contamination for higher values. This is illustrated in the plots of figure 10.4. The low regions are dominated by statistical error from QCD while the intermediate regions show good agreement between data and MC.

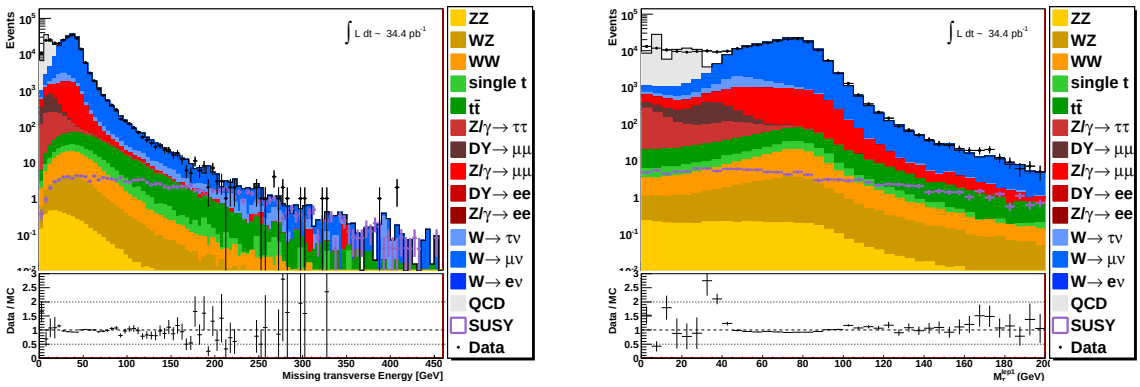

Figure 10.4: The distribution of the $\not\!\!E_T$ (left) and the m_T (right) after cut stage 7.

The W Boson control region should be free of signal contamination and QCD background. It is therefore expected that the distributions are well modelled by the SM MC. There are 78,892 data events where $84,750 \pm 128(stat)$ are expected from MC. This is within the 11% uncertainty on the luminosity. MC predicts that $(95.67 \pm 0.15)\%$ of the events come from a W+Jets event.

The muon term for the $\not{E}_T$ is divided into two components. Although the calculation for the each term is the same, muons are divided by being associated to a jet or not. Since overlap removal is applied with jets of $p_T > 20$ GeV and the minimum jet p_T is 7 GeV the associated jet must be in this range. The two terms are shown in figure 10.5 in the W control region. Aside from the overall normalization difference the distributions are in good agreement.

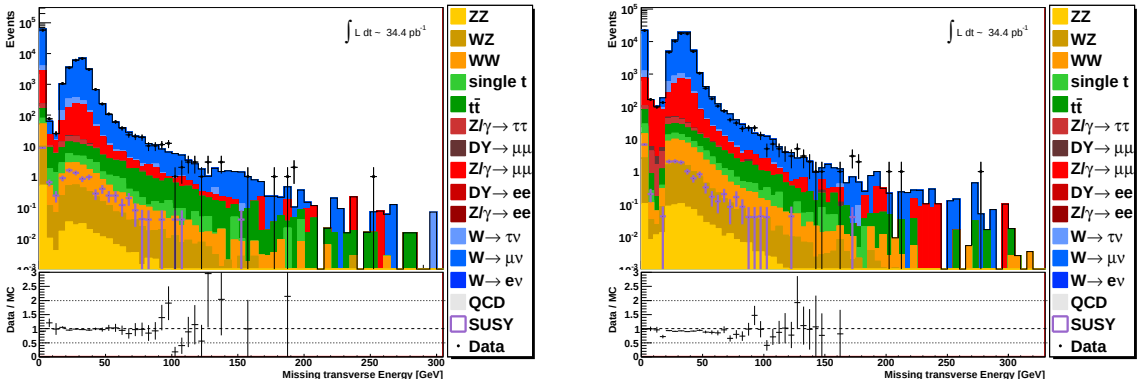

Figure 10.5: The distribution of the muon term for the $\not{E}_T$ divided into muons associated to a jet (left) and those not (right).

As discussed in chapter 9 the jet multiplicity modelling for W+Jets can be problematic. The dominant component comes from the renormalization and factorization scale choice. However, an additional component comes from the fact that k-factors for W+Jets are very likely to be dependent on the number of external lines in the hard process. The jet multiplicity distribution for Good Jets can be seen in the left plot of in figure 10.6. The ratio plot shows an inconsistency in at least the first bin which could indicate these

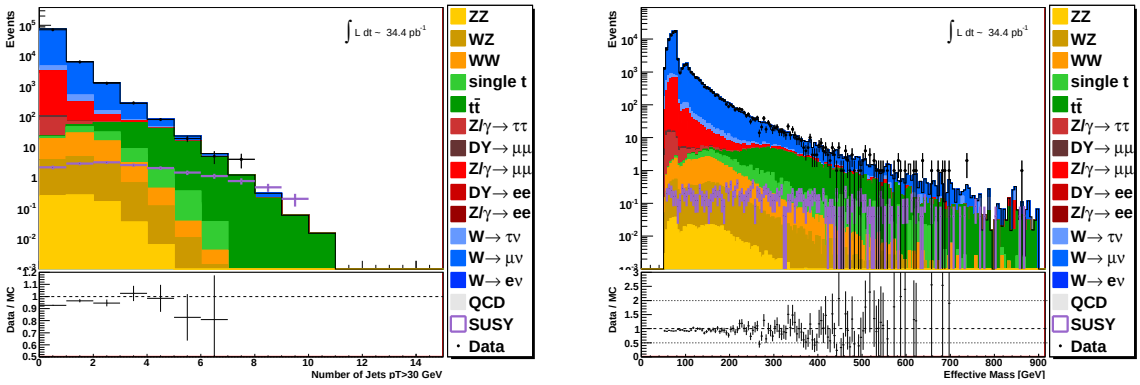

Figure 10.6: The distribution of the jet multiplicity (left) and M_{eff} (right) in the W control region.

effects. The distribution most affected by such a mismodelling is the M_{eff} which is shown to be well modelled in the right plot of figure 10.6. The kinematic edge is a result of the $\not{E}_T$ and jet requirements.

The next few cuts all have to do with the jet p_T. The p_T distribution for each jet is shown in figure 10.7 at the stage directly before it is cut. All are in good agreement within the statistical error.

10.4.1 Systematic Uncertainties

It is clear that the later cut stages have significant statistical error. In addition to this, there are possibly large systematic errors. These can be separated into measurement and MC errors. It is expected that many of these uncertainties can be constrained in the near future. As the current understanding of such constraints is poor, a very conservative approach is taken where no data driven constraint to any MC systematic error is applied. The most simplistic method for constraining systematic error is to normalize in specific control regions as discussed in section 9.5. The 11% systematic uncertainty on the luminosity as well as the error on theoretical cross sections are of the type which could be constrained with such a method.

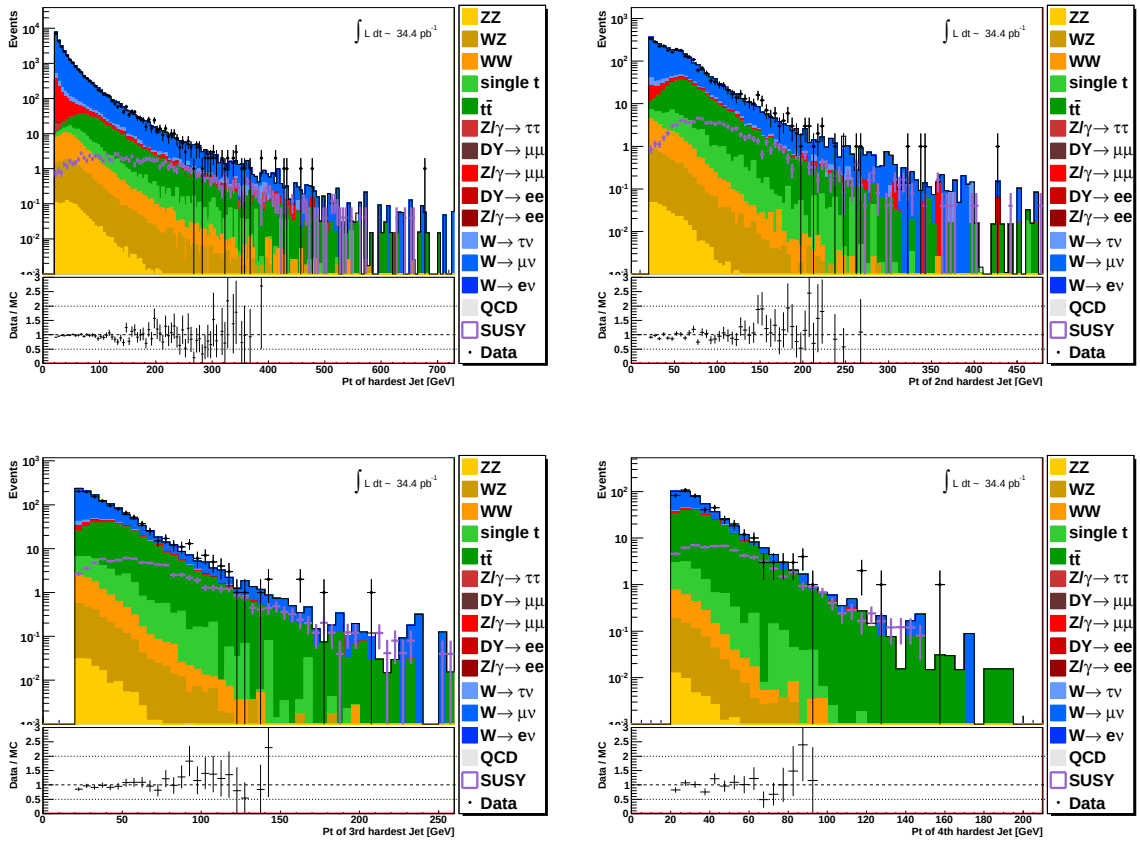

Figure 10.7: The jet p_T distributions before their respective cuts.

As discussed in chapter 9 the ALPGEN modelling uncertainty can be broken into three dominant components; Hadronization, Matching and Scale. Table 9.1 shows the expected number of events for the SUSY signal region and the variations coming from the change in the matching scale, p_T^{min}. This leads to a systematic error estimation for this component of 20%. Table 9.2 shows a similar estimation for the component coming from hadronization of 8%. The dominant component is that of the renormalization and factorization scale. The systematic error for this component is shown in table 9.3 and leads to a 74% uncertainty.

In chapter 9 only generator level properties are used in the selection cuts. An assumption that the variation derived from generation level quantities is a good prediction of the variation from reconstruction level was made. A method for rescaling fully simulated

events to derive the uncertainty from the scale was introduced in subsection 9.4.2. The Pseudoscaling Factors of table 9.5 were applied to the W+Jets MC for all three lepton flavours. The results for the pseudoscaling are shown in table 10.3. At the last cut stage this shows a relative change in predicted number of events to that of table 10.2. This leads to a prediction of an asymmetric systematic uncertainty of $+(46 \pm 41)\%$/-$(71 \pm 140)\%$ from the scale variations in W+Jets events. This calculation of a 71% error matches well with the 74% derived based on generator level cuts. Since the Scale component is dominant over the Hadronization and Matching uncertainties, it was assumed that using the uncertainties derived from generation level was sufficient for them.

Similar studies to that of chapter 9 where done on $t\bar{t}$ samples [109]. They resulted in a prediciton of a 23% systematic uncertainty for hadronization, a 16% uncertainty from p_T^{min} and a 24% uncertainty from the scale variation. In addition to these there is another systematic error due to the choice of generator. This was calculated as the deviation between POWHEG and MC@NLO to be 24%. This as well as the hadronization error were calculated with fully simulated events. The scale variation was calculated with the same pseudoscaling method as with W+Jets. The uncertainty from p_T^{min} was derived using the generator level MC, which is assumed to be sufficient because it is the smallest component. Additionally the variations in the p_T distributions for the jets were predominantly below the cut value of 30 GeV.

By far the largest component comes from the Jets Energy Scale. As previously shown in figure 8.11, this uncertainty was assessed in $\eta \times p_T$ grid. These values were used to shift the energy scale of all jets in both directions to assess this error. As GCW is not applied and many validation studies are still in progress, the values are relatively large. As can be seen in table 10.4 the JES for lower scale results in a $(29 \pm 14)\%$ variation. Alternatively the JES up results in a $(64 \pm 30)\%$ error on the MC production.

The systematic error estimation for the SUSY points proceeded in a similar manner. The same systematic error for each point will be used in the final limit calculation. For

Table 10.3: Cut flow numbers with W+Jets pseudoscaled for the estimation of systematic error.

Cut	W+Jets	SUM	DATA
W+Jets pseudoscaled up			
5	167553±184	268215±16745	270974
6	167222±184	252166±16740	254551
7	166564±183	251375±16740	245691
8	118375±155	124291±157	117684
9	2738±17	3340±18	4346
10	986.4±7.4	1449.2±8.3	2017
11	252.0±3.6	560.2±4.4	731
12	62.8±1.9	219.1±2.5	255
13	5.50±0.53	21.72±0.73	24
14	4.21±0.47	15.52±0.63	18
15	0.34±0.14	2.06±0.22	4
16	0.15±0.08	1.50±0.17	2
W+Jets pseudoscaled down			
5	170210±181	270872±16745	270974
6	169739±181	254682±16740	254551
7	169071±181	253882±16740	245691
8	118432±151	124348±153	117684
9	5482±30	6084±31	4346
10	2552±18	3015±19	2017
11	750±10	1059±11	731
12	190.9±5.4	347.2±5.7	255
13	16.8±1.6	33.1±1.7	24
14	13.0±1.4	24.3±1.5	18
15	1.00±0.41	2.72±0.44	4
16	0.48±0.28	1.83±0.31	2

Table 10.4: Comparison of the cut flows for the JES variation for 34.4 pb^{-1}.

Cut	J0-J6	DY	Di-Boson	W+Jets	Z+Jets	Single t	$t\bar{t}$	SUM	DATA
JES variation up									
5	58340±15229	3037±20	255.53±0.74	168828±182	25798±48	147.6±1.7	696.6±3.2	257102±15230	270974
6	57887±15223	1853±17	203.80±0.67	168439±182	11524±32	134.5±1.6	569.8±2.9	240612±15224	254551
7	57864±15223	1842±17	203.02±0.67	167778±181	11422±32	133.9±1.6	566.5±2.9	239809±15224	245691
8	1.99±1.26	24±1.1	132.35±0.55	118429±153	5459±22	94.4±1.3	401.8±2.5	124543±154	117684
9	1.99±1.26	1.98±0.41	44.18±0.32	4417±24	196.0±4.1	60.9±1.1	356.2±2.3	5078±25	4346
10	1.99±1.26	0.62±0.16	24.22±0.23	1873±13	84.9±2.7	46.20±0.99	343.7±2.3	2375±13	2017
11	0.17±0.06	0.19±0.10	7.20±0.13	524±6.6	24.9±1.4	20.86±0.70	283.2±2.0	860.3±7.1	731
12	0.09±0.05	0.00±0.00	1.35±0.05	131.1±3.3	6.79±0.73	6.20±0.38	165.8±1.6	311.3±3.7	255
13	0.02±0.02	0.00±0.00	0.21±0.02	13.51±1.02	0.10±0.07	1.09±0.16	21.36±0.57	36.3±1.2	24
14	0.02±0.02	0.00±0.00	0.13±0.02	10.56±0.91	0.10±0.07	0.91±0.15	14.45±0.47	26.2±1.0	18
15	0.00±0.00	0.00±0.00	0.02±0.01	1.18±0.34	0.04±0.04	0.20±0.08	2.15±0.18	3.59±0.40	4
16	0.00±0.00	0.00±0.00	0.01±0.01	0.77±0.27	0.04±0.04	0.16±0.07	1.69±0.16	2.68±0.33	2
JES variation down									
5	73109±16758	3049±20	257.91±0.74	169281±182	25911±49	149.3±1.7	706.64±3.26	272464±16759	270974
6	72657±16753	1857±17	205.36±0.68	168887±182	11324±32	135.7±1.6	577.15±2.95	255643±16754	254551
7	72634±16753	1845±17	204.57±0.68	168224±182	11230±32	135.2±1.6	573.72±2.94	254846±16754	245691
8	4.65±1.95	22.5±1.1	133.46±0.55	119070±153	5548±23	94.0±1.3	400.13±2.45	125273±155	117684
9	4.65±1.95	1.47±0.38	33.87±0.28	3398±21	147.1±3.6	51.7±1.0	326.58±2.22	3963±21	4346
10	3.76±1.74	0.35±0.12	16.59±0.19	1396±11	62.7±2.3	37.61±0.89	310.99±2.16	1828±11	2017
11	0.26±0.08	0.03±0.03	4.55±0.10	356±5.4	18.8±1.2	15.26±0.60	240.49±1.90	635.3±5.9	731
12	0.14±0.06	0.00±0.00	0.79±0.04	80.0±2.5	4.7±0.61	3.96±0.30	125.72±1.37	215.22±2.96	255
13	0.00±0.00	0.00±0.00	0.10±0.01	5.38±0.65	0.10±0.07	0.51±0.12	11.01±0.41	17.10±0.78	24
14	0.00±0.00	0.00±0.00	0.05±0.01	4.25±0.59	0.10±0.07	0.31±0.10	7.31±0.33	12.02±0.68	18
15	0.00±0.00	0.00±0.00	0.00±0.00	0.37±0.19	0.04±0.04	0.03±0.03	1.16±0.13	1.62±0.24	4
16	0.00±0.00	0.00±0.00	0.00±0.00	0.19±0.13	0.04±0.04	0.03±0.03	0.88±0.11	1.15±0.18	2

each source of uncertainty, a value is taken greater than the maximum variation seen for any point. Due to the smaller effect of the JES, the sources ignored for W+Jets and $t\bar{t}$ become inportant here. All values except JES were taken from recomendations of the SUSY group. They are summarized in table 10.5.

Table 10.5: The sources of systematic error for the signal points 10.5.

Renormalization/Fatorization Scale	14%
Parton Distribution Function	6%
Jet Energy Scale	12%
Jet Energy Resolution	2%
Muon Energy Scale	3%
Muon Energy Resoluion	1%
Muon Efficiency	3%
Underlying Event	1.5%

10.4.2 Limits

As no excess of data over MC background is seen, limits on specific SUSY models can be made. The analysis was applied to the SUSY grid points. For each point a signal selection efficiency, ϵ, can be defined. The selection efficiency is expected to be smooth in regions of the plane where there are no phenomenological features. However, the distribution obtained from MC is not smooth due to statistical fluctuations in the signal points. 10,000 signal events were generated for each point and this is insufficient for points with a low efficiency. In the low $m_{\frac{1}{2}}$ high m_0 region of the grid the efficiency was low and therefore the few remaining events cause high statistical error. There are no physical reasons for large efficiency fluctuations in this region. To smooth statistical effects the signal efficiency was fit to the form

$$\epsilon_{SigFit} = a + b \times m_0 + c \times m_{\frac{1}{2}} + d \times m_{\frac{1}{2}}^2 \tag{10.1}$$

on the points contained within the region $m_0 \in [200,440]$ GeV and $m_{\frac{1}{2}} \in [100,175]$ GeV. The fit was done with statistical error alone and was found to have a $\chi^2/\text{NDoF} = 1.5$.

The fit values were:

- a = $(5.6 \pm 2.4) \times 10^{-03}$
- b = $-(9.0 \pm 8.7) \times 10^{-07}$ GeV^{-1}
- c = $-(12.6 \pm 3.7) \times 10^{-05}$ GeV^{-1}
- d = $(7.9 \pm 1.4) \times 10^{-07}$ GeV^{-2}

When the ϵ_{SigFit} values at each grid point are substituted, the resulting distribution should be significantly smoothed in the problematic region. Figure 10.8 shows the smoothed and unsmoothed efficiency. The left plot shows the unsmoothed values calculated from the MC with the residual of the smoothing overlaid. It is calculated as,

$$\frac{\epsilon_{SigMC} - \epsilon_{SigFit}}{\sigma} \ . \tag{10.2}$$

The right plot shows the signal efficiency after the points had been substituted from the fit and then interpolated. A bilinear interpolation was used to interpolate between each point down to a 1 GeV spacing.

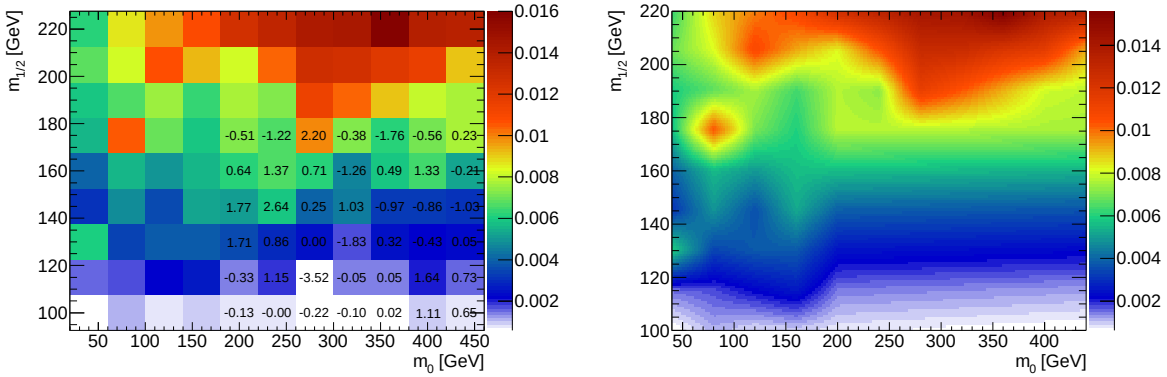

Figure 10.8: The signal selection efficiency (left) and the interpolated and smoothed signal selection efficiency (right).

The program TLimit [114] was used to derive limits at each signal point. A brief overview of the methods used in TLimit was given in section 4.4. The maximum signal cross section consistent at a 95% confidence level with a no signal observation will be

used to set limits. A systematic error of 190% was used for W+Jets as derived in the previous section. This is dominated by the 175% JES uncertainty calculated from table 10.4. The systematic uncertainty for Z+Jets was also set to 190% as this has similar systematic issues and the statistical error on the JES uncertainty in figure 10.4 was large. Similarly a 190% error was taken for the Di-boson sample because it was dominated by $WW \rightarrow \ell\nu qq$ which should have similar large dependencies on gluon radiation. For $t\bar{t}$, the systematic error of 54% was derived from the generator uncertainties combined to the 31% uncertainty from JES. For the single top samples the value of 54% was used since the systematics affecting it are similar to di-leptonic $t\bar{t}$. TLimit takes the quadratic sum of these systematic errors as an input.

The 11% uncertainty on the luminosity and the 20% systematic error on the signal points were also used for the limit calculation. The output is then a limited cross section for each point. These were interpolated down to a 1 GeV spacing and are shown in figure 10.9.

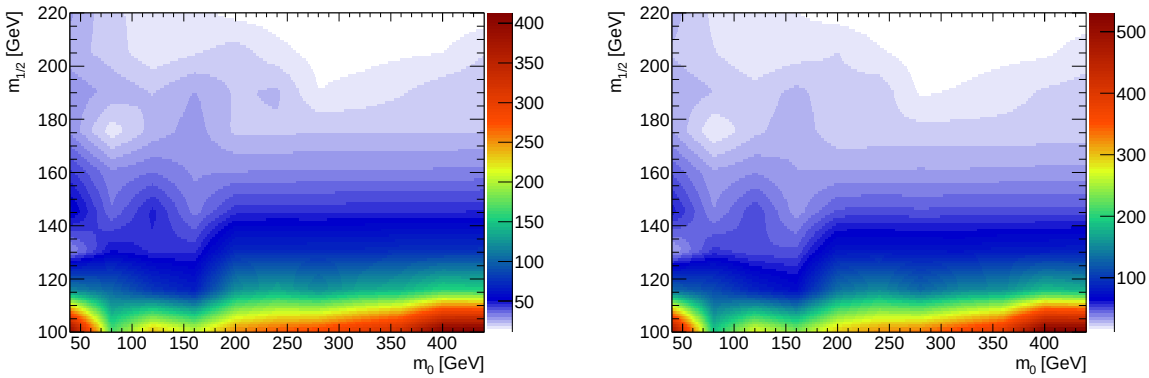

Figure 10.9: σ_{Limit} for the expected (left) and observed (right) limits in pb.

The theoretical cross section values shown previously in figure 10.1 were interpolated down to 1 GeV. If the limit cross section for a point is smaller than the theoretical cross section the point is said to be excluded. Since the important quantity for the limit is the difference between the real and limit cross section, plots for the difference $\sigma_{Theory} - \sigma_{Limit}$ are shown in figure 10.10. Regions where the difference is positive are excluded and a

black line indicates the 0 contour. The excluded points for the expected limit are denoted with triangles and the non-excluded points are denoted by circles. For the observed limits, the excluded points are denoted by squares and the non-excluded points are denoted by stars.

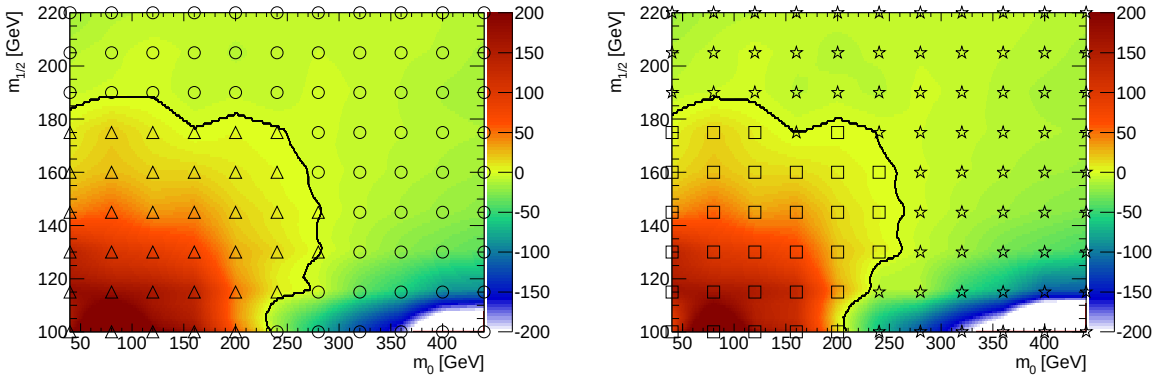

Figure 10.10: $\sigma_{Theory} - \sigma_{Limit}$ for the expected (left) and observed (right) limits in *pb*.

The limit contours in the plots of figure 10.10 are plotted in figure 10.11 along with other limits derived from previous experiments. The blue line shows the previous combined limit. A new region is excluded above the LEP limit. The crack in the D0 Trilepton exclusion represents a line where $m_{\widetilde{\ell}} \approx m_{\widetilde{\chi}_2^0} \approx m_{\widetilde{\chi}_1^\pm}$. To the left of this line slepton masses are just below the $m_{\widetilde{\chi}_2^0}$ mass, the leptons from the $\widetilde{\chi}_2^0 \rightarrow \widetilde{\ell}\ell$ decay have very small momentum, rendering the trilepton selections inefficient. Additionally, in this region the $\widetilde{\chi}_1^\pm \rightarrow \widetilde{\ell}\nu$ decay opens and increases the branching fraction for decays with leptons. Both of these effects result in an enhancement of the efficiency in this region. This can be seen in figure 10.8 as well as figure 10.12 where the expected number of signal events is shown. Only the $m_0 = 80$ GeV and $m_{\frac{1}{2}} = 175$ GeV point falls in this region. A finer grid spacing in this region may result in a feature in the limit contour. Since this would be an increased limit, not a reduced, limit the region which has been excluded in the DO limit crack is valid. These limits probe $\widetilde{q}/\widetilde{g}$ masses of a few hundred GeV. For example, the region around the point where $m_0 = 200$ GeV and $m_{\frac{1}{2}} = 175$ GeV has $\widetilde{t_1} \approx 300$ GeV, $\widetilde{b_1} \approx 400$ GeV and $\widetilde{g} \approx 450$ GeV. The curves for $\widetilde{b_1} = 500$ GeV and $\widetilde{g} = 500$ GeV are

shown in figure 10.11.

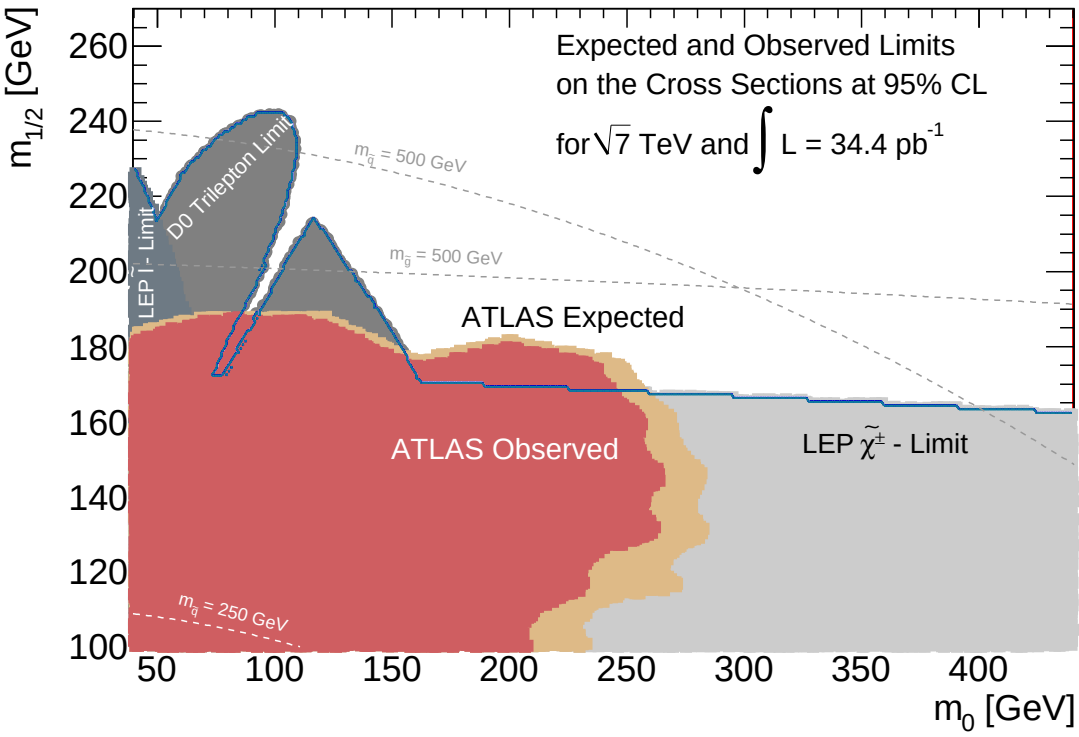

Figure 10.11: The contour plot of the exclusions of this analysis shown with that of the previous experiments.

The exclusion limit shown in figure 10.11 is consistent with the findings of Tevatron and LEP. The limit extends beyond these previous limits in specific regions. Due to the nature of the search, the exlusion band has a different shape than that of the previous experiments. The analysis done by the SUSY group was for 3 jets and combined the electron and muon channels [110]. The limits obtained by this analysis are shown in figure 10.13. Observed and expected 95% CL exclusion limits, as well as the 1σ variation on the expected limit are shown. Also shown are the published limits from CMS, CDF and D0, and the results from the LEP experiments.

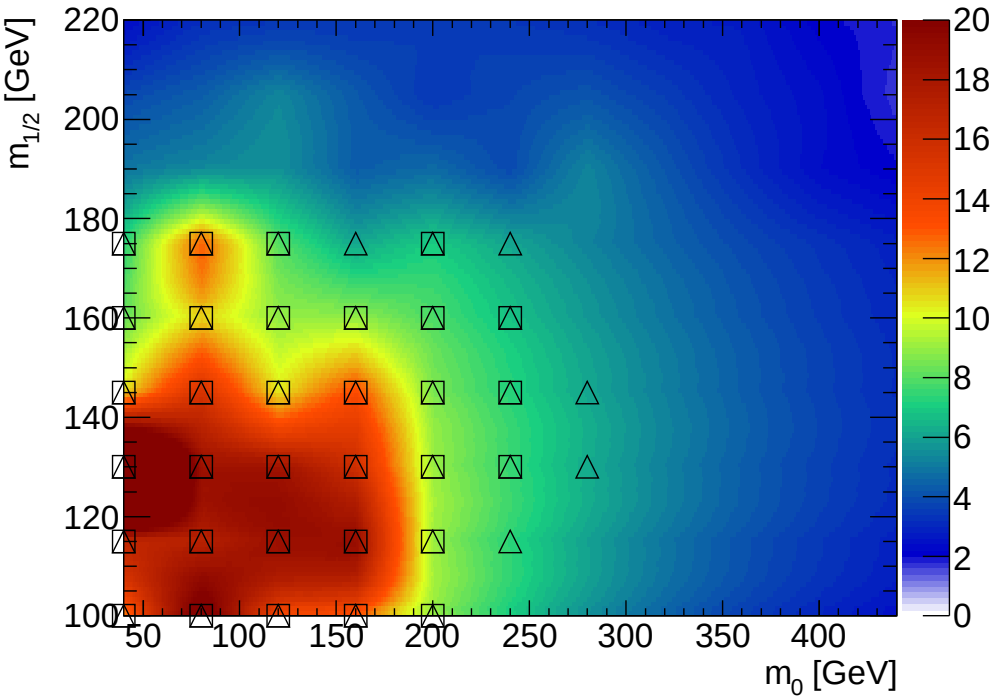

Figure 10.12: The interpolated number of expected signal events.

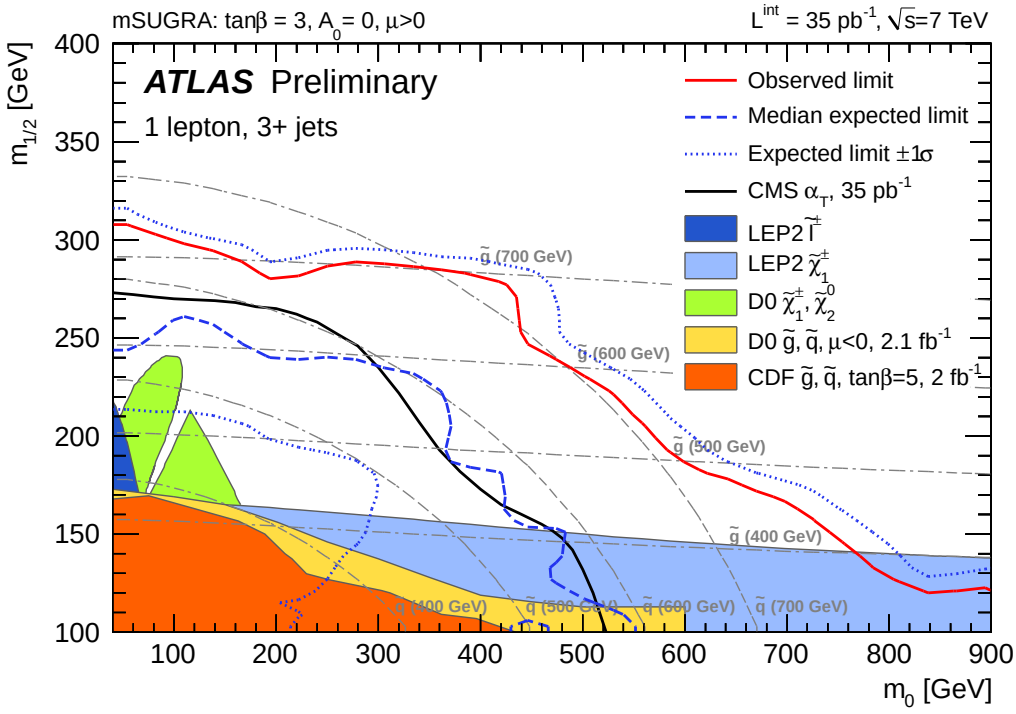

Figure 10.13: ATLAS SUSY Group results in the combined electron and muon channels for an integrated luminosity of 35 pb^{-1}. [110]

Chapter 11

Conclusion and Outlook

This thesis presented an analysis for the search of Supersymmetry with the ATLAS detector at the LHC. The final state with one lepton, several coloured particles and large missing transverse energy was chosen. For the analysis presented in this thesis only a small dataset was available and no significant deviation from the Standard Model was seen. Previous limits for minimal Supergravity set by Tevatron and LEP were extended. The statistical and systematic errors were large enough to accommodate for any discrepancies seen

The dominant systematic errors came from JES and MC generation scale uncertainty. The understanding of JES will be improved in the near future. This analysis did not use jets with any sophisticated calibration. The calibration procedures of Global Cell Weighting and Local Hadron Calibration will be a great benefit once they are available for general study.

In addition to this, there are several data driven methods for confirming the JES. Several similar methods were presented in chapter 8. The lowest luminosity method pertained to 10 pb^{-1} for 10 TeV. Assuming only combinatorial background, it resulted in a determination with a precision of 3.5%. A repetition of this work for 35 pb^{-1} at 7 TeV is likely to produce similar results. The study in chapter 8 made a few assumptions

about the performance and reliability of the correlated systematics associated to the issues mentioned above. The most important such assumption was that the W+Jets background was small compared to the combinatorial background. To reproduce similar results the event selection cuts will likely need to be tightened.

The Monte Carlo understanding and modelling of QCD processes has progressed greatly in the last few years. Common generators such as ALPGEN have well known failings. In chapter 9, these were investigated for W Boson production with associated QCD radiation to produce systematic error estimates. Newer generators, such as Sherpa, are expected to lower the systematic error by solving some of these issues. Data driven methods can be applied to ALPGEN samples to reduce errors. The most advantageous method is likely to be the reduction of the factorization and renormalization scale uncertainty by reweighting events based on the measured jet multiplicity and spectra. As discussed in section 9.4.2 the development of such a method is highly dependent on the understanding of other issues, most notably pile-up.

One can increase the limit reach by the combination with other channels. When the single lepton channels are combined with the multi-lepton channels, the methods described in section 7.3 can be exploited to optimize the boundaries between channels based on lepton definitions. The 0-lepton channel [115] can also be combined to provide further reach.

Expansion to new signal phase space grids or models provides interesting possibilities for new exclusions. The generation of large statistics of many signal points will be significantly assisted by the shorter running time of ATLFAST-II. Only one variety of Supersymmetry breaking was investigated in this thesis but several others will be searched for in the future.

In the coming year the LHC is expected to greatly increase the total integrated luminosity. Clearly the exclusion limits will significantly grow if no excess is seen. The expected discovery reach for 500 pb^{-1} shown in figure 4.1 has already been excluded.

The coming data taking period projects an integrated luminosity greater than 1000 pb^{-1}, opening new discovery possibilities. Extrapolations have been made for the 5σ minimal Supergravity discovery potential in terms of $m_{SUSY} = m_{\tilde{q}} = m_{\tilde{g}}$. The reach for various combined scenarios are shown in figure 11.1.

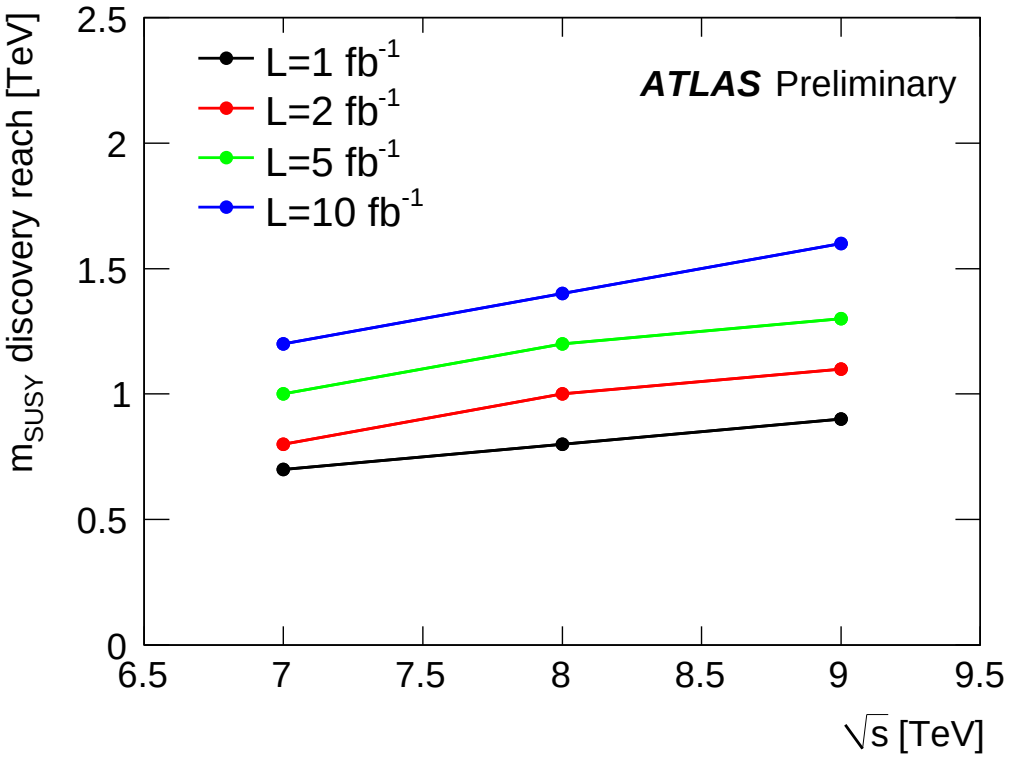

Figure 11.1: SUSY 5 σ discovery reach in TeV for different LHC scenarios [116].

List of Figures

List of Tables

Bibliography

[1] D.J. Griffiths. "Introduction to Elementary Particles" John Wiley & Sons, Inc., 1987;

[2] S. Eidelman et al., Phys. Lett. B 592, 1 (2004);

[3] M. Maltoni, T. Schwetz, M. A. Tortola, J. W. F. Valle, New Journal of Physics 6 (2004) 122. arXiv:hep-ph/0405172v6;
M.C. Gonzalez-Garcia, Y. Nir,, Reviews of Modern Physics 75 (2003) p. 345-402. arXiv:hep-ph/0202058v3;
The Super-Kamiokande Collaboration, Phys. Rev. Lett. 82 (1999) 1810-1814;

[4] Particle Data Group, J. Phys.G33 (2006) 11232, including 2007 updates;

[5] F. Halzen and A. D. Maritn, "Quarks and Leptons: An Introductory Course in Modern Particle Physics" New York, USA Wiley (1984);
S. Weinberg, "The Quantum Theory of Fields" Cambridge University Press, UK (1996);

[6] D. J. Gross and F. Wilczek, Ultraviolet behaviour of non-abelian gauge theories, Phys. Rev. Lett. 30 (1973) 1343;
H. D. Politzer, Reliable perturbative results for strong interactions, Phys. Rev. Lett. 30 (1973) 1346;

[7] R. P. Feynman and M. Gell-Mann, Phys. Rev. 109, 193 (1958);
R. E. Marshak and E. C. G. Sudarshan, Phys. Rev. 109, 1860 (1958);
J. J. Sakurai, Nuovo Cim. 7, 649 (1958);

[8] G. 't Hooft and M Veltman, Nuclear Physics B 44 (1972);

[9] S. P. Martin, hep-ph/9709356 (1997);
H. E. Haber and G. L. Kane, Phys. Rept. 117 (1985) 75;

[10] S. Coleman and J. Mandula, Phys. Rev. 159. 1251 (1967);

[11] Rudolf Haag, Jan T. Lopuszanski, and Martin Sohnius, Nucl. Phys. B88, (1974);

[12] W. Pauli, Phys. Rev. 58 no. 8, 716 (1940);

[13] P. van Nieuwenhuizen, Phys. Rep. 68, 189 (1981);

[14] Jean-Francois Arguin PHD Thesis fermilab-thesis-2005-63 (2005);

[15] E. H. Simmons, hep-ph/9908511 (1999);

[16] F. Zwirner, Phys. Lett. B 132, 103 (1983);
S. Dawson, Nucl. Phys. B 261, 297 (1985);
R. Barbieriand A. Masiero, Nucl. Phys. B 267, 679 (1986);
S. Dimopoulos and L. Hall, Phys. Lett. B 207, 210 (1988);
V. Barger, G. Giudice, and T. Han, Phys. Rev. D 40, 2987 (1989);
R. Godbole, P. Roy and X. Tata, Nucl. Phys. B 401, 67 (1993) [hep-ph/9209251];
G. Bhattacharyya and D. Choudhury, Mod. Phys. Lett. A 10, 1699 (1995) [hep-ph/9503263];
G. Bhattacharyya, Nucl. Phys. Proc. Suppl. 52A, 83 (1997) [hep-ph/9608415];
R. Barbier et al., Report of the GDR working group on the R-parity violation, (1998) [hep-ph/9810232];
B. Allanach et al., Searching for R-parity violation at Run-II of the Tevatron, [hep-ph/9906224];
B. Allanach, A. Dedes and H.K. Dreiner, Phys. Rev. D 69, 115002 (2004) [hep-ph/0309196];
M. Chemtob, Prog. Part. Nucl. Phys. 54, 71 (2005) [hep-ph/0406029]

[17] R.N. Mohapatra, Phys. Rev. D 34, 3457 (1986);
A. Font, L.E. Ibanez and F. Quevedo, Phys. Lett. B 228, 79 (1989);
S.P. Martin Phys. Rev. D 46, 2769 (1992) [hep-ph/9207218];
S.P. Martin Phys. Rev. D 54, 2340 (1996) [hep-ph/9602349];

[18] P. Fayet, NucI. Phys. B90 (1975) 104.;
A. Salam and J. Strathdee, Nucl. Phys. B87 (1975) 85;
G.R. Farrar and S. Weinberg, Phys. Rev. D27 (1983) 2732;
P. Fayet, Phys. Lett. 69B (1977) 489;
G. Farrar and P. Fayet, Phys. Lett. 76B (1978) 575;

[19] A.H. Chamseddine, R. Arnowitt and P. Nath, Phys. Rev. Lett. 49, 970 (1982);
R. Barbieri, S. Ferrara and C. A. Savoy, Phys. Lett. B 119, 343 (1982);
L.E. Ibanez, Phys. Lett. B 118, 73 (1982);
L.J. Hall, J.D. Lykken and S. Weinberg, Phys. Rev. D 27, 2359 (1983);
N. Ohta, Prog. Theor. Phys. 70, 542 (1983);
J. Ellis, D.V. Nanopoulos and K. Tamvakis, Phys. Lett. B 121, 123 (1983);
L. Alvarez-Gaume, J. Polchinski, and M. Wise, Nucl. Phys. B 221, 495 (1983);

[20] H. Georgi and S. L. Glashow, Phys. Rev. Lett. 32 (1974) no. 8, 438. 257 (1975);

[21] M. J. Duff, "M-Theory" arXiv:hep-th/9608117v3 (1996);

[22] D0 Collaboration "Evidence for an anomalous like-sign dimuon charge asymmetry" arXiv:1007.0395v1 [hep-ex] (2010);

[23] R. Mohanta, D. John,"Probing CP violation in the neutrino sector with magic baseline experiment", arXiv:1010.0288 (2010);

[24] T. Hahn et al, ECONF C0705302:HIG19, (2007) arXiv:0711.2020v1 [hep-ph];

[25] LHC Conceptual Design Report, CERN/AC/95-05, (1995);

[26] The LHC Study Group. "Design study of the large hadron collider" CERN/91-03, May (1991);

[27] CERN: The accelerator complex, http://public.web.cern.ch/public/en/Research/AccelComplex-en.html ;

[28] The ATLAS Collaboration, "ATLAS detector and Physics Performance Technical Design Report", CERN LHCC 99-14/15 (1999);

[29] http://visits.web.cern.ch/visits/guides/tools/manual/english/Atlas.html;

[30] Tao Han, MADPH-05-1434 (2005) arXiv:hep-ph/0508097v1;

[31] C. Fabjan. "Experimental Techniques in High Energy Physics: Calorimetry in high-energy physics". Adison-Wesley, (1987);
D. E. Groom et al. Review of particle physics. "The European Physical Journal", C15, (2000);
R. Wigmans. "On the Energy Resolution of uranium and other Hadron Calorimeters." Nuclear Instrumentation Methods, A259: 389-429, (1987);

[32] The ATLAS Collaboration, G. Aad et al., "The ATLAS Experiment at the CERN Large Hadron Collider", JINST 3 (2008) S08003;

[33] ATLAS Liquid Argon Calorimeter Group, ATL-LARG-PROC-2010-016 (2010);

[34] The ATLAS Collaboration CERN-PH-EP-2010-024 (2010) arXiv:1007.5423v1 [physics.ins-det];

[35] The ATLAS Collaboration ATLAS-CONF-2010-067 (2010);

[36] The ATLAS Collaboration, CERN-OPEN-2008-020/ arXiv:0901.0512 [hep-ex] (2008);

[37] J T M Baines, ATL-COM-DAQ-2010-201 (2010);

[38] C. F. Berger, J. S. Gainer, J. L. Hewett, T. G. Rizz, JHEP 0902:023 (2009) / arXiv:hep-ph/0812.0980;

[39] The ATLAS Collaboration, ATL-PHYS-PUB-2010-010 (2010);

[40] Masters thesis of Irene Niessen, "Supersymmetric Phenomenology in the mSUGRA Parameter Space." (2008);

[41] S. L. Glashow, J. Iliopoulos and L. Maiani, Phys. Rev. D 2, 1285 (1970);

[42] The ATLAS Collaboration CERN-PH-EP-2010-037 (2010) arXiv:1010.2130v1 [hep-ex];

[43] K. Melnikov and F. Petriello. Phys. Rev. **D74**, 114017 (2006) [hep-ph/0609070]; R. Gavin, Y. Li, F. Petriello *et al.*, "FEWZ 2.0: A code for hadronic Z production at next-to-next-to-leading order," [arXiv:1011.3540 [hep-ph]];

[44] K. Melnikov and G. Zanderighi, "W + 3 jet production at the LHC as a signal or background" arXiv:0910.3671 [hep-ph] (2009);

[45] M. Simonyan ATLPHYSINT-2009076 (2009);

[46] M. Boulware and D. Finnell, Phys. Rev. D 44, 2054 (1991);
G. Altarelli, R. Barbieri and F. Caravaglios, Phys. Lett. B 314, 357 (1993);
J.D. Wells, C. Kolda and G.L. Kane Phys. Lett. B 338,219 (1994) [hep-ph/9408228];
G. Kane, R. Stuart, and J.D. Wells, Phys. Lett. B 354, 350 (1995)[hep-ph/9505207];
D. Garcia and J. Sola, Phys. Lett. B 357, 349 (1995) [hep-ph/9505350];
J. Erler and P. Langacker, Phys. Rev. D 52, 441 (1995) [hep-ph/9411203];
X. Wang, J. Lopez and D.V. Nanopoulos, Phys. Rev. D 52, 4116 (1995) [hep-ph/9506217];
P. Chankowski and S. Pokorski, Nucl. Phys. B 475, 3 (1996) [hep-ph/9603310];
J.A. Grifols and A. Mendez, Phys. Rev. D 26, 1809 (1982);
J.R. Ellis, J.S. Hagelin and D.V. Nanopoulos, Phys. Lett. B 116, 283 (1982);
R. Barbieri and L. Maiani, Phys. Lett. B 117, 203 (1982);
D.A. Kosower, L.M. Krauss and N. Sakai, Phys. Lett. B 133, 305 (1983);
T.C. Yuan, R. Arnowitt, A.H. Chamseddine and P. Nath, Z. Phys. C 26, 407 (1984);
I. Vendramin, Nuovo Cim. A 101, 731 (1989);

[47] S. Bertolini, F. Borzumati, and A. Masiero, Nucl. Phys. B294 (1987) 321;
S. Bertolini, F. Borzumati, A. Masiero, and G. Ridolfi, Nucl. Phys.; B353 (1991) 591.

[48] S. Ferrara and E. Remiddi, Phys. Lett. B53 (1974) 347.;

[49] WMAP Collaboration, Astrophys. J. Suppl. 148, 175 (2003) [astro-ph/0302209], and [astro-ph/0603449];
SDSS Collaboration, Phys. Rev. D 69, 103501 (2004) [astro-ph/0310723];

[50] LEPSUSYWG, ALEPH, DELPHI, L3 and OPAL experiments, Charginos, large m0 LEPSUSYWG/01-03.1

[51] The D0-Collaboration, "Search for associated production of charginos and neutralinos in the trilepton final state using 2.3 fb^{-1} of data", arXiv:/0901.0646 [hep-ex];

[52] The D0 Collaboration, V. Abazov, et al., "Search for Squarks and Gluinos in events with jets and missing transverse energy using 2.1 fb^{-1} of $p\bar{p}$ collision data at $\sqrt{s} = 1.96$ TeV ", arXiv:0712.3805v2 [hep-ex];

[53] LEPSUSYWG, ALEPH, DELPHI, L3 and OPAL collaborations, note LEPSUSYWG/02-06.2;

[54] R.D. Cousins and V.L. Highland, Nucl. Instrum. Meth. A320 (1992) 331335;
J. T. Linnemann, Measures of significance in HEP and astrophysics, (2003);.

[55] T. Junk, CARLETON/OPAL PHYS 99-01 arXiv:hep-ex/9902006v1 (2009);

[56] ATLAS workbook, twiki.cern.ch/twiki/bin/view/Atlas/WorkBook

[57] P. Mato et al. GAUDI LHCb Data Processing Application Framework LHCb 98-064 COMP;

[58] H. Baer et al, "Les Houches Guidebook to Monte Carlo Generators for Hadron Collider Physics", arXiv:hep-ph/0403045 v1, (2004);
E. Boos et. al., "Generic user process Interface for Event Generators" hep-ph/0109068 (2001);

[59] T. Sjostrand, S.Mrenna, P. Skands, PHYTHIA 6.4, arXiv:hep-ph/0603175 (2006);

[60] G. Corcella et al. HERWIG 6.5 arXiv:hep-ph/oo11363 v3, (2002);

[61] Jimmy Group, http://projects.hepforge.org/jimmy/;

[62] M. L. Mangano et al. hep-ph/0206293 (2006);

[63] S. Frixione, B. R. Webber, The MC@NLO 3.3 Event Generator, Cavendish-HEP-06/28, (2006);

[64] GEANT4 Collaboration, GEANT4: a simulation toolkit, Nuclear Instruments and Methods A, Volume 506, (2003);
R. Brun and F. Carminati, CERN Program Library Long Writeup W5013 (1993);

[65] M. Dührssen, ATLAS Internal Note, ATL-PHYS-INT-2008-043, (2008);

[66] Decisions regarding this issue were made in the Hadronic calibration workshop on the 23^{rd} of June 2009 in Foz do Arelho Portugal.

[67] L. Asquith et al. Performance of Jet Algorithms in the ATLAS Detector, ATLAS note, April 8, (2010);
M. Cacciari, G. Salam and G. Soyez, JHEP 0804, 063 (2008), [arXiv:0802.1189];

[68] The ATLAS Collaboration ATL-COM-PHYS-2010-848 (2010);

[69] T. Cornelissen et al., ATL-SOFT-PUB-2007-007 (2007);

[70] "Electron and photon reconstruction and identification in ATLAS" in preparation

[71] https://twiki.cern.ch/twiki/bin/view/AtlasPublic

[72] The ATLAS Collaboration ATLAS-CONF-2010-064 (2010);

[73] The ATLAS Collaboration ATLAS-COM-CONF-2011-001(2011);

[74] The ATLFAST-II benchmark group, ATL-PHYS-INT-2009-110, (2009);

[75] F.E. Paige, S.D. Protopopescu, H. Baer, and X. Tata, ISAJET 7.69: A Monte Carlo event generator for p p, anti-p p, and e+ e- reactions, hep-ph/0312045, (2003);

[76] M. Bahr et al., Herwig++ Physics and Manual, Eur. Phys. J. C58 (2008) 639,arXiv:0803.0883.

[77] A. Sherstnev and R.S. Thorne, Eur. Phys. J. C55 (2008) 553-575;

[78] W. Beenakker, R. Hopker and M. Spira, PROSPINO: A program for the production of supersymmetric particles In next-to-leading order QCD, hep-ph/9611232, (1996);

[79] P. Nadolsky et al Phys.Rev.D78:013004 (2008) arXiv:0802.0007 [hep-ph];

[80] A. Arce et al, ATL-COM-PHYS-2010-838 (2010);

[81] L. Asquith et al., "Performance of Jet Algorithms in the ATLAS Detector", ATL-COM-PHYS-2009-630 (2010);

[82] ATLAS Collaboration, "Readiness of the ATLAS Liquid Argon Calorimeter for LHC Collisions", arXiv:0912.2642;
M. Aharrouche et al., Nucl. Instrum. Meth. A614 (2010) 400-432;
M. Aharrouche et al., Nucl. Instrum. Meth. A597 (2008) 178-188;

[83] M. Aharrouche et al., "Readiness of the ATLAS Tile Calorimeter for LHC collisions", arXiv:1007.5423 [physics.ins-det];

[84] E. Abat et al., , ATL-CAL-PUB-2010-001, (2010);

[85] Hossain Ahmed, presented at ATLAS Physics Workshop of the Americas, SFU, June 17 2008;

[86] M. R. Whalley et al. "The Les Houches Acord PDFs and Lhaglue" hep-ph/0508110;

[87] The ATLAS Collaboration CERN-PH-EP-2010-034 (2010) arXiv:1009.5908 [hep-ex];

[88] S. Mrenna, P. Richardson, "Matching Matrix Elements and parton Showers with Herwig and Pythia", arXiv:hep-ph/0312274 (2003);

[89] J. Alwall et al. arXiv:hep-ph/0706.2569 (2008);

[90] F. Caravaglios and M. Moretti, Phys. Lett. B 358 (1995) 332 [hep-ph/9507237];

[91] J. Pumplin, D. R. Stump, J. Huston, H. L. Lai, P. Nadolsky and W. K. Tung, JHEP 0207 (2002) 012. [arXiv:hep-ph/0201195v3];

[92] V.N. Gribov, L,N. Lipatov. Sov.J.Nucl.Phys. 15:438 (1972);
G. Altarelli and G. Parisi. Nucl. Phys. B126:298 (1977);
Yu. L. Dokshitzer. Sov.Phys. JETP, 46:641 (1977);

[93] S. Catani, F. Krauss, R. Kuhn and B. R. Webber, JHEP 11 (2001) 063, hep-ph/0109231;
F. Krauss, JHEP 08 (2002) 015, hep-ph/0205283;

[94] J. Alwall et al., Eur. Phys. J. C53 (2008) 473500;

[95] F. Caravaglios, M. L. Mangano, M. Moretti and R. Pittau Nucl. Phys. B539 (1999) 215-232 hep-ph/9807570;

[96] B. Andersson et al., Phys. Rept. 97 (1983) no. 2-3, 31;

[97] X. Artru and G Mennessier, Nucle. Phys. B70 (1974) 93;
M. G. Bowler, Zeit. Phys. C11 (1981) 169;
B. Andersson, G. Gustafson and B. Söderberg, Zeit. Phys. C20 (1983) 317; Nucl. Phys. B264 (1986) 29 ;

[98] T. Sjöstrand, Comp. Phys. Comm. 39 (1986) 347;
M. Bengtsson and T. Sjöstrand, Comp. Phys. Comm. 43 (1987) 367;
T. Sjöstrand, S. Mrenna, and P. Skands, Comput. Phys. Commun. 178 (2008) 852, arXiv:0710.3820 ;

[99] D. Amati and G Veneziano, Phys Lett B83 (1979) 87;
A. Bassetto, M. Ciafaloni and G. Marchesini, Phys. Lett. B83 (1979) 207;
G. Marchesini, L. Trentadue and G. Veneziano, Nucl. Phys. B182 (1980) 335;

[100] The ATLAS collaboration, ATL-COM-PHYS-2010-031(2010);

[101] The ATLAS collaboration, ATL-PHYS-PUB-2010-014(2010);

[102] C.F. Berger et al., Phys. Rev. D80 (2009) 074036;

[103] Paolo Nason, JHEP0411:040, (2004) arXiv:hep-ph/0409146v1;

[104] T. Gleisberg, et al JHEP 0402 (2004) 056 [hep-ph/0311263] ;

[105] R. Kuhn, F. Krauss, B. Ivayi and G. Soff, Comput. Phys. Commun 134 (2001) 223-266 [hep-ph/0004270];

[106] S, Schumann, F, Krauss JHEP0803:038, (2008) arXiv:0709.1027v1 [hep-ph];

[107] S. Hoeche, F. Krauss, S. Schumann, F. Siegert, JHEP 0905:053,(2009) arXiv:0903.1219v2 [hep-ph];

[108] J. Winter, F. Krauss, G. Soff Eur.Phys.J.C36:381-395, (2004) [arXiv:hep-ph/0311085v1];

[109] The ATLAS Collaboration ATLAS-CONF-2010-066 (2010);

[110] The ATLAS Collaboration ATL-COM-PHYS-2010-1071 (2010);
The ATLAS Collaboration ATL-COM-PHYS-2010-1039 (2010);
The ATLAS Collaboration ATLAS-SUSY-2010-01-002 (2010);

[111] The ATLAS Collaboration ATL-COM-PHYS-2010-826(2010);

[112] The ATLAS Collaboration ATL-COM-PHYS-2010-836(2010);

[113] The ATLAS Collaboration ATL-COM-PHYS-2010-695(2010);

[114] Thomas Junk arXiv:hep-ex/9902006 (1999);

[115] The ATLAS Collaboration ATL-COM-PHYS-2010-1046 (2010);
The ATLAS Collaboration ATL-COM-PHYS-2010-1077 (2010);
The ATLAS Collaboration ATLAS-SUSY-2010-05-001(2010);

[116] The ATLAS Collaboration ATL-PHYS-PUB-2011-003 (2011);